**Doctoral thesis of University of Lille**

**Doctoral School** 104
Matter, Radiation and Environmental Sciences

Defended on 19/12/2024, by :
**Jeyan Bichon**

---

# Complex refractive index determination of suspended particles in a controlled environment by TeraHertz spectroscopy

---

Committee members :

| | |
|---|---|
| **Gwenaël Gaborit**<br>Associate professor, CROMA/University of Savoie | **Reviewer** |
| **Weidong Chen**<br>Professor, LPCA/University of Littoral Côte d'Opale | **Reviewer** |
| **Jerôme Yon**<br>Professor, CORIA/University of Rouen Normandie | **President of the jury** |
| **Isabelle Chiapello**<br>Research scientist, LOA/University of Lille | **Examinator** |
| **Sophie Eliet**<br>Research engineer, IEMN/CNRS | **Advisor** |
| **Denis Petitprez**<br>Professor, PC2A/University of Lille | **Thesis director** |
| **Alexandre Deguine**<br>Associate professor, LPCA/University of Littoral Côte d'Opale | **Invited** |
| **Romain Peretti**<br>Research scientist, IEMN/CNRS | **Invited** |

**Thèse de doctorat de l'Université de Lille**

**École Doctorale** 104
Sciences de la Matière, du Rayonnement et de l'Environnement

Soutenue le 19/12/2024, par :
**Jeyan Bichon**

---

# Détermination de l'indice de réfraction complexe de particules en suspension dans un environnement contrôlé par spectroscopie Térahertz

---

Membres du jury :

| | |
|---|---|
| **Gwenaël Gaborit**<br>Maître de conférences, CROMA/Université de Savoie | **Rapporteur** |
| **Weidong Chen**<br>Professeur, LPCA/Université du Littoral Côte d'Opale | **Rapporteur** |
| **Jérôme Yon**<br>Professeur, CORIA/Université de Rouen Normandie | **Président du jury** |
| **Isabelle Chiapello**<br>Chercheuse, LOA/Université de Lille | **Examinatrice** |
| **Sophie Eliet**<br>Ingénieure de recherche, IEMN/CNRS | **Encadrante** |
| **Denis Petitprez**<br>Professeur, PC2A/Université de Lille | **Directeur de thèse** |
| **Alexandre Deguine**<br>Maître de conférences, LPCA/Université du Littoral Côte d'Opale | **Invité** |
| **Romain Peretti**<br>Chercheur, IEMN/CNRS | **Invité** |

*"Here is my secret. It is very simple : it is only with the heart that one can see rightly; what is essential is invisible to the eye."*

Antoine de Saint-Exupéry

*"Voici mon secret. Il est très simple : On ne voit bien qu'avec le cœur. L'essentiel est invisible pour les yeux."*

Antoine de Saint-Exupéry

# Abstract

The composition of Earth's atmosphere is crucial for regulating environmental phenomena and, consequently, climate change. Terahertz (THz) radiation, spanning frequencies from 0.1 to 10 THz, interacts with suspended atmospheric particles via absorption and scattering, influencing the planet's radiative balance. However, the effects of atmospheric aerosols in the THz range remain largely unexplored, due to the recent availability of appropriate sources and detectors at these frequencies. Determining the optical properties of atmospheric aerosols in the THz band, particularly their complex refractive indices, is essential for understanding their role in modulating Earth's radiative balance. This study addresses this need by developing a setup operating in the 0.2 to 5 THz range, specifically designed to investigate atmospheric aerosol particles. Using this setup, we recorded and analyzed THz spectra of natural aerosols, including a sample from the Gobi Desert, to deduce their optical properties and better understand their potential environmental implications.

# Résumé

La composition de l'atmosphère terrestre est cruciale pour réguler les phénomènes environnementaux et, par conséquent, le changement climatique. Le rayonnement TéraHertz (THz), s'étendant sur des fréquences de 0,1 à 10 THz, interagit avec les particules atmosphériques en suspension par absorption et diffusion, influençant ainsi le bilan radiatif de la planète. Cependant, les effets des aérosols atmosphériques dans la plage THz restent largement inexplorés en raison de la disponibilité récente de sources et de détecteurs appropriés à ces fréquences. La détermination des propriétés optiques des aérosols atmosphériques dans la bande THz, en particulier leurs indices de réfraction complexes, est essentielle pour comprendre leur rôle dans la modulation du bilan radiatif de la Terre. Cette étude répond à ce besoin en développant un dispositif fonctionnant dans la plage de 0,2 à 5 THz, spécifiquement conçu pour étudier les particules d'aérosols atmosphériques. À l'aide de ce dispositif, nous avons enregistré et analysé les spectres THz d'aérosols naturels, y compris un échantillon provenant du désert de Gobi, afin de déduire leurs propriétés optiques et de mieux comprendre leurs implications environnementales potentielles.

# Acknowledgements

I would like to express my deepest gratitude to Sophie Eliet. The project that became the foundation of my doctoral thesis was born from your vision. More than a mentor, you have been an incredible listener, always encouraging me to express myself freely as a young scientist. Your positivity and inspiration have been constant throughout this journey and I feel truly lucky to have shared it with you.

I also want to sincerely thank Denis Petitprez for his invaluable guidance. Your expertise has played a crucial role in shaping my work. Despite the challenges of working in different laboratories, you were always available, supportive, and understanding. Your mentorship has meant a lot to me, and I am deeply grateful for everything you have done.

A special thank you to Romain Peretti. Even though you were not officially my supervisor, you took on that role with generosity and dedication. Your scientific insights and practical advice have been invaluable. Title or not, you have been a true mentor to me.

I extend my sincere gratitude to the members of my jury: Gwenaël Gaborit, Weidong Chen, Jérôme Yon, Isabelle Chiapello, Alexandre Deguine, and Romain Peretti, for the time and effort you dedicated to evaluating my work.

I am also very grateful to Karine Deboudt from LPCA for her expertise and support in analyzing atmospheric aerosols through SEM-EDX and XRD. Your help has been essential for our study.

To my colleagues: Alexandre, Alexandra, Roman, Elsa, Eliot, Valentin, Niels, Cristiane, Ali, Vianney, and Victor, thank you for making this journey more enjoyable with your kindness. A special acknowledgment to Noureddin, Walter, Théo, Youssef, Mélanie, and Adrien, with whom I had the honor of sharing my workspace.

My appreciation also extends to the THz photonics team at IEMN, who welcomed me so warmly. A special thanks to Jean-François for the interesting discussions about polaritons. A heartfelt thank you to the characterization team at IEMN—Étienne, Sylvie, and Vanessa.

I would also like to thank the atmospheric physicochemistry team at PC2A for their kindness and hospitality. In particular, Valentine and Sylvie, with whom the resuspension experiments quickly became a pleasure. I am also grateful to

Jérôme, Valisoa, and Luna, with whom I shared great moments outside the lab. A special thanks to Lise for her work on the Gobi particles.

And finally, to my interns, Taha and Romane : I wish you both the very best for the future—you have the skills, passion, and determination to achieve great things.

To my lifelong friends: Constance, Cédric, Cécile, Camille, and Charlotte—my entire C-team. Since we were ten years old, you have been by my side, through every stage of my life. You have been my pillars throughout my studies and my trusted companions in all my adventures. Your friendship is one of the greatest gifts in my life, and I cherish every moment we share.

To my fiancé, Quentin—we met at the very beginning of my PhD, while you were completing your own thesis. Your love, patience, and support have made this journey not only easier but also deeply meaningful. I am so grateful for you, for the life we are building together, and for all the rescued animals that will undoubtedly be part of it. Thank you for being my partner in every sense of the word.

Lastly, my deepest gratitude goes to my family: my parents, Nalan and Patrick, and my brother, Jekfer. Mom, thank you for always being there to listen, and Dad, for making sure I had everything I needed to focus on my studies. I also want to acknowledge my grandmother, Mémé Marie, who passed away during my thesis. I regret that she will not be here to see its conclusion.

To conclude, I honor all the animals
who illuminate my days,
with their loyal spirits and tender gaze,
teaching love in silent ways.

A special tribute to those now gone,
or those enduring their trials still,
their memories will linger on,
a reminder of their pure and gentle will.

# Contents

# List of Figures

# List of Tables

# General introduction

Atmospheric aerosols play a crucial role in climate processes by interacting with both solar and terrestrial radiation. Some aerosols reflect radiation, causing cooling, while others absorb it, contributing to atmospheric warming. Accurately understanding their optical properties is key to assessing their impact on the climate. However, atmospheric aerosols have never been explored at Terahertz (THz) frequencies (0.1 to 10 THz), making this an entirely new area of investigation.

Recent technological advancements in the THz domain have enabled robust and reliable signal generation and detection. Since solid particles produce a broad signal that spans several GHz to a few THz, THz time-domain spectroscopy (THz-TDS) emerges as a powerful technique for their analysis. This method provides broadband spectroscopy and allows access to both signal amplitude and phase, making it particularly relevant for studying aerosols.

The research carried out during this thesis focuses on how aerosols, particularly desert dust, interact with THz radiation and what these interactions reveal about their optical behavior. By filling this gap, the work opens new possibilities for characterizing aerosols, providing novel insights into their role in atmospheric processes. To address these multidisciplinary questions, this thesis was conducted as part of the ANR STEPSON project, in collaboration with LPCA (Laboratoire de Physico-Chimie de l'Atmosphère), LOA (Laboratoire d'Optique Atmosphérique), PC2A (PhysicoChimie des Processus de Combustion et de l'Atmosphère), and IEMN (Institut d'Électronique, de Microélectronique et de Nanotechnologie).

Chapter one lays the groundwork for applying THz-TDS to aerosol studies, tracing the technique's development and outlining the challenges of studying particles in aerosol form at THz frequencies. Chapter two details the design and characterization of a THz-TDS spectrometer (0.2 - 5 THz) specifically developed for aerosol analysis (sizes ranging from 0.1 to 10 μm), describing the experimental setup and signal interpretation.

The third chapter presents the results obtained with our experimental setup, which successfully recorded THz spectra of Gobi Desert aerosols, including particles of calcite, quartz, and clays. Additionally, these particles were morphologically and chemically characterized using scanning electron microscopy with energy-dispersive X-ray spectroscopy (SEM-EDX) and X-ray diffraction (XRD). This combined approach provides a comprehensive assessment of the particles'

optical behavior, both in pellet form and in suspension. Therefore, this chapter demonstrates the functionality and reliability of our THz setup for aerosol studies, validating its ability to accurately measure and analyze the optical properties of atmospheric aerosols within the THz range.

The final chapter addresses the need for simulations to deepen our understanding of THz-aerosol interactions at the single-particle level. Finite-Difference Time-Domain (FDTD) simulations are performed to investigate the absorption and scattering cross-sections of calcite particles as a function of particle radius. Additionally, the simulations are compared to a Mie theory code using mixed-index models to extract the complex refractive indices of the materials. This approach provides a robust framework for interpreting the optical behavior of aerosols in the THz range.

This thesis represents the first comprehensive application of THz-Time Domain Spectroscopy (0.2 - 5 THz) to particle analysis in a gas-suspended state (aerosol form), pioneering a previously unexplored frequency range and opening the door to a new field of study. While this research marks an important step forward, much remains to be discovered. The findings have the potential to improve climate models and broaden our understanding of aerosol interactions with THz radiation, with promising applications in areas such as environmental monitoring and telecommunications.

# Chapter 1

# Context

This thesis addresses a multidisciplinary topic at the intersection of Terahertz (THz) domain and aerosol science, focusing specifically on desert dust particles. Given the broad scope of the subject, certain decisions had to be made regarding the depth and breadth of the contextual chapter. While this chapter provides an overview of the key elements necessary to understand the research, it is by no means exhaustive.

For readers who wish to delve deeper into the specific aspects covered, I recommend consulting the works of Mélanie Lavancier [1] and Théo Hannotte [2] for comprehensive insights into THz frequencies. For those interested in aerosol science, particularly in the context of Gobi Desert particles, Lise Deschutter's thesis and its references offer a thorough exploration of the subject [3].

These references will complement the multidisciplinary nature of this work and provide additional context for readers seeking a more in-depth understanding of the fields involved.

## 1.1 Atmospheric aerosols

### 1.1.1 Definition

Atmospheric aerosols are considered a two-phase system consisting of solid or liquid particles suspended in the gas (i.e. air in the case of Earth) of the atmosphere [4]. Aerosols of natural origin mainly come from soil erosion, desert dust storms, volcanic eruptions and wave splashes whereas anthropogenic aerosols are generated by industrial and agricultural activities, vessel exhaust, biomass and fossil fuel combustion.

In figure 1.1, results from the Goddard Earth Observing System Forward Processing (GEOS FP - Analyses and forecasts produced in real time) aerosol model from August 23, 2018 exhibit the ubiquity of aerosols of different sources in the atmosphere with smoke drifting above the North America and rough tropical cyclones in the Pacific Ocean, and large dust clouds over the deserts of Asia. Sea salts are shown in blue, black carbon particles in red, and dust particles in purple.

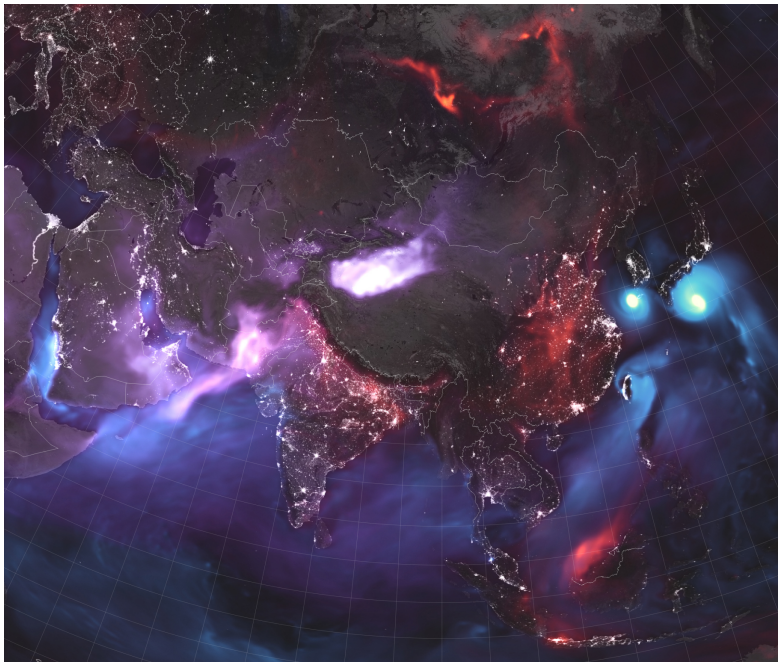

Figure 1.1: Image of the Day for August 23, 2018 from NASA with Goddard Earth Observing System Forward Processing (GEOS FP) model. The storms are visible within swirls of sea salt aerosol (blue). Black carbon particles (red) are among the particles emitted by fires. Dust particles are in purple.

Aerosols that are directly emitted in the atmosphere are known as primary aerosols. Secondary aerosols are formed by chemical reaction and gaseous conversion into particles of volatile organic compounds in the atmosphere, either by formation of new particles, by gas-particle separation, and finally by heterogeneous or multiphasic reactions [5]. Suspended particles constitute an extremely heterogeneous group whose size varies from a few tenths of nanometer to a hundred micrometers. These atmospheric particles play an important role in climate and atmospheric chemistry: they scatter and absorb solar and telluric radiation, provide condensation nuclei for cloud droplets, and participate in heterogeneous chemical reactions [6].

### 1.1.2 Impact of atmospheric aerosols

Atmospheric aerosols play a crucial dual role in the environment, exerting both direct and indirect effects. Directly, they scatter and absorb solar and terrestrial radiation, which modifies the amount of energy that reaches the Earth's surface and escapes back into space.

The peak radiation emitted from Earth occurs at a wavelength of 10 micrometers, well within the infrared range. As shown in figure 1.2, terrestrial emission wavelength is roughly 20 times longer than the peak solar emission wavelength. Therefore radiation emitted by Earth is often referred to as long-wave radiation, whereas solar radiation is called short-wave radiation [7]. The radiative balance is

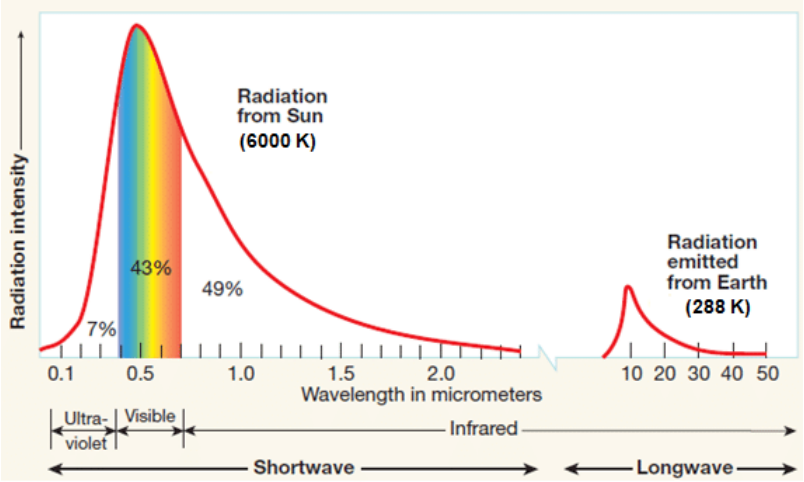


Figure 1.2: Radiation intensity of solar and telluric emissions from [7].

the sum of all incoming (i.e. shortwave and longwave radiation) minus outgoing radiant energy flows. Therefore, in-depth knowledge of the optical properties of atmospheric components such as complex refractive indices is necessary to assess the radiative forcing.

Indirectly, aerosols influence cloud properties and formation, subsequently affecting precipitation patterns and climate dynamics. Understanding these interactions is essential for evaluating the overall impact of aerosols on climate change and environmental health.

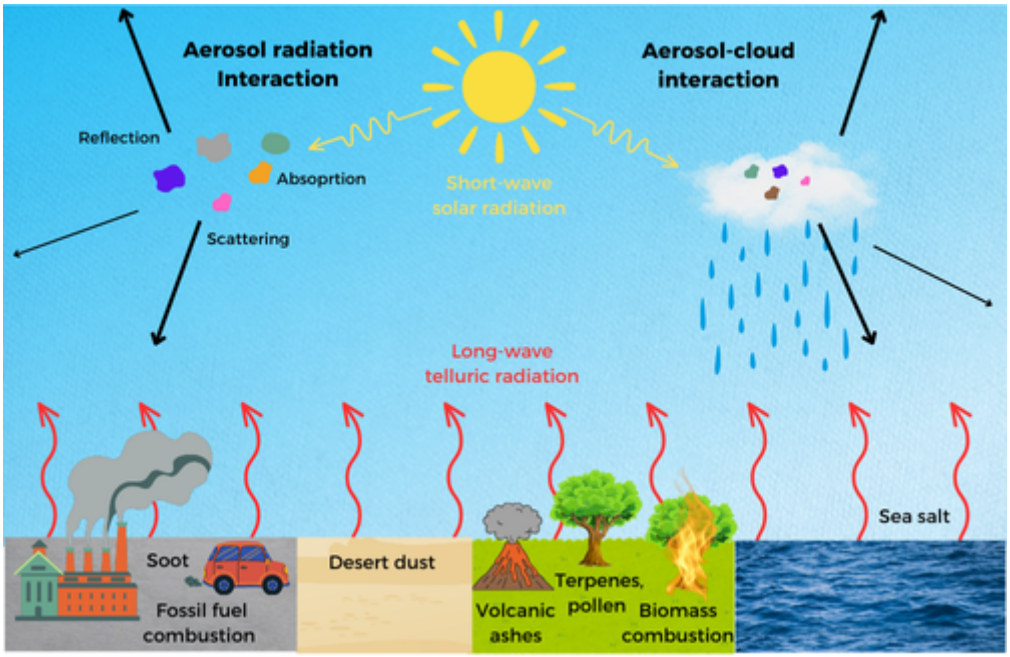


Figure 1.3: Emission sources of atmospheric aerosols and their direct and indirect effects on the Earth's climate system.

Due to their potentially harmful effects on climate and health, the Stockholm

Resilience Center designates aerosol pollution as one of the nine planetary boundaries, that is, one of nine processes essential for maintaining the stability and resilience of the Earth system as a whole [8, 9]. The different sources as well as direct and indirect effects of aerosols in the Earth's climate system are summarized in figure 1.3. Short-wave radiation from the Sun is illustrated in yellow and long-wave telluric radiation in red. Atmospheric aerosols will interact with both radiations by absorbing, scattering or reflecting them.

#### 1.1.2.1 Direct effects of aerosols on radiative forcing

The Intergovernmental Panel on Climate Change (IPCC) has shown in its successive reports that aerosols have a strong influence on the climate system. Aerosols directly impact the radiative energy balance by scattering and absorbing short and long wave radiation [10].

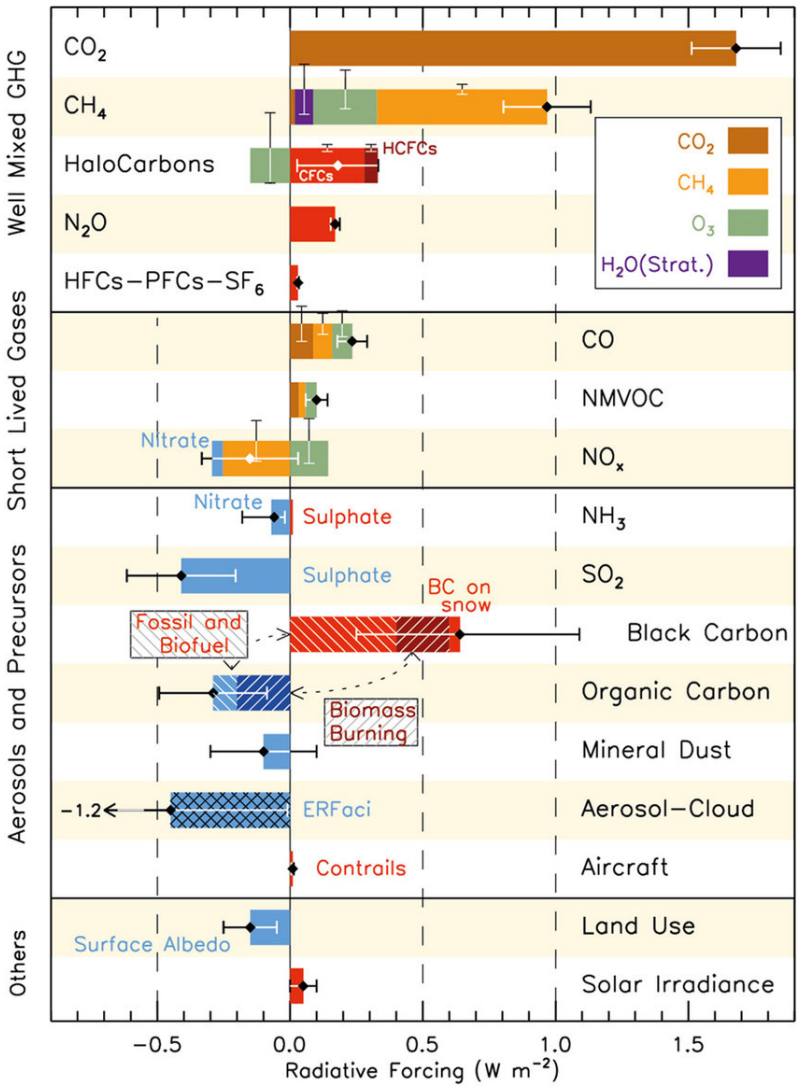


Figure 1.4: Radiative forcing of different aerosols and gas types and their uncertainties from [11])

Figure 1.4 gives an overall picture of the radiative forcing of different aerosol types and their uncertainties on a global scale. The effects that aerosols have on the radiative balance are strongly linked to the physicochemical composition of the particles present. Most atmospheric aerosols contribute to the cooling of the planet through their ability to reflect sunlight back into space and scatter incoming solar radiation. In contrast, black carbon and organic carbon aerosols have a warming effect on the climate. Black carbon, which is produced from incomplete combustion of fossil fuels and biomass, absorbs solar radiation and converts it into heat. When black carbon particles settle on snow and ice, they darken the surface, reducing its albedo (reflectivity) and causing it to absorb more solar energy. This accelerates melting and contributes to regional warming. Nevertheless, the average radiative forcing of aerosols across the globe has been estimated to be between -0.1 and -1.9 W.m$^2$, with the best estimate being -0.9 W.m$^2$, indicating that the overall cooling effects of aerosols could counteract the warming effects caused by increased greenhouse gases, such as carbon dioxide (1.82 +/- 0.19 W.m$^2$) [11, 12].

The IPCC Sixth Assessment Report [13] confirms that the magnitude of negative direct aerosol forcing has gradually decreased over the years. The climate model from NASA's Goddard Institute for Space Studies, carried out on four future scenarios, demonstrated that this reduction accelerates global warming [14]. In addition, the absorption of solar and telluric radiation, particularly by dust aerosols, can modify the stability in the local atmospheric environment [15].

#### 1.1.2.2 Indirect Effects of Aerosols on Cloud Microphysics and Radiative Forcing

In addition to the induced changes in the energy balance, aerosols interfere with the micro-physical and optical properties of clouds and have consequences on convection, evaporation and precipitation [16]. Indirect effects of aerosols consist firstly of an increase in droplet number concentration with aerosol number concentration and a simultaneous decrease in droplet size [17]. The distribution of the same cloud liquid water content over more and smaller cloud droplets leads to higher cloud reflectivity, i.e. an increase in the overall albedo and contribute to the cooling of the Earth. Furthermore, reducing the size of droplets in clouds affects the efficiency of precipitation and therefore increases the lifetime of clouds.

Aerosols can also affect clouds and precipitation by modifying radiation directly and by serving as cloud condensation nuclei or ice nuclei. In particular, aerosols can enhance cloud evaporation and then suppress the formation of clouds and precipitation by absorbing solar radiation [18].

The indirect impact of aerosols on cloud microphysics induces changes in their radiative properties as well. Nonetheless, the magnitude of the radiative forcing caused by these indirect effects is uncertain because the cloud modification process is highly variable [19].

#### 1.1.2.3 Air quality and health effects

Their small sizes make aerosols easy to penetrate the respiratory system and have harmful effects on human health in the short and long term [20]. Their repercussions in the human body will depend on their sizes at the time of inhalation. For example, particles with a diameter of less than 2.5 μm can penetrate deep branches of the respiratory tract and spread throughout the body. Once in the respiratory tract, the particles interact with each other to affect blood and brain cells [21]. Fetuses, newborns, children, the elderly, and anyone suffering from cardiovascular or respiratory pathology and diabetes are the most sensitive populations to aerosols. Furthermore, the World Health Organization (WHO) has stated that the penetration of these particles into the human body can cause asthma, stroke, heart disease, bronchial and lung cancer and adverse consequences on pregnancy [22]. Therefore, global monitoring of air pollution is essential to prevent health and climate effects of aerosols.

### 1.1.3 Atmospheric aerosols analysis and monitoring

Chemical, microphysical and optical parameters of aerosols are measured with local samples taken either on the ground or at altitude by air or by remote sensing. These may involve photometric measurements from the ground, massive concentration measurements carried out within the framework of air quality monitoring networks or satellite measurements [23]. For example, the Earth Surface Mineral Dust (EMIT) mission was launched at the International Space Station in July 2022. The goals of EMIT are to measure the spectral signatures of minerals from dust sources to update soil composition in order to better understand and reduce related uncertainties in radiative forcing of mineral dust aerosols at local, regional and global levels in the 400-2500 nm range [24].

Another example is the NASA's Plankton, Aerosol, Cloud, Ocean Ecosystem (PACE) mission launched in February 2024 that provides measurements of the optical properties of clouds and aerosols. The measurements are carried out with two polarimeters that measure how the oscillation of sunlight within a geometric plane is changed by passing through clouds and aerosols in the 385-770 nm range [25].

Finally, the Far-infrared Outgoing Radiation Understanding and Monitoring (FORUM) mission, which will be launched in 2027, aims to measure the emission spectrum of the Earth at the top of the atmosphere in the spectral region of 100 to 1.600 $cm^{-1}$ (i.e. 6.25 to 100 μm, corresponding to 3 THz to 48 THz) [26]. While the primary goal of these measurements is to monitor gases in the atmosphere, the data may also be used to study aerosols. This is achieved by comparing the observed spectra with those obtained through laboratory experiments in the THz range. Recently, a new method was developed that links laboratory data and Infrared Atmospheric Sounding measurements to extract information about min-

eral dust aerosols in the infrared region [27]. Figure 1.5 illustrates the spectral region that will be explored by the FORUM mission. This mission raises the importance and the urgency of measuring the optical properties of aerosols in the THz domain in laboratory experiments.

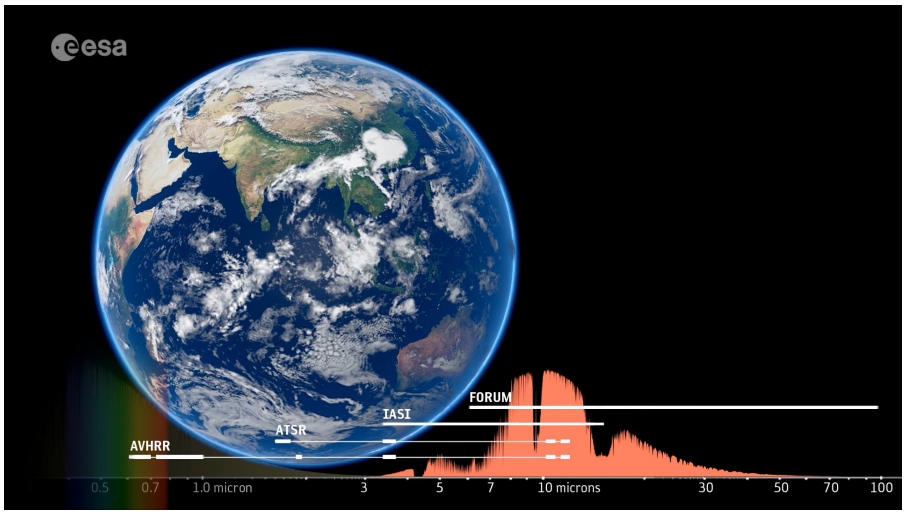


Figure 1.5: Spectral region that will be explored by the Far-infrared Outgoing Radiation Understanding and Monitoring (FORUM) mission (from [28]).

## 1.2 Desert dust

### 1.2.1 Formation and emission of desert dust aerosols

Atmospheric mineral dust arises primarily from wind erosion of soils in arid and semi-arid regions of the Earth and is composed of rock mineral fragments and other soil constituents. Most emissions come from the so-called dust belt: the arid regions of North Africa, the Arabian Peninsula, Central Asia and China [29]. Estimates of global dust emissions can vary considerably between models due to invaluable differences in size ranges. However, the quantity of dust particles with a geometric diameter of less than 20 µm emitted into the atmosphere is estimated at 5.000 Tg.year$^{-1}$ [30].

Desert dust is entrained into the air when surface wind speed creates enough aerodynamic drag to dislodge and lift particles from the soil. Therefore, the finest particles (less than 60 µm) are small enough to be suspended upwards by turbulent eddies and can be transported away from the sources. The particles that are emitted are generally transported thousands of kilometers [31]. Particles ranging in size from 60 to 2000 µm can be lifted by the vortices to a height of a few centimeters. They will be too heavy to reach the atmosphere and will be brought back to the surface. These particles are called in saltation. When a saltating particle hits a soil dust aggregate, the impact can break the interparticle bonds between the particles in the dust aggregate. Collections of smaller particles are created by

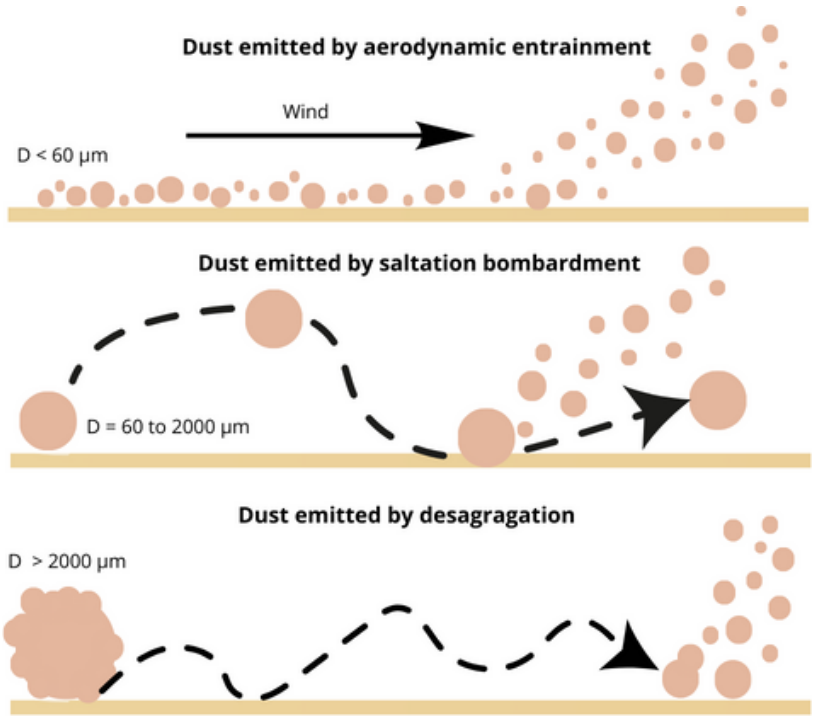


Figure 1.6: Emission processes of desert dust.

this fragmentation and are suspended [32]. Particles that are too large (greater than 2000 µm) will roll and crawl along the surface [33]. However, the lifetime of super coarse aerosols is generally underestimated in studies, due to the underestimation of the emission of super coarse dust [34]. The three different emission processes are explained on the figure 1.6.

### 1.2.2 Size distribution and chemical composition

The particle size distribution of the dust emitted depends on the physical process of dust emission. Aerosols can have different sizes and varied shapes (spherical, spheroids, etc.), which can have an effect on radiation absorption, reflection and scattering. There is still a high uncertainty regarding the emission of particles larger than 10 µm, whose contribution to transport and climate is considered underestimated due to the lack of field data [35]. Aerial measurement campaigns have revealed that dust with a diameter > 10 µm represents approximately a quarter of the mass of aerosols present in the atmosphere [34].

Aerosols often coagulate to form complex heterogeneous mixtures. However, the particles will have different impacts depending on whether they are mixed externally or internally. Figure 1.7 illustrates the different mixtures in a set of particles. In an external mixture, the aerosol population comprises particles with distinct chemical compositions. Each particle has its own unique refractive index depending on its composition, which influences its light scattering properties. For

instance, sulfate aerosols, which are light-colored and primarily reflective, scatter incoming solar radiation in all directions more effectively than black carbon, which is darker and absorbs more radiation. Additionally, different aerosol species absorb light at specific wavelengths. For example, black carbon exhibits strong absorption in the visible and near-infrared regions, while organic aerosols may absorb light in the ultraviolet range. This diversity in absorption characteristics leads to a complex interplay of light interactions based on the relative concentrations of the various particles in the external mixture. The internally mixed particles can be of different types, for example binary or ternary [36]. In internal mixtures, light-absorbing components, such as black carbon, are combined with scattering components like sulfates or organic matter. This internal mixing can significantly enhance the overall absorption of the aerosol mixture, often exceeding that of any individual component alone. This phenomenon arises from the effective "coating" of absorbing particles by non-absorbing ones, which alters how light penetrates and interacts with the aerosol. The resulting structure leads to improved light absorption due to multiple scattering events and increased effective surface area, thereby enhancing the optical properties of the internal mixture.

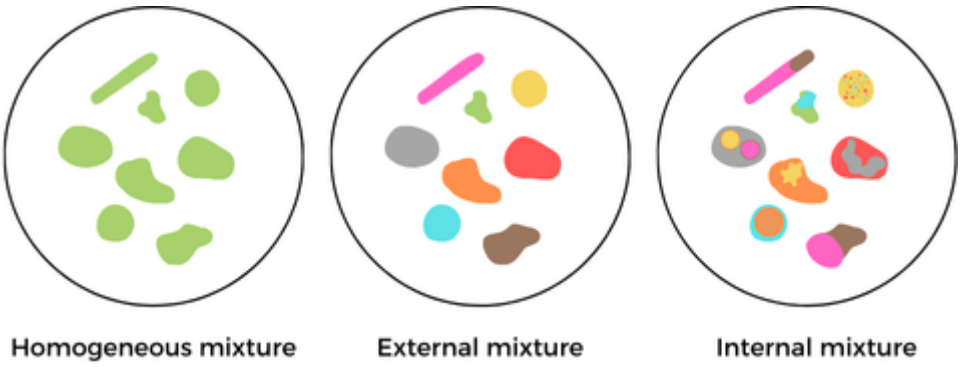


Figure 1.7: Homogeneous, external and internal mixture in particles mineralogical composition.

In summary, understanding the differences between external and internal mixtures is essential for accurately characterizing the optical behavior of aerosols and their implications for climate and air quality.

However, it is important to specify that these mixtures are defined according to selection criteria. If compounds in small percentages were not neglected, each atmospheric particle would be unique in its composition. Even if the particles are individually pure when first produced, there are numerous reactions and aging processes in the atmosphere which will modify their chemical composition and which convert an external mixture into an internal mixture [37]. For example, calcite-containing dust from China reacts with nitric acid to form a nitrate salt, causing increased adsorption of water vapor and therefore an increase in particle size [38]. Mass estimates of the elementary components of the aerosol can be used to determine the extent of internal mixing relative to external mixing by calculating the mixing state index. Results from an aerosol study in Alabama

showed that neither external nor internal mixing fully represents the mixing state of atmospheric aerosols in a real-world situation [39].

Asian dust contains a large amount of mineral dust composed of major metal oxides, $SiO_2$, $Al_2O_3$, CaO and $Fe_2O_3$ with smaller amounts of $K_2O$, $Na_2O$, MgO, $P_2O_5$, $SO_3$ and $TiO_2$. Although these minerals are typically dominant components in desert dust from other regions around the world, the concentration of calcite ($CaCO_3$) is a known characteristic to distinguish the origin of desert dust. Calcite is a significant constituent of dust found in both Asian and Saharan deserts, where it plays a major role in the overall mineral composition. However, in Australian desert dusts, calcite is present only in smaller amounts, typically as trace component. This difference in calcite concentration across these desert regions is likely due to variations in the geological makeup and weathering processes of the respective areas.

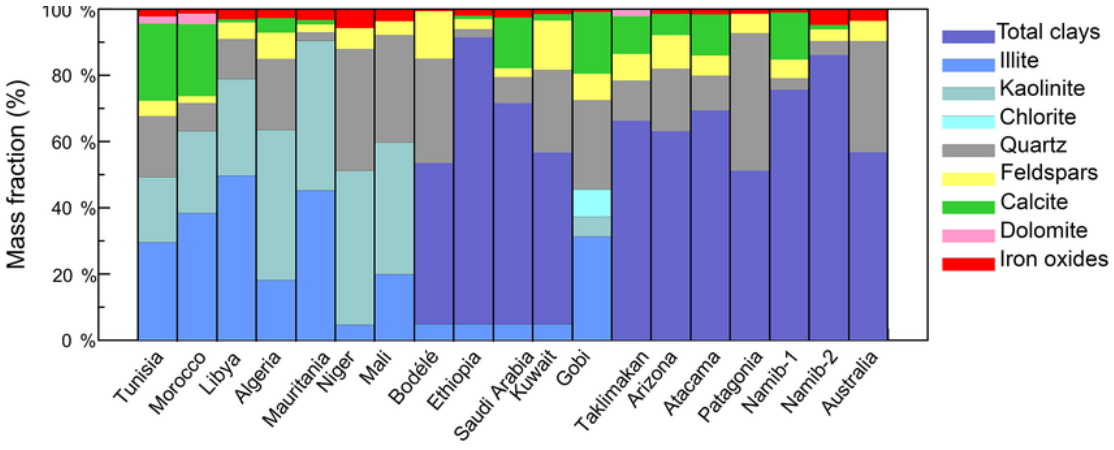


Figure 1.8: Mass fractions of illite, kaolinite, chlorite, quartz, feldpars, calcite, dolomite and iron oxides are shown for northern African (Tunisia, Morocco, Libya, Mauritania, Niger, Mali, Bodélé), eastern Asian (Gobi, Taklimakan) and Australian aerosols, from [41]

.

For instance, unaged Gobi Desert particles are composed of 46% illite, 7% montmorillonite, 15% quartz, 13% feldspars, 12% calcite, 6% anhydrite and aged particles are composed of 52% illite, 8% montmorillonite, 15% quartz, 2% feldspars, 14% calcite, 9% anhydrite based on linear spectral mixing analysis measurements (LSM) [40]. However, the composition may depend on the analysis method used. In this study, the authors compared the results obtained with X-ray diffraction (XRD) with the LSM method where each observed spectrum is assumed to result from a linear combination of a small number of endmembers. In the case of LSM, possible differences in size, morphology and chemical state between the reference minerals and the actual minerals can affect the analysis, which highlights the importance of working directly with spectra of minerals that have been resuspended. Another study [41] on northern African (Tunisia, Morocco, Libya, Mauritania, Niger, Mali, Bodélé) and eastern Asian (Gobi, Taklimakan) aerosols (figure 1.8) estimated the particles' mineralogical composition by the combination

of XRD, wavelength dispersive X-ray fluorescence (WD-XRF) and X-ray absorption near-edge structure (XANES). These estimations emphasize the diversity of dust compositions by illustrating the different minerals mass fractions such as illite, kaolinite, quartz or calcite.

### 1.2.3 Impact of desert dust aerosols

The impacts of desert dust on the Earth system are spatially heterogeneous, not only because the dust loading itself varies considerably between regions, but also because the properties of the dust depend on the mineralogy , which varies depending on the region of origin [30]. Globally, mineral dust is estimated to warm the atmosphere and cool the Earth's surface in the short-wave spectral range and induce opposite effects in the long-wave spectral range. However, uncertainties remain regarding the direct radiative effect of dust due to uncertainties about their compositions and their evolution during transport [42]. This radiative effect is in fact closely linked to the composition of the minerals present in the desert particles. For example, the presence of quartz and calcite in its composition will affect the radiative effect in the long wave bands [43]. Other parameters can also be impacted by the shape and chemical composition of desert dust, such as atmospheric chemical reactions or the absorption of liquid water and the nucleation capacity of the dust. Eight minerals (illite, kaolinite, smectite, hematite, quartz, calcite, gypsum, and feldspar) were identified as climatically important by treating desert dust as an external mixture of minerals with the Community Earth System Model (CESM) [44]. Some of these minerals will be studied as part of this thesis, in Chapter 3.

Furthermore, the transport of "giant" dust particles (diameter greater than 20 µm) remains a representation problem that is unresolved. The size of the particle will strongly affect its absorption and scattering efficiency depending on the spectral range despite its shorter lifetime. The chemical composition of aerosols is a key factor that defines their intrinsic optical properties. These properties are quantified by the complex refractive index, which governs how aerosols absorb and scatter light. Particle size, in turn, dictates how these optical effects manifest at different wavelengths, ultimately influencing the aerosols' radiative impact on climate. However, the particle diameters typically measured and incorporated into models rarely exceed 20 µm, despite recent evidence showing that particles larger than 20 µm are prevalent in the Sahara and its downwind export regions [45]. The growth in particle size and the evolution of their chemical compositions during the aging process also modify the optical properties [46]. These factors underscore the need for improved measurements and models that account for the presence of larger particles and their evolving optical properties, which are crucial for accurately assessing the climate impact of desert dust on both regional and global scales.

It has also been shown that desert dust can inhibit or promote the new particle formation process by participating in atmospheric reactions. For instance, it was revealed that $TiO_2$ and $Fe_2O$ act as photocatalysts and could promote the heterogeneous oxidation of $SO_2$ and the subsequent formation of gaseous $H_2SO_4$. These components, acting as catalysts, are not consumed in the photocatalytic reaction and can repeatedly accelerate atmospheric photochemistry [47].

### 1.2.4 Gobi Desert

The Gobi Desert (GD) is the largest desert in Asia with an area of around 1.3 million square km above northern and northwestern China and southern Mongolia, and the $5^{th}$ largest desert in the world. The desert is composed of five distinct eco-regions: the Gaxun Gobi, Junggar Gobi, and Trans-Altai Gobi in the west; the Eastern or Mongolian Gobi in the centre and east; and the Alxa Plateau or Ala Shan Desert in the south. Its name is derived from the Mongolian word 'gobi' – meaning 'waterless place'. Sandy desert only accounts for around five per cent of the Gobi, with the majority of the desert being bare rock. Despite this, the Gobi is home to one of the world's biggest sand dunes, the Khongor Sand Dunes (i.e 80 metres high, and 180km long) [48].

The Gobi and desert regions of northwest China are among the major sources of dust aerosols in East Asia. The most recent model calculations indicate that global mineral dust emissions from wind erosion (i.e. between 1000 and 3000 $Mt.yr^{-1}$) account for about half of annual particulate emissions at worldwide [49]. It is estimated that between 100 $Mt.yr^{-1}$ and 460 $Mt.yr^{-1}$ of dust particles are emitted into the atmosphere by GD and the deserts of northern China each year [50]. It has been shown from reports of dust storms from 1960 to 1999, that GD is the major source of dust from East Asia [51]. Furthermore, Chen et al investigated a typical dust storm event that occurred from 18 to 23 March 2010 and attested that GD was the main contributor to the dust concentration over South Asia during the first stage of the storm (18-20 March 2010) [52]. Nevertheless, the importance of GD emissions tends to be, in general, underestimated.

## 1.3 Optical properties of aerosols

The Earth's atmosphere is constantly exposed to radiation from various sources, such as sunlight, terrestrial radiation, moonlight, starlight, and artificial lighting. As this radiation passes through the atmosphere, it interacts with both gas molecules and suspended particles, leading to a variety of optical phenomena, including scattering, absorption, diffraction, and reflection. These interactions are responsible for observable effects such as the blue color of the sky, the formation of white clouds, and the appearance of rainbows (see Figure 1.9). In atmospheric science, the combined processes of scattering and absorption are often referred

to as extinction, as they describe the attenuation of light as it travels through the atmosphere.

Aerosols, which are tiny particles suspended in the air, play a crucial role in extinction processes. The optical properties of aerosols are primarily influenced by several key factors: the particle size distribution, the complex refractive index, and the assumption of particle shape (often simplified as spherical for modeling purposes). However, real-world aerosols—such as desert dust, sea salt, or industrial pollutants—display significant variability in both size and refractive index, even within the same class of aerosols. For instance, desert dust particles can vary widely in size, composition, and morphology, leading to different optical behaviors across various datasets, such as the Optical Properties of Aerosols and Clouds (OPAC) database [53] and the Aerosol Refractive Index Archive (ARIA) [54].

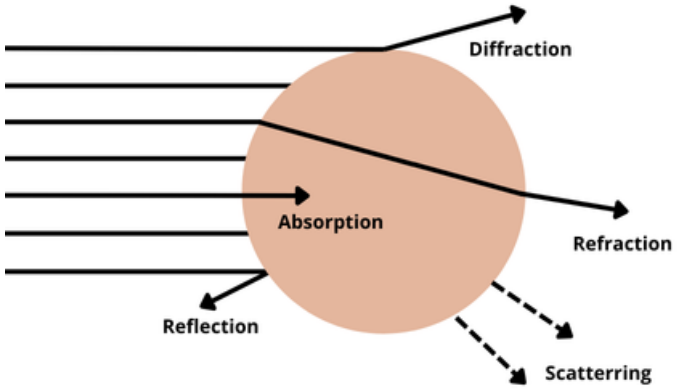


Figure 1.9: Interaction between an incident radiation and a homogeneous and spherical aerosol particle.

Most global aerosol models make the simplifying assumption that dust particles are spherical, despite the fact that many atmospheric particles, such as mineral dust, have irregular, non-spherical shapes. This assumption leads to significant underestimations of key optical parameters, including extinction efficiency, mass extinction efficiency, single scattering albedo, and asymmetry parameters, particularly across a broad range of dust sizes in both the shortwave and longwave spectra [55]. For example, spherical models often fail to account for the enhanced scattering of light by larger, non-spherical dust particles, which can lead to inaccuracies in climate models and radiative forcing estimates.

To describe the interaction between light and atmospheric particles, two primary scattering theories are used: Mie scattering and Rayleigh scattering.

### 1.3.1 Mie and Rayleigh theories

Any particle can be divided into smaller regions, termed scatterers. When illuminated by incident radiation, a dipole moment is induced in each scatterer, causing the particle to scatter light in multiple directions. Absorption occurs due to the

damping of dipole oscillations and the conversion of electromagnetic energy into thermal energy.

The scattering and absorption cross sections of individual scatterers are a measure of a probability of scattering or absorption processes for a particle. The efficiency of scattering and absorption is defined as the ratio of the effective section to the geometric surface $\pi a^2$ of a sphere. These cross sections can be defined as:

$$\sigma_{abs} = \pi a^2 Q_{abs} \tag{1.1}$$

$$\sigma_{scat} = \pi a^2 Q_{scat} \tag{1.2}$$

$$\sigma_{ext} = \sigma_{abs} + \sigma_{scat} \tag{1.3}$$

- $\sigma_{abs}$, $\sigma_{scat}$ and $\sigma_{ext}$ absorption, scattering and extinction cross sections in $m^2$.
- $Q_{abs}$ and $Q_{scat}$, absorption and scattering efficiencies, dimensionless.

The regime of scattering is defined in function of the size parameter, that is calculated as follows:

$$X = \frac{2\pi n a}{\lambda} \tag{1.4}$$

With :

- $n$ the refraction index of the medium, typically $n$=1 for air.
- $a$ the radius of the particle in m.
- $\lambda$ the wavelength of the incident light in m.

Figure 1.10 classifies the scattering type based on the particle size parameter, particle radius, and wavelength.

Mie theory applies when the size parameter $X$ is approximately 1, meaning the particle size is similar to the wavelength. In contrast, if $X$ is much less than 1, indicating that particles are small relative to the wavelength, Rayleigh Scattering applies [57]. The interplay between induced dipole moments and electromagnetic waves explains the wavelength dependence of both Rayleigh scattering and absorption. The well-known wavelength dependence of the Rayleigh scattering cross-section, given by $\lambda^{-4}$, and the less-known wavelength dependence of the Rayleigh absorption cross-section, $\lambda^{-1}$, are derived from electromagnetic oscillator theory in the long-wavelength approximation [58]. For particles significantly larger than the wavelength, the Geometric Regime applies, where the scattering can be approximated by tracing independent parallel rays, treating electromagnetic waves as localized due to the size difference.

Both Mie and Rayleigh theories assume that aerosol particles are spherical. However, many real-world aerosol particles have irregular shapes due to their formation processes, aggregation, or chemical reactions. Non-spherical particles scatter light differently, which can lead to inaccuracies in predicted optical properties. In addition, Mie and Rayleigh theories typically assume that aerosol particles

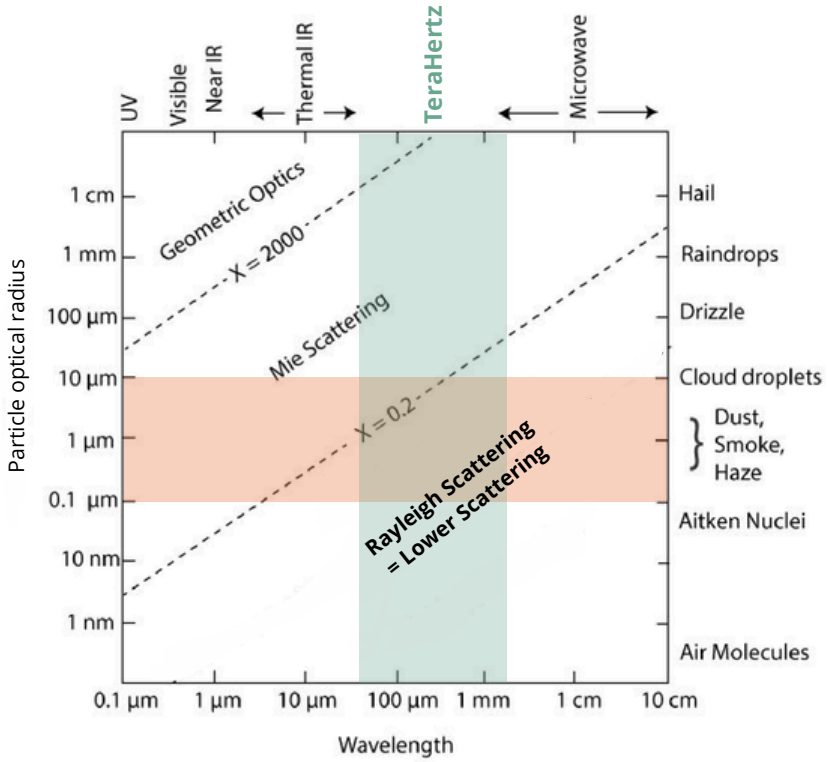


Figure 1.10: Graph of size parameter X and type of scattering as a function of radiation wavelength and particle radius [56]. The THz range is highlighted in green and the measured particle optical radius range is highlighted in orange.

are homogeneous in composition. In reality, aerosols can be mixtures of different materials (e.g., soot, sulfate, organic compounds), which can affect their optical properties significantly.

In this study, since the particles are relatively small compared to the wavelength, the Rayleigh regime is the primary focus. However, in real-world scenarios, many aerosol particles exist within the size range where Mie theory becomes applicable, even though Rayleigh theory is often primarily referenced. This shift complicates the predictions of their optical properties. In addition, While Mie and Rayleigh theories provide a good starting point, the complexity of real-world aerosol systems often necessitates advanced computational methods (such as numerical solutions to the Maxwell equations or ray-tracing techniques) to accurately model their optical properties.

This complexity highlights the necessity of comprehending the intricate interactions that shape the optical properties of aerosols. As a result, complex refractive indices, along with absorption and scattering cross sections, become essential parameters for calculating the planet's radiative balance. These factors are crucial in assessing the influence that various groups of atmospheric aerosols can have on

climate, particularly considering that absorbed light can be converted into heat, thereby affecting temperature and energy dynamics in the atmosphere [59].

### 1.3.2 Complex refractive index

The propagation of light in absorbing materials can be entirely characterized by the complex refractive indices (CRI) specific to each wavelength. Nearly all micro and nanoparticle monitoring methods are based on optical properties, which are represented by the CRI of the particle [60].

The CRI of a material is related to its relative permittivity according to the following formula :

$$\tilde{n} = \sqrt{\epsilon_r} \tag{1.5}$$

With :

- $\tilde{n}$ the CRI.
- $\epsilon_r$, the complex relative permittivity.

The imaginary part of the CRI relates to the absorption and losses, while the real part is linked to the phase velocity and refraction. The CRI is dependent on the wavelength and the size and shape of a particle for the same chemical composition [61]. The real and imaginary part of the CRI can be defined as :

$$\tilde{n}(\lambda) = n(\lambda) - i\kappa(\lambda) \tag{1.6}$$

With :

- $n$ the real part of the CRI, which is the ratio of light velocity in a vacuum to light velocity in the particle.
- $\kappa$ the imaginary part of m that describes the absorption of light by the particle.
- $\lambda$ the wavelength of the incident radiation in m.

The samples in this study are diluted and their absorption is consequently low, which allows the imaginary part of the CRI to be related to the absorption coefficient according to the Beer-Lambert law :

$$\alpha = \frac{4\pi\kappa}{\lambda} \tag{1.7}$$

With $\alpha$ the absorption coefficient in $m^{-1}$.

In anisotropic optical materials (i.e. birefringent) such as calcite and quartz, the refractive index generally depends on the direction of polarization and the direction of propagation. In addition, certain relative permittivities can be negative, notably for certain photonic metamaterials or for particles presenting polaritons in crystals. These phenomena are essentially perceptible in microwave and far-infrared regions [62].

### 1.3.3 Polaritons

Polaritons are hybrid quasiparticles formed from the coupling of photons with other excitations. They can manifest as exciton-polaritons in semiconductors, plasmon-polaritons in doped materials, and phonon-polaritons in solids, which arise from the interaction between phonons (collective vibrations of the atomic lattice) and photons [63]. This study will primarily focus on phonon-polaritons, particularly in the infrared and terahertz (THz) regions, where their effects are most pronounced.

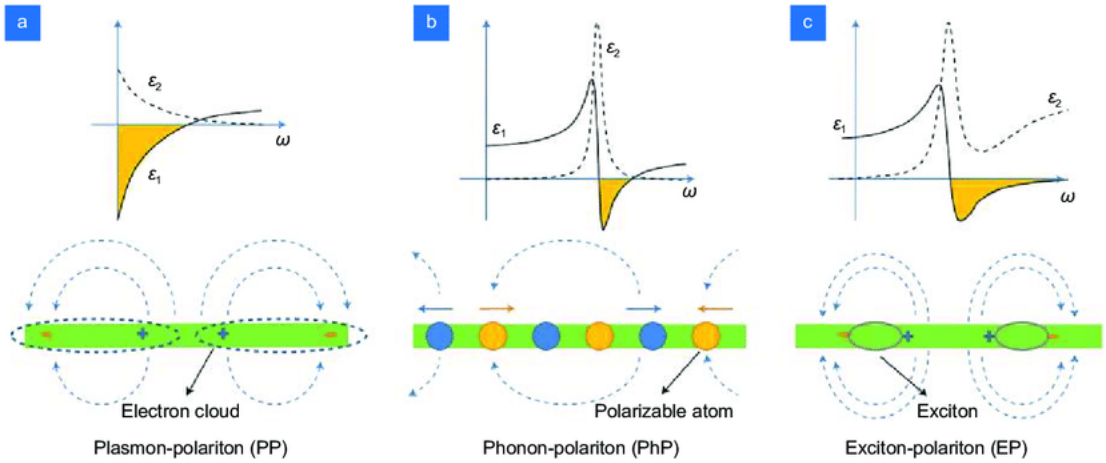


Figure 1.11: Polaritons with different dielectric functions and electric field line distributions. (a) Plasmon-polariton, (b) phonon-polariton, and (c) exciton-polariton. $\epsilon_1$ represents the real part of permittivity, $\epsilon_2$ imaginary part, and $\omega$ angular frequency of light, from [65].

Figure 1.11 illustrates the various types of polaritons, highlighting their dielectric constants and complex permittivities. In the context of phonon-polaritons, negative permittivity arises from resonant optical absorption, which occurs when the frequency of incident light matches the natural vibrational frequencies of the material's phonons. This resonance is indicative of highly dispersive permittivity behavior, where the material's response to electromagnetic fields varies significantly with frequency. In such dispersive media, the permittivity is not constant but instead changes over a range of wavelengths, resulting in complex interactions between light and matter.

The interplay between negative permittivity and dispersive characteristics contributes to the formation of a reduced modal volume. The modal volume refers to the effective volume in which the electromagnetic field can exist around the polariton. A reduced modal volume signifies that the electromagnetic field is highly localized, resulting in an exceptionally high local density of electromagnetic states at the interface between light and the material. This high density enhances light-matter interactions, allowing for more efficient coupling and stronger effects in phenomena such as polaritonic chemistry and enhanced radiative processes. Consequently, this strong coupling can significantly influence the optical properties

of materials, particularly in applications involving photonic devices and energy transfer mechanisms.

Such strong coupling between light and matter is a focal point of ongoing research, particularly in its implications for polaritonic chemistry and photochemistry, where these interactions can influence chemical reactions in novel ways. Moreover, they are being explored for applications such as radiative cooling materials, leveraging their unique optical properties to enhance thermal management strategies [64].

Recent studies have investigated the polaritonic eigenmodes of water droplets representative of natural atmospheric conditions using Mie theory and infrared spectroscopy [66]. Notably, it has been demonstrated that water droplets with radii greater than approximately 2.7 µm exhibit polaritonic behavior, extending into the ultra-strong coupling regime. As we delve into the ramifications of these polaritonic phenomena on the Earth's radiative balance, it becomes crucial to broaden our focus to additional spectral ranges that significantly affect atmospheric interactions, including the THz frequency domain, positioned between the infrared and microwave regions of the electromagnetic spectrum.

## 1.4 TeraHertz frequencies

### 1.4.1 Definition and properties

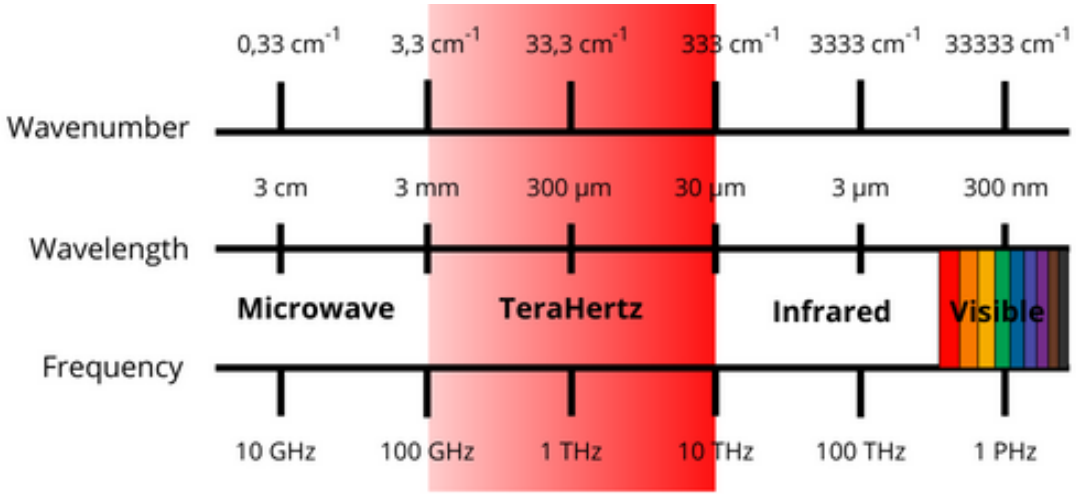


Figure 1.12: Location of THz band in the electromagnetic spectrum.

The Terahertz (THz) range of electromagnetic waves is defined by frequencies between 100 gigahertz ($10^{11}$ Hz) and 10 terahertz ($10^{13}$ Hz) [67]. This domain is located between infrared and microwaves and is sometimes called far infrared or "T-rays". After its discovery in 1911, research was significantly hampered because the development of powerful and compact sources only really began with the emergence of microelectronics and nanotechnologies at the end of the 20th

century [68]. The location of the THz band is shown on figure 1.12. 1 THz is equal to 33.3 $cm^{-1}$ in wavenumber and 300 μm in wavelength.

THz radiation is emitted as a component of black-body radiation from terrestrial objects, which typically have physical temperatures ranging from approximately 273 K (0 °C) to 300 K (27 °C). According to Planck's law of black-body radiation, any object at a given temperature emits radiation across a broad spectrum of wavelengths, with the intensity and distribution of that radiation influenced by its temperature. For terrestrial objects, the peak emission occurs between approximately 8 and 10 μm [69]. The presence of THz radiation in the spectral output of these objects is crucial, as it significantly affects various atmospheric processes, including energy balance and radiative transfer within the Earth's atmosphere.

### 1.4.2 Applications: From Material Analysis to Atmospheric Studies

The interest of terahertz waves is linked to their penetrating power since they allow visualization through certain materials and in particular skin, clothing, wood and plastics, while being strongly absorbed or reflected by others. In addition, THz spectroscopy is a powerful tool for characterizing collective excitation modes in a periodic arrangement of atoms constituting a crystalline or amorphous structure i.e. phonons [70]. Terahertz rays have also very varied applications in astronomy, security and telecommunications [71]. Since THz radiation is sensitive to the environment of the molecules and their chirality, it potentially offers a means of detecting different polymorphs [72].

Another additional benefit is that samples can be analyzed in solid, liquid or gaseous state. THz spectroscopy on gases is several times more sensitive than microwave spectroscopy and has better resolution than infrared spectroscopy due to weaker Doppler effects [73, 74]. Morevoer, the dielectric properties of liquids in the THz range mainly depend on the interaction and relaxation of permanent or induced dipoles inside a liquid. As expected, water and aqueous solutions are the most studied liquids, mainly for biological applications [1]. Solid samples can take different shapes, such as films, plates or pellets. Powder samples, inter alia, are generally prepared by mixing a non-absorbent powder (i.e. polyethylene), grinding it to a fine powder and finally preparing the resulting composite as a pressed pellet [75].

**THz for atmospheric purposes** Gases with a dipole moment and dielectric materials present in our atmosphere exhibit distinct spectral signatures and diverse optical characteristics within the THz range [76]. This enables THz waves to perform precise quantitative analyses of atmospheric composition and structure [77]. For example, the THz range is ideal for remote sensing of the diurnal behavior of stratospheric OH [78]. Moreover, THz remote sensing extends beyond Earth, providing insights into the physical and chemical processes within the atmospheres

of planets like Venus, Mars, and the Jovian planets, while passive THz studies on Earth enhance our understanding of the telluric environment [79].

### 1.4.3 THz generation and spectroscopy techniques

This section focuses on optical and opto-electronic methods, although numerous techniques exist for the generation and detection of THz frequencies.

One approach to generating THz frequencies involves the use of a nonlinear crystal with high electro-optical coefficients, operating via optical rectification. This process creates quasi-DC polarization due to the preferred direction within the nonlinear medium [80]. Optical rectification allows for the generation of pulses with an extremely wide bandwidth, constrained by the bandwidth of the optical pulse used [81]. Another method, photomixing, relies on the interference of two continuous-wave optical laser beams tuned to different wavelengths. When these beams are superimposed on an ultrafast photodetector, they generate continuous THz radiation. The frequency of the resulting beat signal equals the difference between the two laser frequencies. This photocurrent is then directed through a broadband antenna, emitting the THz beam.

Fourier-transform infrared spectrometers (FTIR) can be equipped with far-infrared extension modules, which allow measurements down to 10 $cm^{-1}$. This progress enables the use of FIR or THz spectroscopy, depending on the experimental requirements [82]. Large synchrotron sources can also be coupled with FTIR instruments. Recently, successful heterodyning between a synchrotron source and a gas laser was achieved [83].

Two widely used laser-based techniques for THz generation and detection are THz time-domain spectroscopy (THz-TDS) and time-resolved THz spectroscopy (TRTS). In TRTS, the sample (semiconductor) is excited by an fs laser pump pulse, generating electron-hole pairs that absorb the THz probe radiation. This absorption, measured as a decrease in transmitted THz power, allows for the extraction of the time-dependent THz spectrum through a typical pump-probe experiment.

In THz-TDS, THz pulses are generated by transient currents in photoconductive antennas, induced by illumination with a femtosecond (fs) laser. Photocarriers accelerated by a static electric field create a transient polarization in the semiconductor. This process is explained in detail in Chapter 2. THz time-domain spectroscopy is particularly interesting for optical characterization of aerosols as it provides a direct measurement of the electric field E(t), rather than the intensity (squared electric field) as in Fourier-transform infrared spectroscopy (FTIR). This technique enables access to both the amplitude and phase of the electric field in the frequency domain via Fourier transformation, eliminating the need for Kramers-Krönig relations to extract parameters such as complex refractive indices [84]. THz-TDS provides a powerful combination of broadband spectral coverage, direct electric field measurement, and sensitivity to water and small par-

ticles, making it the ideal choice for studying atmospheric aerosols in controlled laboratory environments. Additionnaly, THz-TDS systems can be adapted to a variety of sample environments, such as controlled humidity, pressure, and temperature, which are important for simulating real atmospheric conditions. This technique provides also time-resolved data, allowing for the observation of dynamic changes in the aerosol properties, such as particle growth, chemical reactions, or phase transitions under controlled conditions. Therefore, THz-TDS emerges as an ideal tool for conducting precise and repeatable measurements of aerosols across varying environmental conditions.

This table provides an overview of the various techniques in terms of their resolution, frequency range, cost, and other key factors.

| Technique | Spectral Resolution | Frequency Range | Output Power | Price Range | Advantages | Limitations |
|---|---|---|---|---|---|---|
| Optical Rectification | 10 GHz - 100 GHz | 0.1 - 5 THz | Low to moderate (µW) | Moderate to high | Wide bandwidth, broadband generation | Limited output power |
| Photomixing | 0.1 MHz - 10 GHz | 0.1 - 3 THz | Continuous, low (nW to µW) | Moderate to high | Continuous wave THz, tunable frequency | Requires two lasers, complex setup |
| Time-Resolved THz Spectroscopy (TRTS) | 10 GHz - 100 GHz | 0.1 - 10 THz | Low (µW) | High | Allows for dynamic material studies | Complex, high cost |
| FTIR with Far-IR extension | 0.1 GHz - 10 GHz | 0.1 - 10 THz | Low to moderate (µW) | Moderate | Cost-effective for certain ranges | Limited by spectral resolution and range |
| Synchrotron Radiation | 0.1 GHz - 10 GHz | 0.1 - 50 THz (broad spectrum) | High (mW) | Very high | Extremely broad spectrum, high power | Expensive, limited access |
| Gas Laser (Heterodyne) | 10 MHz - 100 MHz | 0.1 - 10 THz (depends on gas) | Moderate (mW) | High | High power in narrow frequency bands | Narrow frequency range, expensive |
| THz Time-Domain Spectroscopy (TDS) | 100 MHz - 100 GHz | 0.1 - 10 THz | Low (µW) | High | Full electric field measurement, wide range | Requires fs lasers |

Table 1.1: Comparison of Optical and Opto-Electronic THz Generation Techniques

## 1.5 State of the art

As mentioned previously, atmospheric aerosols have never been studied in the THz range before. In this section, studies completed on samples of atmospheric interest and ranging from ultraviolet to far infrared will be examined. Then, far infrared and THz studies carried out on powders and pellets, and in particular resuspension achieved on particles with a diameter of the order of a few mm, will be reviewed.

**Dust aerosols studies in the UV-Infrared range** First of all, the CRI of kaolinite, which is one of the major compounds in Sahara Desert particles, has recently been extracted for the first time from far infrared (200 $cm^{-1}$) to ultraviolet (UV) (40,000 $cm^{-1}$) using an optimal estimation method (OEM) combined with diffusion theories and the unique subtractive Kramers–Kronig (SSKK) relationship following resuspension in the laboratory [85]. Quartz is another main component of desert dust particles. It was analyzed from UV (40,000 cm-1) to thermal infrared (650 cm-1) in a resuspended form. The quartz' ordinary and extraordinary CRI were then extracted with a numerical procedure coupling scattering theories, the single subtractive Kramers-Kronig relation, and an optimal estimation method in an iterative process [84]. Furthermore, Deschutter [3] analyzed resuspended Gobi Desert particles in a large spectral range (UV to infrared) and applied the linear combination to its compounds in order to reproduce the experimental extinction of Gobi Desert dust. Hence, this study demonstrated that the extinction of Gobi Desert dust in the infrared region can be recreated by the linear combination of its main components, that are illite, quartz and calcite. Figure 1.13 shows the reproduction of Gobi particles' extinction.

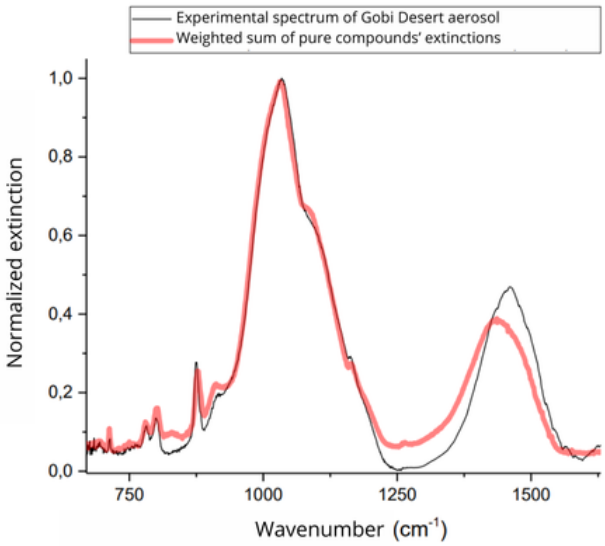


Figure 1.13: Linear combination of illite, quartz and calcite extinctions reproducing the experimental extinction spectrum of Gobi desert particles, from [3].

**THz Domain Studies on Mineral Particles and Powders** Mineral particles were also studied in the THz domain for pharmaceutical, industrial and environmental purposes. However, these studies have only been carried out on bulk materials, in the form of pellets or on more or less compact powder, but never on particles suspended in a gas as in atmospheric conditions. For instance, attenuated Total Reflectance Fourier transform Far-infrared measurements (0 to 700 $cm^{-1}$) were carried out on the main mineral groups (kaolinite, smectite, calcite, quartz, illite, albite and dolomite) that can be found in different shale types [86]. The samples were in a compact powder form to ensure reproducible ATR analysis. ATR THz-TDS methods were also used on powders to probe carbonate minerals' (calcite, aragonite and dolomite) optical responses in the 1-6 THz range [87]. The transmittance of carbonates minerals were also measured by FTIR. The samples were mixed in polyethylene pellets of 700 mg, 3 cm diameter and 1 mm thick [88].

Nonetheless, few studies aimed at resuspending particles or mimicking a suspension to extract their optical parameters in the THz domain. Particularly, the research carried out by Prophete [89] focuses on sand particles and glass beads of comparable size to the wavelength in the frequency band between 100 GHz and 2 THz. The measurements are performed with a commercial THz-TDS from Menlo systems. Prophete's aim was to characterize large particles that are suspended in brownout conditions of military helicopters, hence the particles are not representative of atmospheric conditions. The measurements were divided into three

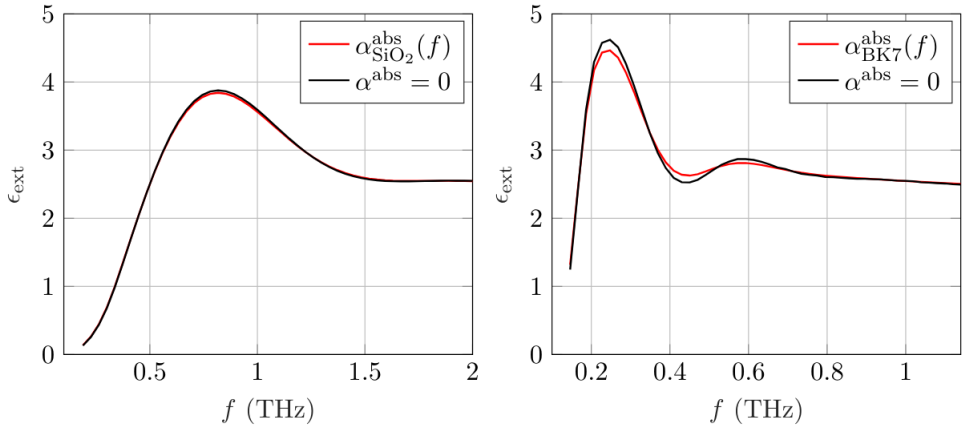


(a) Sable de Fontainebleau (b) Billes de verre

Figure 1.14: Extinction efficiencies as a function of frequency for (a) non-absorbing or absorbing real index 1.67 beads such as silica and (b) non-absorbing or absorbing beads with an index of 2.54 (BK7), measured by Prophete [89].

distinct parts: measurement in 2D on a static sample, in 3D on a static sample and finally in 3D on a dynamic sample. The 2D measurements on a static sample consisted of glass beads stuck on paper, or grains of sand placed on tape with a thickness of the support which is negligible compared to the size of the particles to limit their interaction. This study was similar to that of Fiorino [90] that

achieved TDS transmission measurements on sand samples whose sizes ranging from 177 to 550 µm. The particles were held in place using cellophane tape to mimic a suspension and investigate brownout conditions. The static 3D sample measurements consisted of a paraffin matrix containing the particles, as the paraffin is known to be transparent in the THz range. However, the manufacturing of these samples was not satisfactory because the adhesion between the grains of sand (or the glass beads) and the paraffin was not ensured because areas of air could form between the layers. In addition, neighboring paraffin layers were dissociable and reflections internal to the sample could take place at the interfaces. For measurements with dynamic 3D samples, a chamber composed of two cellophane windows and a ventilator which allows the sand particles to be lifted was set up. In figure 1.14, the extinction coefficients of sand particles and glass beads resulting from the 3D dynamic experiments are plotted.

Additionnaly, Campbell et al. were led to evaluate the contribution of THz technologies to the ability to detect and identify threatening agents. Higher frequency spectra (1.5-21 THz) of small sized chemical and biological warfare agent were acquired with a Fourier transform infrared spectrometer. The resuspension was carried out in a 15 cm long chamber with magnetic stirring [91]. However, their published results focused on the 10-20 THz range, specifically for silica particles. The precise sizes of these particles were not fully specified in the paper.

One significant limitation of these THz studies is the use of pellet or compact powder samples. These materials do not accurately represent atmospheric aerosols, as the size, shape, and structure of the particles are altered during pellet formation. Specifically, the application of pressure during pelletization can induce structural changes that shift the frequency and alter the shape of absorption peaks or bands. Additionally, the morphology of particles in their suspended state, especially in the case of atmospheric aerosols, plays a crucial role in their optical properties. In contrast, when particles are pressed into pellets, their natural shapes and interactions with surrounding gases are lost, which can lead to non-representative results. Therefore, while pellet measurements can provide some insights into material properties, they are not directly applicable to the study of atmospheric aerosols, and care must be taken when interpreting their THz spectra. Further efforts are needed to resuspend particles under controlled conditions to obtain more accurate optical parameters that truly reflect atmospheric behavior.

## 1.6 This study : developing a novel setup for analyzing THz optical properties of atmospheric particles in suspension

As part of this thesis, a novel resuspension bench for atmospheric particles will be established within the IEMN laboratory, marking the first time their optical responses will be obtained in the Terahertz (THz) domain. This setup is being

developed specifically for this research, as no such facility existed prior to this thesis.

This study aims to address several critical questions: How do the optical properties of atmospheric particles differ when they are in pelletized versus resuspended states? Are the optical signals obtained from compacted pellets truly representative of the particles' behavior in suspension? How do structural changes induced by pelletization, such as particle compression, influence their THz optical responses? Furthermore, can the interactions between THz radiation and these particles be better characterized by Rayleigh or Mie scattering theory?

To explore these questions, the optical study will commence with preliminary experiments on powders formed into pellets, followed by the resuspension of these particles in the newly constructed aerosol bench to enable a more realistic comparison. The optical responses from both states will be processed to derive their complex refractive indices in the THz frequency range, utilizing effective medium approximation theories.

In addition, the particles will be characterized at the single-particle scale using Scanning Electron Microscopy (SEM) combined with energy-dispersive X-ray (EDX) analysis at the LPCA laboratory, allowing for a thorough assessment of their morphologies and chemical compositions. Finally, Finite Difference Time Domain (FDTD) simulations will be performed to model the interaction of a THz beam with individual particles. The absorption and scattering cross-sections obtained from these simulations will be compared with results from a custom developed Mie code, providing insights into the adequacy of theoretical models in describing the observed optical behavior.

# Chapter 2

# Realization and characterization of the aerosol measurement bench and THz signal processing

## 2.1 Introduction

This chapter is essential for understanding the comprehensive efforts involved in developing and characterizing an aerosol measurement bench within the THz domain. The first section introduces the THz Time Domain Spectroscopy (THz-TDS) system and the detailed signal processing workflow used to extract optical parameters from the measured data, including algorithms as Correct@TDS and Fit@TDS. It covers uncertainty quantification, error functions, and the use of the Lorentz oscillator model, establishing the foundation for reliable analysis of aerosol interactions.

The second part delves into the specifics of aerosol interaction with the THz beam, including the setup of the aerosol system, flow characterization, and the critical task of aligning the THz beam over a 150 cm distance. The section also includes the optical and mechanical characterization of the cell windows, critical for ensuring minimal interference during measurements, and the analysis of the particle size distribution using advanced techniques.

The final part addresses the morphological and chemical characterization of aerosol samples. Techniques such as Scanning Electron Microscopy (SEM) coupled with Energy Dispersive X-ray (EDX) spectroscopy and X-ray diffraction (XRD) are explored in detail. These methods provide a thorough understanding of the structural and chemical composition of the aerosols, ensuring a well-rounded characterization that integrates both optical properties from the THz measurements and detailed morphological and chemical analyses. This holistic approach is critical to achieving accurate and comprehensive results in the study of aerosols in the THz range.

## 2.2 THz Time Domain spectroscopy and signal processing

### 2.2.1 THz Time Domain Spectroscopy

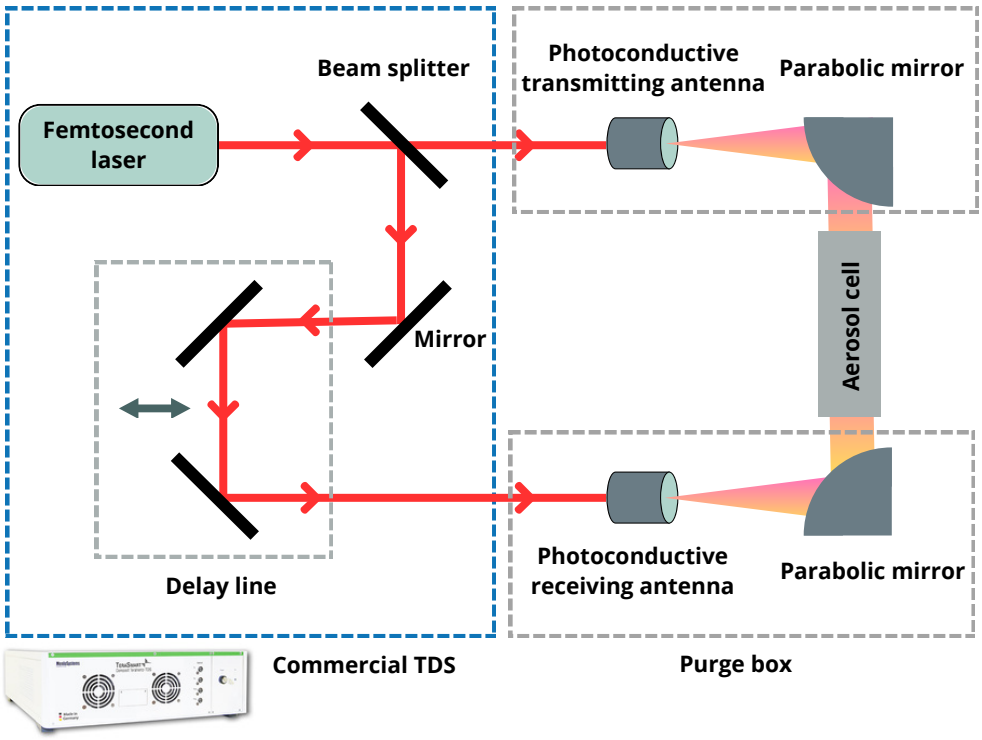


Figure 2.1: Schematic of the Terahertz Time Domain Spectroscopy (THz-TDS) setup.

The principle of TeraHertz Time Domain Spectroscopy (THz-TDS) is illustrated in Figure 2.1, which provides a schematic overview of the setup used for this study [92]. While the beam generation and detection components are commercially sourced, I conducted the characterization tests for the antennas. Additionally, I developed the aerosol generation setup, performed the optical alignment of the system, and selected suitable materials for the experiments. These aspects will be discussed in detail in the following sections of this chapter.

The femtosecond laser beam in this system is generated by a commercial TeraSmart unit from Menlo Systems. Within this compact device, a fiber laser produces 90 fs pulses at a wavelength of 1.5 µm, which are split into two beams: the pump and the probe. The femtosecond laser pulses are generated through a mode-locking technique, which produces short, high-power pulses. Conventional laser sources are unsuitable for THz generation due to the lack of appropriate semiconductors for direct emission in the terahertz range [93].

The pump beam is directed along a delay line that provides a scanning range of up to 850 ps. This delay is managed by a movable retroreflector plate, which adjusts the optical path length. This setup determines the exact moment the THz detector captures the signal in relation to the generated THz pulse. By altering

the timing of the pump beam's arrival at the detector, the delay line facilitates accurate sampling of the THz electric field in the time domain [94].

The THz pulse is generated by focusing the pump beam onto a GaAs photoconductive antenna. Time-domain THz sources typically rely on either photoconductive antennas or optical rectification in nonlinear media to generate extremely short terahertz pulses, though these often have relatively low pulse energy [95]. Photoconductive antennas convert laser energy into THz radiation. These antennas consist of a layer of low-temperature-grown GaAs (GaAs L-T) with metal contacts on semi-insulating GaAs. The short carrier relaxation time in the GaAs L-T film, achieved through epitaxial growth, creates defects that act as recombination and trapping centers. The excess arsenic clusters in the material induce rapid nonradiative recombination within sub-picosecond time intervals.

The probe beam, derived from the same femtosecond laser source, is precisely timed to coincide with the THz pulse at the detector. By adjusting the delay line associated with the pump beam, the moment when the probe pulse interacts with the THz electric field can be controlled, enabling accurate measurements of the electric field's strength at various time intervals.

The resulting THz beam is collimated to a diameter of 38 mm as it traverses the aerosol measurement cell, which measures approximately 95 cm in length and equipped with polypropylene windows. Parabolic mirrors, purchased from Thorlabs, are used to ensure optimal collimation of the THz beam. After passing through the cell, the THz beam is focused on the detector.

The emitted THz pulse consists of a single-cycle oscillation of the electric field. Time-domain measurements are achieved by sampling the THz signal through convolution of the known femtosecond probe pulse with the longer THz pulse. This ensures that a measurable signal is detected only when both pulses arrive at the detector simultaneously, allowing for precise temporal resolution of the THz waveform. The signal at a specific time $t_1$ can be expressed as:

$$S(t_1) \propto I_{laser} \circledast E_{THz}(t_1) \tag{2.1}$$

with :

- $I_{laser}$, the intensity profile of the femtosecond laser pulse.
- $E_{THz}(t_1)$, the electric field of the THz pulse at time $t_1$.

A computer system controls the delay lines and records data from the amplifier to enhance the signal-to-noise ratio. A Fourier transform is then performed on the time-domain data to obtain the frequency spectrum [96, 97].

To mitigate the strong absorption of water vapor in the THz range, which can distort the optical response of the samples, the THz beam path is enclosed within a purge box. This box is flushed with dry air or nitrogen. Since nitrogen molecules lack an electric dipole moment, they do not interact with THz radiation, ensuring a clear signal.

Figure 2.2 presents a representative time-trace of the THz signal along with its Fourier transform, obtained using nitrogen gas alone, with 1000 accumulations over a time window of 60 ps. Subfigure (a) presents the time-domain signal, showcasing the main impulse generated by the THz pulse. This trace reflects the oscillation of the electric field over time, capturing the rapid fluctuations that characterize the THz radiation. Subfigure (b) displays the Fourier transform of the time-domain signal, which represents the frequency spectrum of the THz pulse. Together, these figures underscore the effectiveness of THz Time Domain Spectroscopy in capturing both temporal and spectral characteristics of THz radiation. Signals in the 3.5 to 5 THz range will be discussed and analyzed further in section 2.1.4.3.

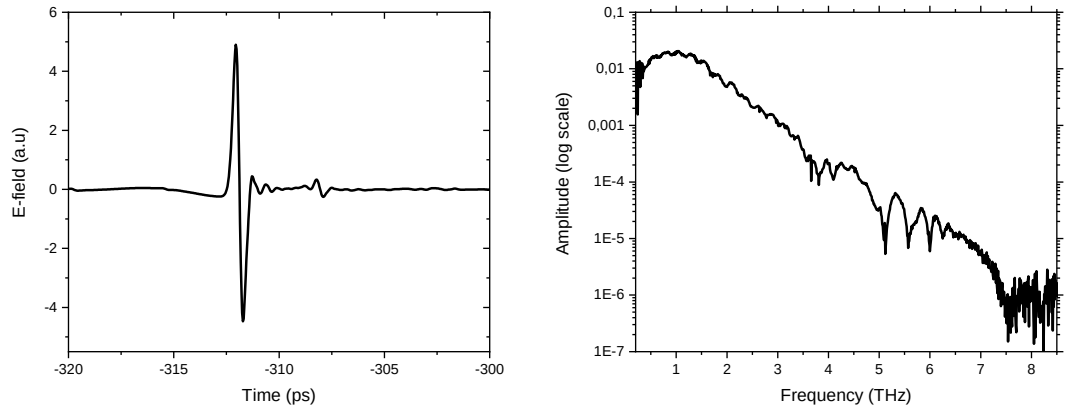


(a) (b)

Figure 2.2: A typical time-trace focused at the main impulsion (a) and its Fourier transform (b) showing the transmission. Nitrogen gas, with 1000 accumulations and 60 ps time-trace.

### 2.2.2 Correct@TDS

The time signal estimator commonly used for measuring samples with a time-domain THz spectrometer is based on the average of the temporal traces accumulated over a specified number of iterations, denoted by $N_{acc}$. Within our research group, we have developed an open-source Python-based algorithm to get as much information on the signal as possible and minimize noise in this estimator. The software, Correct@TDS, provides a refined signal estimator by averaging the temporal traces and applying corrections tailored to specific noise sources using a general optimization approach.

The first set of corrections addresses temporal shifts caused by temperature variations in the optical fibers, which induce thermal expansion and affect the timing of the signal. Additionally, the software compensates for fluctuations in laser pulse amplitude and corrects for variations in the speed of the delay line. By accounting for these factors, Correct@TDS improves the reliability of the signal

estimator, allowing users to extract both the uncertainties in the time-domain signal and the Fourier transform of this estimator.

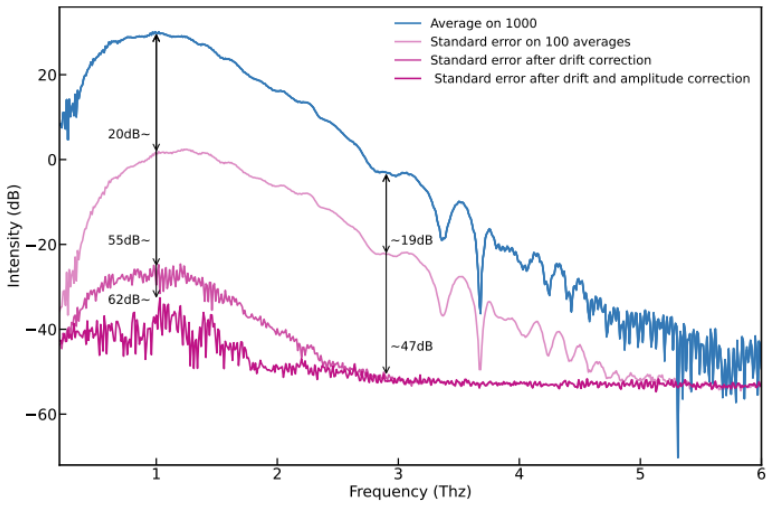


Figure 2.3: Mean and standard error in frequency domain after drift and amplitude correction, from [98]

Given that the frequency and temporal noise are modeled as following a white Gaussian distribution, the standard deviation serves as an indicator of the noise present in both the temporal signal and its Fourier transform. However, even after applying corrections, some residual noise may remain, as illustrated in Figure 2.3. Here, it is evident that the signal correction leads to a significant improvement in the signal-to-noise ratio (SNR), achieving an enhancement of over 30 dB at 1 THz with 1000 accumulated traces after drift correction. Overall, using this software significantly reduces the signal-to-noise ratio (SNR), resulting in an enhanced dynamic range for THz spectroscopic measurements, ensuring more reliable data analysis. However, this is only one aspect of the error; additional systematic errors remain and will require further investigation.

This residual noise exhibits correlations, distinguishing it from purely white noise. To effectively address this issue, we compute the covariance matrix, which facilitates the extraction of accurate material parameters by normalizing the error function during the fitting process implemented in the Fit@TDS software. This comprehensive approach not only refines the signal quality but also enhances the reliability of the material characterization outcomes.

#### 2.2.2.1 Covariance matrix

The covariance matrix quantifies the extent to which two variables vary together and is represented as a square symmetric matrix, defined mathematically by the

following equation:

$$Cov(\tilde{E}(t)) = \frac{1}{n-1}\sum_{t=1}^{n}(\tilde{E}_t - \overline{\tilde{E}_{mean}})(\tilde{E}_t - \overline{\tilde{E}_{mean}})^T \tag{2.2}$$

With $n$ representing the total number of time samples used in computing the covariance matrix.

The matrix takes the following form :

$$Cov((\tilde{E}(t)) = \begin{bmatrix} \sigma^2_{E(t_1)} & \sigma_{E(t_1)E(t_2)} & \cdots & \sigma_{E(t_1)E(t_n)} \\ \sigma_{E(t_2)E(t_1)} & \sigma^2_{E(t_2)} & \cdots & \sigma_{E(t_2)E(t_n)} \\ \vdots & \vdots & \ddots & \vdots \\ \sigma_{E(t_n)E(t_1)} & \sigma_{E(t_n)E(t_2)} & \cdots & \sigma^2_{E(t_n)} \end{bmatrix}$$

In this matrix, the diagonal elements represent the variances ($\sigma^2$), while the off-diagonal elements indicate the covariances ($\sigma$). The matrices are estimated based on repeated noise measurements from both the reference and the sample data. This covariance matrix plays a crucial role in analyzing the reliability of the data and in improving the accuracy of material parameter extraction during the fitting process.

#### 2.2.2.2 Uncertainties on the spectra in frequency domain

The estimation of uncertainties in the frequency domain is critical for understanding the reliability of the spectral data and ensuring accurate material characterization. The standard deviation on the signal at each frequency $\sigma(E(\omega))$ can be expressed as :

$$\sigma(\tilde{E}(\omega)) = \sqrt{\frac{1}{N_f}\sum_{j=1}^{N_f}\left(\tilde{E}(\omega_j) - \tilde{E}_{mean}(\omega_j)\right)^2} \tag{2.3}$$

With :

- $E(\omega_j)$ Fourier transform of the measured and corrected time domain signal at a given frequency $\omega_j$.
- $E_{mean}(\omega_j)$ Fourier transform of the mean measured and corrected time domain signal at a given frequency $\omega_j$.
- $N_f$ the number of frequencies.

This standard error quantifies the precision of the signal estimator and is computed within the Correct@TDS framework. The standard deviations for both the sample and reference signals in the frequency domain, obtained as outputs from Correct@TDS, will subsequently be used to calculate the standard deviation of the transmission in the Fit@TDS software. This process enhances the reliability

of the measurements and aids in extracting accurate material properties. When combining various measurements and calculations to extract material properties, uncertainties can propagate through these computations. The propagation of uncertainties should be systematically analyzed to ensure the final material parameter estimations reflect the underlying uncertainties accurately.

### 2.2.3 Fit@TDS algorithm for optical parameters extraction

When I joined the team, Fit@TDS was already an established open-source tool software designed for direct time-domain fitting. It provided precise measurements of sample thickness and optical properties, such as the complex refractive index (CRI), by integrating various permittivity models to ensure reliable retrieval of material parameters. This process relied on two main inputs: the experimental data, which includes both the sample and reference signals, and a selected permittivity model, defined by parameters that describe how the sample transforms the reference pulse into the modeled pulse [99].

Fit@TDS, however, is an evolving algorithm, undergoing continuous development to refine its accuracy and extend its capabilities. During my work, I contributed to its advancement, particularly in signal analysis, focusing on the implementation and interpretation of error bars to improve the reliability of retrieved values. Through these improvements, I was able to make Fit@TDS a more effective and precise tool, advancing its application in the reliable analysis of THz data.

#### 2.2.3.1 Transfer function

An usual method for complex refractive index determination is to fit a theoretically calculated transfer function. The transfer function describes the time-invariant relation between the input and the output signals. The experimental transfer function can be easily calculated by doing the ratio of the Fourier transform of the two traces.

$$TF(\omega, m) = \frac{\tilde{E}_{sample}(\omega)}{\tilde{E}_{reference}(\omega)} \tag{2.4}$$

With $\tilde{E}_{sample}$ and $\tilde{E}_{reference}$ the measured signals with the sample and without the sample.

The transfer function is also known as transmission coefficient. The transmittance is the ratio between the intensity of the transmitted radiation and the incident intensity. As the intensity of an electromagnetic wave is proportional to the square of the wave's electric field amplitude, the transmission is proportional to the transfer function :

$$\frac{I_{sample}}{I_{reference}} \propto \left( \frac{\tilde{E}_{sample}}{\tilde{E}_{reference}} \right)^2 \tag{2.5}$$

$I_{sample}$ and $I_{reference}$ being the intensity of $\tilde{E}_{sample}$ and $\tilde{E}_{reference}$ amplitudes.

All the transfer functions depend on the complex refractive index. To efficiently retrieve the real and imaginary parts of the complex refractive indices, the so-called inverse problem has to be resolved : knowing the amplitude of the complex transmitted wave and of the incident wave, one can find the complex refractive index of the sample by solving the following transmission $T(\omega)$ equation [1] :

$$T(\omega) = FP(\omega) \times exp\left(-i(\tilde{n}_{sample} - \tilde{n}_{air})\frac{\omega d}{c}\right) \times F(\omega) \tag{2.6}$$

With :

- $\omega$, the angular frequency (rad.s$^{-1}$).
- $FP(\omega)$ the Fabry Pérot multiple reflections term.
- $\tilde{n}_{sample}$ and $\tilde{n}_{air}$, the complex refractive indices of the analyzed sample and the air, respectively.
- $d$ the thickness of the sample in m.
- $c$ the speed of light in m/s.
- $F(\omega)$ the product of the Fresnel coefficients at normal incidence.

The Fabry-Pérot term represents the interference effects caused by light reflecting back and forth between the surfaces of a sample, which can lead to constructive or destructive interference at specific wavelengths or frequencies. The FP term captures how the phase of the light changes as it travels through the material and reflects at the boundaries. Each time light reflects, it incurs a phase shift that depends on the refractive index of the material and the thickness of the sample. For pellets, the FP term directly corresponds to the pellet thickness, while for aerosols, it is primarily a transmission term linked to the path length of the aerosol cell.

Fresnel coefficients describe how electromagnetic waves behave at the interface between two different media, accounting for both reflection and transmission. In THz time-domain spectroscopy, the Fresnel coefficients play a crucial role in defining how the electric field interacts with the boundaries between air and the sample (aerosol or pellet). When solving the inverse problem to retrieve the complex refractive index of the sample, it is critical to account for the Fresnel coefficients. These coefficients affect both the amplitude and phase of the transmitted signal, influencing the effective refractive index derived from the transmission data.

In this context, the retrieved refractive index reflects the effective refractive index of the aerosol sample. By solving the inverse problem, we can derive this effective index, which captures the comprehensive effects of the sample on the

transmitted wave. This effective index encompasses not only the intrinsic optical properties of the aerosol but also the external structural factors that affect light propagation through the medium. The solution to the inverse problem is achieved numerically by formulating an error function that needs to be minimized.

#### 2.2.3.2 Error function

The error function to be minimized compares the theoretical model's expected pulse with the experimental pulse. The expected pulse is calculated using the theoretical model based on the reference pulse. According to Parseval's theorem, the norm of a function is equivalent to the norm of its Fourier transform. This allows the error function to be evaluated directly in the frequency domain, eliminating the need for repeated Fourier transforms during the optimization process.

$$\varepsilon = |(\tilde{TF}_{model} - \tilde{TF}_{sample})|^2 \tag{2.7}$$

With $\tilde{TF}_{model}$ and $\tilde{TF}_{sample}$ the transfer functions of the model and the sample respectively.

By minimizing this error function, a fitting algorithm is applied to each frequency, yielding the real and imaginary components of the complex refractive index (CRI), $n$ and $\kappa$, respectively.

This optimization process enables the retrieval of spectroscopic parameters, such as oscillator strength, resonant frequency, and linewidth, that allow the theoretical model to best match the experimental data. Additionally, this method inherently respects the Kramers-Kronig relations, as it accounts for both the real and imaginary parts of the refractive index due to the time-domain nature of the analysis, ensuring a physically consistent description of the sample's optical properties.

#### 2.2.3.3 Lorentz oscillator model

The Lorentz oscillator model, also known as the Drude-Lorentz model, describes the behavior of an electron bound to an atomic nucleus, modeled as a driven and damped harmonic oscillator. In this framework, the electron is tethered to the nucleus by a spring-like restoring force, and its motion is subject to both an external driving force (such as an electromagnetic field) and a damping force that accounts for energy loss (as illustrated in Figure 2.4). The damping in the model is related to the interaction of the electron with its environment, such as collisions and frictional forces. The resonance mode of the oscillator corresponds to a natural frequency where the energy absorption is maximized, while the width of the resonance peak is inversely proportional to the damping coefficient, reflecting how quickly the oscillator loses energy.

This model allows us to use Newton's second law to describe the electron's motion, which can then be applied to calculate important quantities such as the

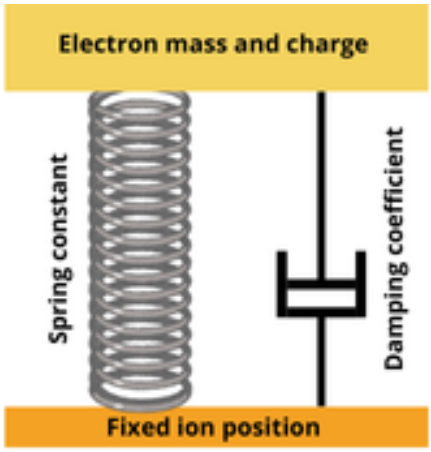


Figure 2.4: Simplified scheme of the Lorentz model. The damping coefficient corresponds to $\gamma$, the spring constant is equal to $m_e\epsilon_0$.

dipole moment, dielectric susceptibility, and the material's optical response. By treating the electron as a harmonic oscillator, we can derive how it interacts with incoming electromagnetic waves, leading to expressions for the material's permittivity and refractive index.

The complex permittivity of a material under the Lorentz model is given by:

$$n = \sqrt{\epsilon_r} = 1 + \frac{\omega_p'^2}{\omega_0^2 - \omega^2 - i\omega\gamma} \tag{2.8}$$

- $\epsilon_r = \frac{\epsilon}{\epsilon_0}$, $\epsilon_0$ being the vacuum permittivity.
- $\omega$ is the angular frequency of the applied electromagnetic field.
- $\omega_0$ is the resonance frequency of the bound electron oscillator.
- $\omega_p'$ is an effective coupling frequency related to the density of bound electrons and their response to the field.
- $\gamma$ is the damping coefficient, representing how quickly the oscillation decays over time.

### 2.2.4 Standard deviation on the transmittance and the retrieved CRI

#### 2.2.4.1 Standard deviation on transmittance

Since the intensity of an electromagnetic wave is proportional to the square of the wave's electric field amplitude, the standard deviation of the transmission is similarly related to the standard deviation of the transfer function. This can be expressed as:

$$\sigma\left(\frac{I_s}{I_{ref}}\right) \propto 2 \times \sqrt{\frac{I_s}{I_{ref}}} \times \sigma\left(\frac{\tilde{E}_s}{\tilde{E}_{ref}}\right) \tag{2.9}$$

$$\sigma\left(\frac{I_s}{I_{ref}}\right) \propto 2 \times \sqrt{\frac{I_s}{I_{ref}}} \times \sigma\left(\tilde{TF}_{sample}\right) \tag{2.10}$$

With :

- $\tilde{TF}_{sample} \propto \sqrt{\frac{I_s}{I_{ref}}}$
- $I_s$ intensity of the transmitted radiation through the sample and $I_{ref}$ reference intensity (without the sample).
- $\sigma(\tilde{TF}_{sample})$ standard deviation of the sample's transfer function.

To propagate uncertainties in this case, the uncertainty propagation law is applied, indicating how uncertainties in variables contribute to the uncertainty of a function. In the context of the transfer function, this leads to the following general equation:

$$\sigma(\tilde{TF}_{sample}) = \sqrt{\left(\frac{\delta\tilde{TF}_{sample}}{\delta\tilde{E}_s} \times \sigma(\tilde{E}_s)\right)^2 + \left(\frac{\delta\tilde{TF}_{sample}}{\delta\tilde{E}_{ref}} \times \sigma(\tilde{E}_{ref})\right)^2} \tag{2.11}$$

Simplified, the equation becomes:

$$\sigma(\tilde{TF}_{sample}) = \sqrt{\left(\frac{\sigma(\tilde{E}_s) \times \tilde{E}_{ref}}{\tilde{E}_{ref}^2}\right)^2 + \left(\frac{\sigma(\tilde{E}_{ref}) \times \tilde{E}_s}{\tilde{E}_{ref}^2}\right)^2} \tag{2.12}$$

$$\sigma(\tilde{TF}_{sample}) = \sqrt{\left(\frac{\sigma(\tilde{E}_s)}{\tilde{E}_{ref}}\right)^2 + \left(\frac{\sigma(\tilde{E}_{ref})}{\tilde{E}_{ref}} \times \tilde{TF}_{sample}\right)^2} \tag{2.13}$$

Given multiple measurements or accumulations, the variance of the averaged transfer function is divided by the square root of the number of accumulations :

$$\sigma(\overline{\tilde{TF}}_{sample}) = \frac{1}{\sqrt{N_{acc}}} \times \sigma(\tilde{TF}_{sample}) \tag{2.14}$$

$$\sigma(\overline{\tilde{TF}}_{sample}) = \frac{\sqrt{\left(\frac{\sigma(\tilde{E}_s)}{\tilde{E}_{ref}}\right)^2 + \left(\frac{\sigma(\tilde{E}_{ref})}{\tilde{E}_{ref}} \times \tilde{TF}_{sample}\right)^2}}{\sqrt{N_{acc}}} \tag{2.15}$$

Therefore, the standard deviation of the transmittance becomes proportional to the variance of the transfer function:

$$\sigma\left(\frac{I_s}{I_{ref}}\right) \propto 2 \times \sqrt{\frac{I_s}{I_{ref}}} \times \frac{\sqrt{\left(\frac{\sigma(\tilde{E}_s)}{\tilde{E}_{ref}}\right)^2 + \left(\frac{\sigma(\tilde{E}_{ref})}{\tilde{E}_{ref}} \times \tilde{TF}_{sample}\right)^2}}{\sqrt{N_{acc}}} \tag{2.16}$$

With :

- $\sigma(\tilde{E}_{ref})$ and $\sigma(\tilde{E}_s)$ standard deviations of the reference and sample signals.
- $N_{acc}$ the number of accumulation.

#### 2.2.4.2 Standard deviation on attenuation and absorption coefficients

The attenuation coefficient according to the Beer Lambert law is expressed as :

$$\alpha = \frac{lnT}{l} \tag{2.17}$$

- $T$ being the transmission $\frac{I_s}{I_{ref}}$.
- $l$ the optical path length in m.

The optical path length is a fixed number. The attenuation coefficient therefore depends on a single variable which is the transmission $T$. The standard deviation of the attenuation coefficient $\sigma(\epsilon)$ can consequently formulated as follows :

$$\sigma(\alpha) = |\frac{\delta\frac{lnT}{l}}{\delta T} \times \sigma T| \tag{2.18}$$

$$\sigma(\alpha) = \frac{\sigma T}{T \times l} \tag{2.19}$$

The standard deviation of the attenuation coefficient is equal to the relative standard deviation of the transmission.
The absorption coefficient is defined as :

$$\kappa = \frac{\alpha \times c}{4\pi \times \nu} \tag{2.20}$$

Using the relationship derived for the standard deviation of the attenuation coefficient, we can also find the standard deviation of the absorption coefficient $\sigma(\kappa)$:

$$\sigma(\kappa) = \frac{\partial\kappa}{\partial\alpha} \times \sigma(\alpha) \tag{2.21}$$

This can be expressed as:

$$\sigma(\kappa) = \frac{c \times \sigma(\alpha)}{4\pi\nu} \tag{2.22}$$

Substituting the expression for $\sigma(\alpha)$ gives:

$$\sigma(\kappa) = \frac{c \times \sigma_T}{T \times l \times 4\pi\nu} \tag{2.23}$$

The imaginary part of the complex refractive index is directly related to the absorption coefficient [100].

#### 2.2.4.3 Standard deviation on the modeled CRI

The uncertainty during the fitting is estimated with a second order Taylor derivation, as illustrated in Figure 2.5. Taylor's theorem articulates the approximation of a function differentiable several times in the vicinity of a point by a polynomial whose coefficients depend only on the derivatives of the function at this point.

The use of a second-order Taylor expansion assumes that the error function is reasonably well-behaved near the optimum. If the error function is highly nonlinear or contains discontinuities, the Taylor expansion might not yield reliable results. In such cases, higher-order terms might need to be considered, or alternative methods such as Monte Carlo simulations could be employed to estimate uncertainties.

The second-order Taylor approximation around its optimum is the Hessian, or the second derivatives of the objective function. The Hessian matrix, denoted as H, whose entries are the second derivatives of the objective function. Note that $H$ is symmetric because the mixed partial derivatives are equal.

$$H_{ij} = \frac{\partial^2 f(x)}{\partial x_i \partial x_j} \tag{2.24}$$

In this context, the $x$'s represent the parameters being fitted in the model, specifically the variables that the error function depends on and that are optimized during the fitting process to obtain the complex refractive index (CRI). These include the real and imaginary parts of the CRI at different frequencies. And $f(x)$ is the error function that evaluates the difference between the model and the experimental data.

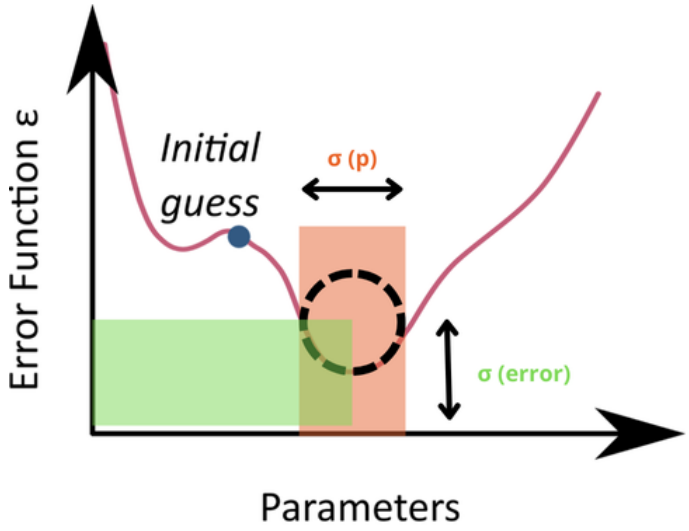


Figure 2.5: From the initial guess of error function to the minimized optimum error function and parameters retrieved with the second derivatives.

At the minimum, the Hessian relates the uncertainties in the parameters to the uncertainties in the objective function. The relation between the error function

at the optimal parameters and the uncertainties in the parameters is given by:

$$Error_{best} + \sigma(p)^2 = Error(p + \sigma_p) \tag{2.25}$$

$$Error(p + \sigma_p) = Error_{best} + \frac{\partial^2 Error}{\partial p^2}\sigma(p)^2 \tag{2.26}$$

$$\sigma(p)^2 = \frac{Error(p + \sigma_p) - Error_{best}}{\frac{\partial^2 Error}{\partial p^2}} \tag{2.27}$$

Rearranging the equation, by setting the increase in the error function to 1 to approximate a 1-sigma (68%) confidence interval for the parameter. :

$$\sigma(p)^2 = \frac{1}{\frac{\partial^2 Error}{\partial p^2}} \tag{2.28}$$

This expression allows the standard deviation of the parameters to be calculated from the second derivative of the error function, providing an estimate of the uncertainty in the retrieved CRI.

## 2.3 Pellets to approximate the behavior of suspended particles

Pelletizing aerosol powder is a traditional approach used to simulate an aerosol suspension. In this method, the sample powder is diluted within a transparent matrix, creating a static medium that imitates the behavior of suspended particles. For example, polyethylene powder has been widely used for sample dilution in the THz range. In the early stages of my thesis, polyethylene was utilized for this purpose but was later replaced by docosane, a choice I will explain further in the following sections.

Despite its utility, pelletizing remains a 2D form of analysis since the particles are static within the matrix. A key limitation of this method is that the THz beam is highly sensitive to the surrounding environment of the particles. As a result, particles embedded in a pellet (surrounded by either air or a powder) will not exhibit the same optical response as those in an aerosol suspension. This sensitivity to the sample's environment can lead to noticeable differences in the recorded THz response.

Another important factor to consider is the particle size distribution in the pellet. The size of the particles in a pellet tends to be much more dispersed than in an aerosol suspension. In a pellet, particle sizes can range from sub-micron to several tens of microns. This is a significant contrast to the resuspension setup used in our experiments, where particles are typically on the order of a few hundred nanometers to a few microns. This size discrepancy can result in frequency shifts in the THz spectrum as well as differences in the observed resonance modes, particularly the vibrational modes specific to THz frequencies. These shifts and variations will be examined in detail in the calcite case study and Chapter 4.

It is also essential to note that the compression pressure (tonnage) applied during the fabrication of the pellets can affect the vibrational modes observed in the THz range. This may lead to differences in the shape of the absorption bands and even slight shifts in their frequencies. However, despite these potential variations, the primary advantage of using pellets is that they offer a straightforward and practical method to ensure that observable bands are present before conducting more complex studies on the material in aerosol form.

Pellet analysis serves as an initial step to verify the material's spectral response, providing a simpler, more manageable procedure compared to analyzing the material in a dynamic aerosol state.

### 2.3.1 Methodology for pellet making

The process begins with weighing the powdered docosane and sample using a precision balance (Sartorius), which has an uncertainty of 0.01 mg. The weight of each component is calculated based on the desired sample concentration in the final pellet mixture. The total mass of the mixture can be adjusted depending on the target pellet thickness, which helps to control the appearance of the Fabry-Perot (FP) reflections in the time-domain trace. By adjusting the thickness, it is possible to push the FP reflection further away from the main pulse, allowing for cleaner time-domain data before the onset of FP oscillations in the frequency domain. However, the FP reflection is typically preserved in the time-domain traces as it provides valuable information about the pellet thickness during analysis with Fit@TDS. Additionally, the total pellet mass generally varied between 100 and 200 mg, with the thickness of the pellets ranging from 0.5 mm to 2 mm, depending on the density and volume of the sample material.

Once the weights are determined, the docosane and sample mixture is placed in an agate mortar. The mixture is then finely ground and homogenized to ensure even distribution of the sample within the docosane. Some mass loss may occur during this step, which depends on the specific properties of the powders being used. After homogenization, the mixture is transferred into a 13 mm metal press die set (Specac). To prevent the docosane from sticking to the die set, tracing paper is placed between the mixture and the metal faces. It's important to note that the sample-to-docosane ratio remains consistent throughout this transfer process due to the thorough homogenization of the mixture.

Next, the die set is placed in a hydraulic press, and pressure is applied to form a smooth, even pellet. The pressure ensures that the pellet has a uniform surface, which is crucial for accurate THz measurements.

The prepared pellets are then mounted in a sample holder featuring 16 circular openings, each with a diameter of 10 mm (as shown in Figure 2.6). This holder allows for the simultaneous measurement of up to 16 pellets in a single experiment.

The experimental setup for pellet measurements follows the same principles as aerosol measurements. The distance between the THz antennas is approximately 40 cm, and 50 mm lenses are placed after the parabolic mirrors to focus the beam onto the pellets. The beam size at the sample position is around 0.4 mm.

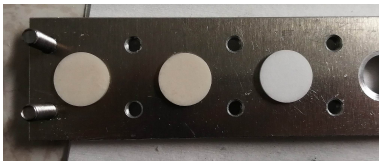

Figure 2.6: Three pellets placed on the sample holder, the two pellets at the left are feldspars diluted into docosane and the one at the right is pure docosane.

This method provides a straightforward and effective way to prepare samples for THz analysis, allowing preliminary tests on pellets before conducting more complex studies on aerosolized materials.

### 2.3.2 Polyethylene and docosane for dilution

The polyethylene (PE) powder used for pellet preparation is Ultra-high molecular weight polyethylene (UHMWPE), with an average molecular weight ranging from 3,000,000 to 6,000,000 g/mol (Sigma Aldrich 429015-250G). Docosane, also purchased from Sigma Aldrich (134457-100G, 99% purity), was selected as a suitable replacement material in the course of my research.

Initially, polyethylene was the preferred transparent powder in our laboratory for THz applications. However, handling UHMWPE presented challenges due to its tendency to accumulate electrostatic charge. Additionally, early in my thesis work, the performance of our THz setup was significantly improved by replacing one of the pairs of lenses with parabolic mirrors, which provided better beam collimation, and by upgrading to more powerful antennas. This allowed the spectra to extend to higher frequencies, revealing a critical limitation: polyethylene begins to absorb strongly beyond 3 THz. Specifically, high-density polyethylene (HDPE), a related form of PE, exhibits a pronounced absorption peak at 6.2 THz, which negatively impacts the spectrum starting from 3 THz.

Due to these issues, polyethylene was replaced by docosane, a saturated hydrocarbon consisting of a 22-carbon chain. Docosane has a melting point of around 44°C, making it easy to handle without concern for melting during sample preparation. Furthermore, due to its waxy consistency, docosane forms durable, non-brittle pellets when subjected to the pressure of a hydraulic press, in contrast to polyethylene. This property is particularly advantageous when analyzing delicate crystalline or biological powders, which can undergo structural changes under high pressure.

The comparison between the two materials is illustrated in Figure 2.7. It shows the transmission spectra of a pure polyethylene pellet weighing 100 mg and pressed

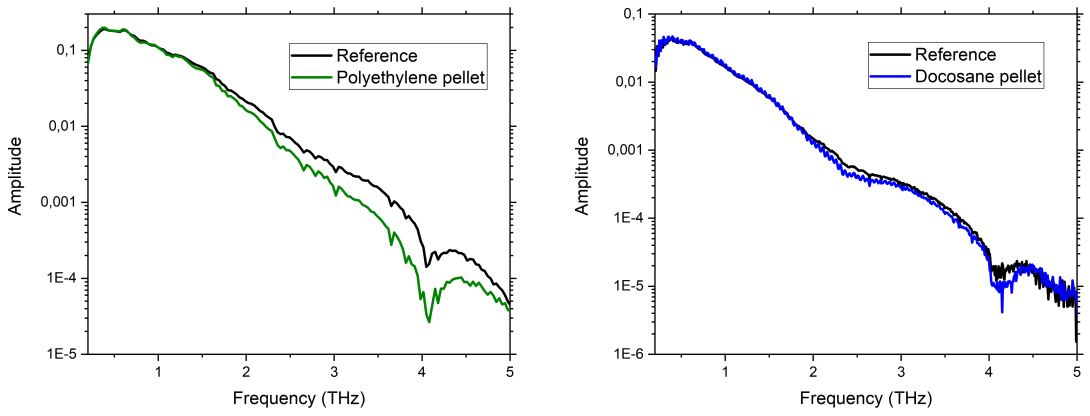


(a) (b)

Figure 2.7: Comparison of the transmission of a pure PE pellet of 100 mg and pressed at 8 tons (a) with a pure docosane pellet of 150 mg ans pressed at 5 tons (b).

at 8 tons (Figure 2.7a) compared to a pure docosane pellet weighing 150 mg and pressed at 5 tons (Figure 2.7b). The higher pressing force used for the polyethylene is necessary to prevent the pellet from breaking, whereas the waxy consistency of docosane allows for lower pressure during pressing, resulting in better outcomes.

Despite the larger mass of the docosane pellet, it exhibits superior transparency at higher frequencies compared to polyethylene. The intense absorbance peak of HDPE at 6.2 THz likely influences the spectrum starting from 3 THz, which is why docosane—free from such interference—became the preferred medium for THz measurements.

## 2.4 Aerosol interactions with the THz beam

### 2.4.1 Aerosol set-up for THz analysis

The aerosol setup consists of three main components: In the first section, particles are resuspended, creating an aerosol. The second section features a cell measuring 95 cm in length and 5 cm in diameter, which is used to probe the optical properties of the aerosol in the THz range. Finally, the third component allows for the measurement of both the concentration and the particle size distribution (see Figure 2.8).

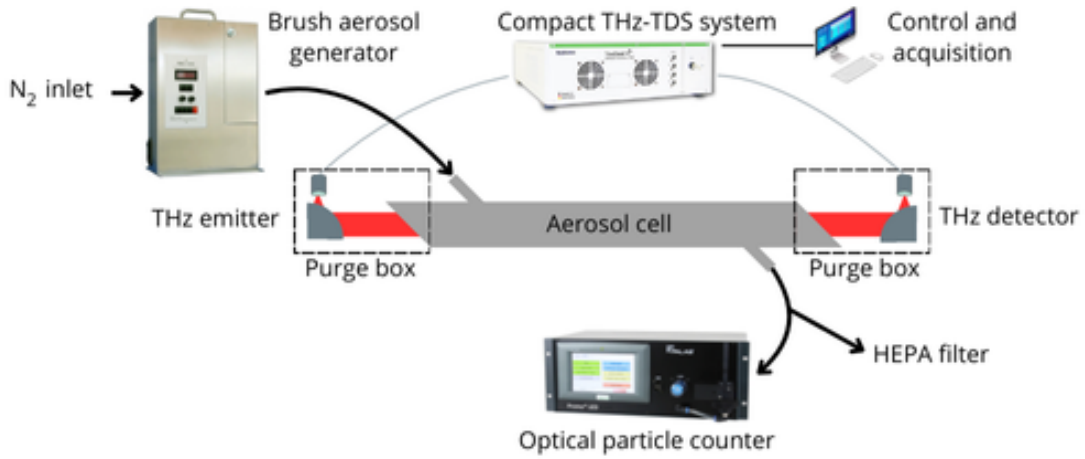


Figure 2.8: Simplified scheme of the aerosol resuspension and THz-TDS optical analysis set-up.

#### 2.4.1.1 Aerosol Generation

Initially, aerosol generation was performed using the custom-built PC2A resuspension method, adapted to meet the implementation constraints of our setup (Figure 2.9). In this method, particles were placed in a reactor under magnetic stirring to facilitate resuspension. The resuspended particles were then directed towards a buffer volume, designed to remove larger particles by impaction. This buffer volume featured both an inlet and outlet for particle flow, as well as an outlet connected to a High-Efficiency Particulate Air (HEPA) filter to prevent overpressure or vacuum buildup in the system [101].

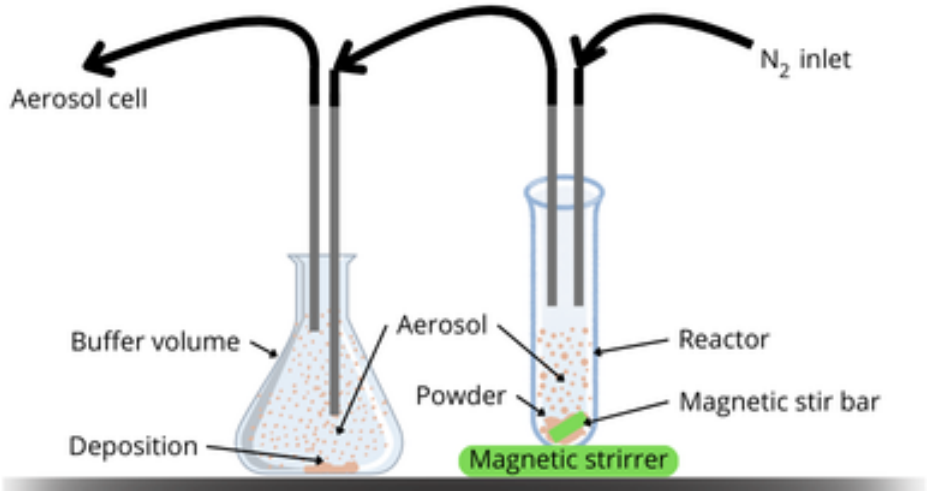


Figure 2.9: Initial aerosol generation method. Particles were resuspended under magnetic stirring in the reactor and then directed to the buffer volume where bigger particles were impacted.

The nitrogen flow was precisely controlled by a mass flow controller (MFC) positioned upstream of the reactor. With the PROMOLED pump operating at 4.8 L/min, the MFC was set to 5 L/min, allowing the excess nitrogen to exit through

the HEPA filter. This ensured that the flow rate exceeded the capacity of the particle counter pump, an important factor since THz frequencies are highly sensitive to water vapor. By avoiding the introduction of ambient air into the system, we minimized the potential for water vapor contamination. After passing through the buffer volume, the particles were directed to the measurement cell. To minimize electrostatic interactions, silicone tubes were used to transfer particles between containers.

While this resuspension method served our initial needs, the concentration of the particles inside the aerosol cell was not enough to register the optical response. Its use may still be considered in the future as the setup becomes more sensitive and refined.

The homemade PC2A resuspension setup was ultimately replaced by the Brush Aerosol Generator for Solids (RBG - Palas), which significantly increased the number of particles introduced into the cell—up to ten times more than the previous method—while enabling the recording of the particles' optical response in the THz range. The operating principle of the RBG is illustrated in Figure 2.10.

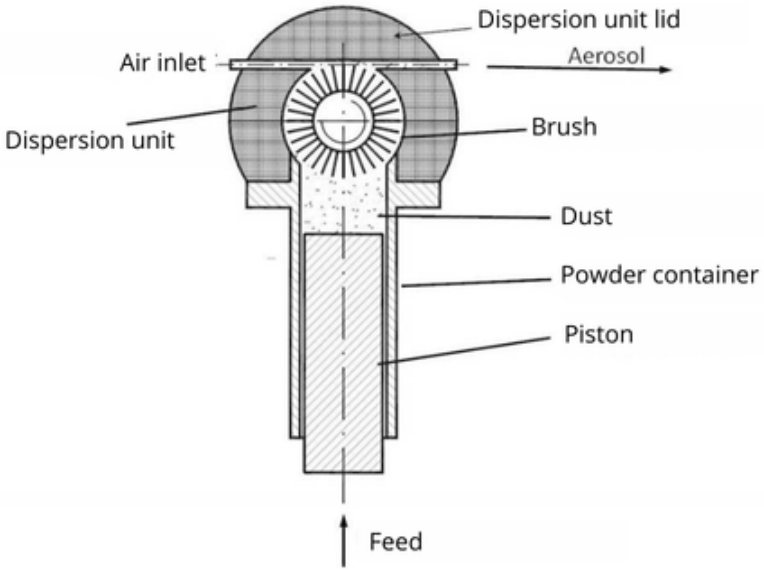


Figure 2.10: Explanatory diagram of the RBG and its different parts, found on the seller CONTREC's website, translated from German into English.

However, this new device introduces different constraints compared to the earlier setup. The powder container has a filling height of 70 mm, and the powder to be dispersed is gradually distributed within a solid cylindrical chamber. Once filled, the powder container is positioned in the RBG's dispersion unit, where it is conveyed against a rotating brush at a precisely controlled feed rate. A high-speed adjustable volumetric flow rate from the densely woven brush extracts particles and resuspends them in dinitrogen gas.

It is crucial to keep the samples dry, especially since some materials, like calcite, can be hygroscopic. Hygroscopic particles tend to absorb moisture from the

surrounding atmosphere, which means that measurements on non-dried samples may reflect ambient conditions. Additionally, Barcelos et al. [102] demonstrated that heating the oven to over 300°C is necessary to eliminate any water included within the sample structure. However, heating certain samples may lead to changes in their crystallographic structure, and potentially affecting their optical response in the THz range, as THz frequencies are sensitive to structural variations. For example, calcite can transition from the calcite I phase to calcite II, III, or even aragonite under increased temperature and pressure [103]. Some of our samples may also have thermal decomposition temperatures around 300°C [104]. Therefore, while the presence of water can interfere with optical measurements, it is crucial to avoid heating mineral samples to such temperatures without properly managing their upstream and downstream phases. Notably, no significant differences in spectra have been observed between dried samples at 100°C during 48 hours and non-dried samples.

Finally, the use of the RBG requires a significantly higher amount of powder compared to the initial system, typically necessitating at least 200 mg. This increased quantity accounts for system stabilization before beginning spectrum acquisition. Additionally, the nitrogen flow rates at various parts of the device were measured using TSI mass flow meters (range: 0.01-20 L/min), and these measurements will be discussed in the following section.

#### 2.4.1.2 Flow characterization

The dinitrogen flow was characterized using TSI flow meters, which have an uncertainty of ±2% (Figure 2.11). These flow meters were strategically placed upstream and downstream of the measurement cell, as well as at the junction with the PROMOLED and the HEPA filter. For the RBG to function properly, a minimum flow rate of 14.3 L/min is required; lower flow rates will not activate the system. During aerosol measurements, the RBG operates at this minimum flow rate, with 14.3 L/min measured at the cell outlet. Of this, 4.8 L/min, corresponding to the PROMOLED pump capacity, is directed to the particle counter, while 9.5 L/min is expelled through the HEPA filter.

As the resuspended particles traverse the silicone and stainless steel tubes, as well as the cell, they experience three primary modes of movement: sedimentation, impaction, and diffusion. However, the predominant modes of movement will be impaction and diffusion, while sedimentation plays a minor role in this context. Gravitational forces and resistance from the dinitrogen ultimately counteract the buoyancy of the particles, causing them to deposit on the walls of the tubes and the cell, particularly for larger particles. Impaction occurs when suspended particles encounter bends in the tubing; more massive particles tend to travel straight rather than following the nitrogen flow, impacting surfaces in their path. This underscores the importance of minimizing sharp bends in the setup [105]. Diffusion, or Brownian motion, describes the random movement of

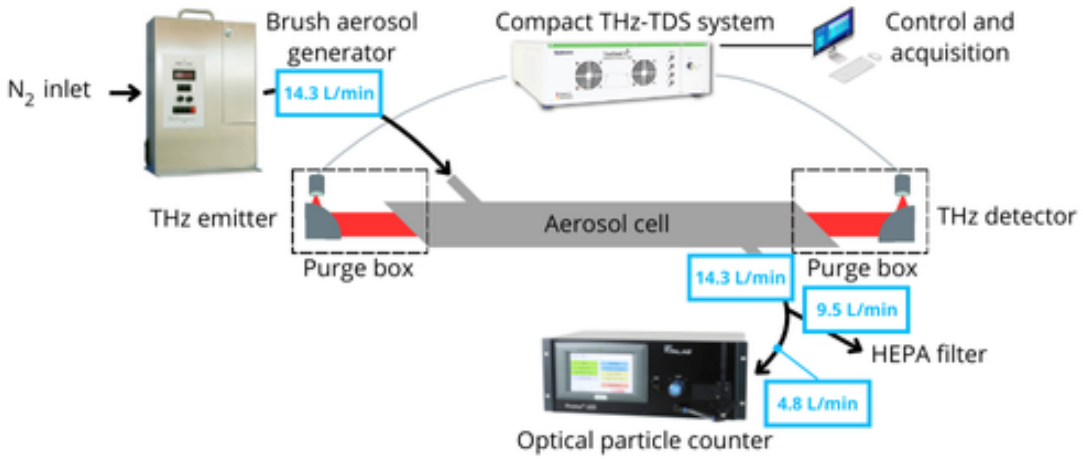


Figure 2.11: Simplified scheme of the aerosol resuspension set-up showing the measured flows upstream and downstream the aerosol cell.

smaller particles, similar to that of gas molecules.

The sedimentation rate of particles can be described by various laws, such as Stokes' law, applicable in laminar flow conditions for spherical particles. Nonetheless, characterizing turbulence in the cell is crucial, which can be assessed using the Reynolds number. At low Reynolds numbers, flow is typically laminar, while higher Reynolds numbers indicate turbulent flow. The relationship between the Mach number (M) and the Knudsen number (Kn) is also significant; the Mach number is a dimensionless quantity representing the ratio of flow velocity to the speed of sound, while the Knudsen number assesses the continuity of the flow regime.

$$Re = \frac{|v^p - v^f|d}{\mu} = \frac{4M}{K_n} \tag{2.29}$$

With :

- $\mu$ the kinematic viscosity in kg/m/s. The value is $1,76 \times 10^{-5}$ for dinitrogen gas.
- $d$ particle diameter in m.
- $v^p$ particle velocity in m/s.
- $v^f$ dinitrogen velocity in m/s.
- $M$ the Mach number, $M = \frac{|v^p - v^f|}{c^f}$
- $K_n$ the Knudsen number, $K_n = \frac{2\lambda}{d}$
- $c^f$ the speed of sound. It is of 343 m/s at 20 $°C$ in the air.
- $\lambda$ the mean free path of gas molecules in m.

The mean free path $\lambda$ of the gas molecules is given by :

$$\lambda = \frac{kT}{\sqrt{2}\pi d_m^2 P} \tag{2.30}$$

With :

- $k$ the Boltzmann constant, $k$ = 1.38x10$^{-23}$ J/K.
- $T$ the temperature in K. In our case, the temperature is 295.5 K.
- $d_m$ the gas molecule collisional diameter in m. For dinitrigen, $d_m$= 380 x10$^{-12}$ m.
- $P$ the pressure in Pa. The measurements were carried out at 1 atm, corresponding to 101325 Pa.

Therefore, the mean path of dinitrogen can be calculated :

$$\lambda = \frac{1.38 \times 10^{-23} \times 295.5}{\sqrt{2}\pi \times 380 \times 10^{-12^2} \times 101325} \tag{2.31}$$

$$\lambda = 6.27 \times 10^{-8} m \tag{2.32}$$

The mean path of dinitrogen is equal to $6.27 \times 10^{-8}$ m.

Next, the Knudsen number is calculated for a particle diameter of 1 µm, which approximately corresponds to the mean diameter of the particles analyzed with the aerosol setup at IEMN:

$$K_n = \frac{2\lambda}{d} = \frac{2 \times 6.27 \times 10^{-8}}{1 \times 10^{-6}} \tag{2.33}$$

$$K_n = 0.1254 \tag{2.34}$$

For particles with a diameter of 1 µm, a Knudsen number of approximately 0.1254 is calculated, which will be lower for larger particles. When the Knudsen number is significantly less than 1, particle flow can be considered continuous, suggesting that the distance traveled by a particle between collisions with dinitrogen molecules is small relative to the particle's size. Consequently, the motion of the particle phase can be expressed in terms of macroscopic fluid properties, such as density and viscosity.

In calculating the Mach number, the velocities of the particles and the flow are assumed to be negligible in difference. The flow rate in the cell is 14.3 L/min, and we can approximate the particle rate to be similar. Therefore, the Mach number is considered very small.

Therefore, we will simplify the Reynolds number to:

$$Re = \frac{\rho v d}{\mu} \tag{2.35}$$

where:

- $\rho$ is the fluid density in kg.m$^{-3}$. For dinitrogen at 1 atm and 20 $^\circ$ C, the fluid density is 1.16 kg.m$^{-3}$.
- $v$ is the flow velocity in m/s.
- $d$ is the particle diameter in m.
- $\mu$ is the dynamic viscosity of the fluid in kg/m/s.

The velocity of the flow is calculated by divding the transversal section of the cell (with a diameter of 5 cm) by the flow rate $r$ of dinitrogen in m³/s :

$$v = \frac{\pi \times R^2}{r} \tag{2.36}$$

$$v = \frac{\pi \times (2.50 \times 10^{-2})^2}{2.38 \times 10^{-4}} \tag{2.37}$$

Therefore :

$$v = 8.25 \quad \text{m/s} \tag{2.38}$$

$$Re = \frac{1.16 \times 8.25 \times 1 \times 10^{-6}}{1.76 \times 10^{-5}} \tag{2.39}$$

$$Re = 0.54 \tag{2.40}$$

The reynolds number is less than 1, the flow is therefore laminary, as expected. During aerosol counting or sizing, laminar flow ensures that particles traverse the detection area without sudden disruptions, allowing for accurate detection and characterization. While laminar flow conditions provide a stable and predictable environment that enhances measurement consistency, they also introduce specific challenges, particularly concerning wall effects and particle deposition. In laminar flow, the flow velocity near the walls of the measurement cell is significantly reduced due to the development of boundary layers. This can lead to a situation where particles close to the walls experience slower velocities and increased deposition rates. Consequently, this can result in a discrepancy between the actual concentration of particles in the bulk flow and the measured concentration, especially for larger particles that are more prone to deposition.

However, understanding the precise dynamics within the cell remains challenging due to the small size of the particles, despite efforts to capture interior footage. Future experiments could benefit from a transparent cell combined with fluorescent particles and high-speed cameras. Additionally, losses within the cell, attributed to the high flow rates associated with the RBG, are primarily due to impaction. This leads to the hypothesis that the optical response we measure may correspond to a greater number of particles than what the PROMOLED counts, potentially distorting analyses during the CRI extraction.

#### 2.4.1.3 Alignment of the THz beam at a distance of 150 cm

Once the aerosol is generated, it is directed into a stainless steel cell with a diameter of 5 cm and a length of 95 cm. At both ends of the cell, dinitrogen purge boxes are installed. Within these boxes, THz transmitting and receiving antennas are positioned, collimating the beam to a diameter of 3.8 cm over a length of 150 cm. These antennas are connected to a compact rack housing the laser, the delay line, and an Ethernet-based remote control engine.

Achieving alignment with parabolic mirrors at a distance of 150 cm can be challenging due to the divergence of the THz beam. The alignment process must be performed incrementally at various distances, characterizing the beam at each step. Initial alignment is conducted without the cell in place. The purge boxes are mounted on a rail system, while an additional rail is installed within the boxes to facilitate precise positioning of the parabolic mirror and antenna, allowing for millimeter-scale adjustments. This parabolic mirror and antenna assembly will be referred to as the "headlight."

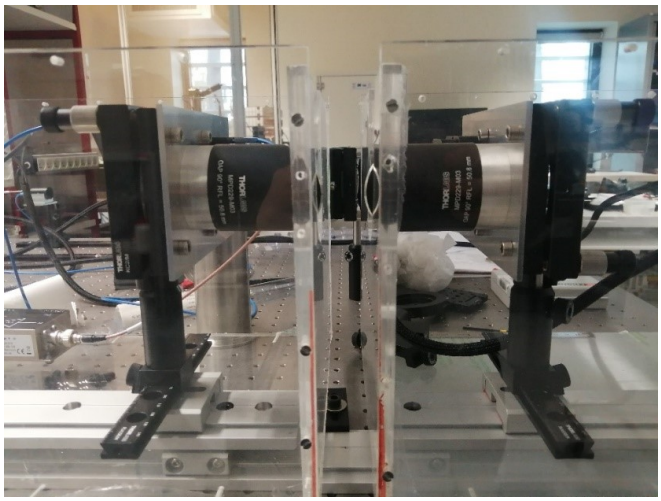

Figure 2.12: The two boxes on the same rail, containing the parabolic mirror, brought together as much as possible in order to make the first adjustments (height, inclination, angle, etc.). The long side of the parabolic mirrors makes a continuous line, there is no difference in angles between the headlights.

The primary goal of this alignment process is not only to achieve long-distance collimation but also to compare our results with the performance metrics provided in the Fraunhofer reports during the purchase of the antennas. The Fraunhofer conditions included the use of two 2-inch parabolic mirrors, a distance of 30 cm between the antennas, and 1000 averages of 65 ps time traces. To closely replicate these conditions in the IEMN laboratory, we selected two 2-inch parabolic mirrors and an optical path of 37 cm between the antennas—the minimum length dictated by the optical fiber constraints. Temporal traces are acquired using 1000 averages within a time window of 65 ps (from -420 ps to -355 ps) to match the spectral resolution reported in the Fraunhofer performance tests. The acquisition

time is determined by the number of averages and the length of the time traces.

**Obtaining a collimated signal** The longest time trace corresponds to an antenna separation of 103 cm, with a time window of -425 to 425 ps. For the 37 cm distance, the time window was set to 65 ps (-420 to -355 ps), while for the 60 cm distance, the time window was adjusted to 340 to 425 ps. The variations in the lengths of the temporal traces can be attributed to limitations imposed by the optical fibers. All time traces consist of 1000 accumulations. The acquisition time depends on the length of the time-traces for the same number of accumulations. Usually it takes less than 15 minutes.

The spectral magnitude remains relatively consistent for measurements taken at both 37 cm and 60 cm distances between the antennas, indicating effective collimation of the beam (see Figure 2.13). However, as the distance increases, the presence of water disrupts the spectrum. This disruption arises from the purging process, as the installation is not fully sealed and ambient air can enter due to the plastic surrounding the setup. At 103 cm, the excess moisture makes it difficult to distinguish the spectral pattern, even after a full day of purging. Despite these challenges, the spectra suggest that the beam is well collimated, highlighting the need for a purge box encompassing the entire setup, which exceeds 150 cm, to achieve accurate measurements and reliable spectra.

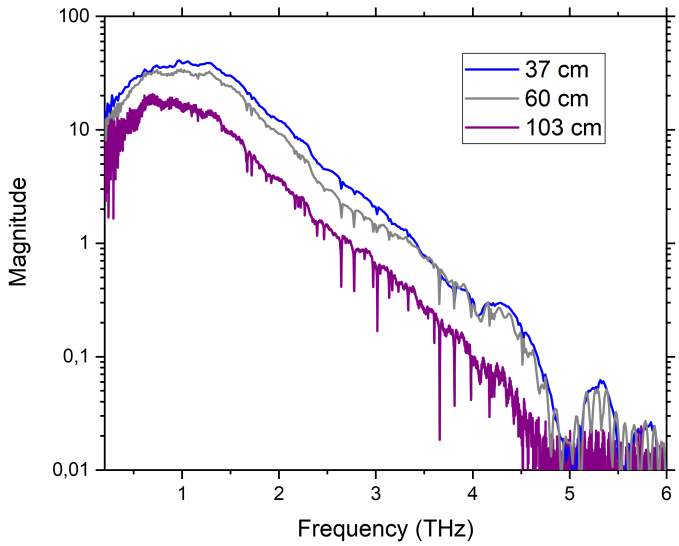


Figure 2.13: Fourier transform magnitudes of the time-traces of 103 cm (purple),60 cm (grey) and 37 cm (blue) distance between the antennas. Whitout the aerosol cell, purged.

**Antennas coatings** Figure 2.14 presents the time traces and their Fourier transforms for both the purged and unpurged optical paths at a distance of 37 cm.

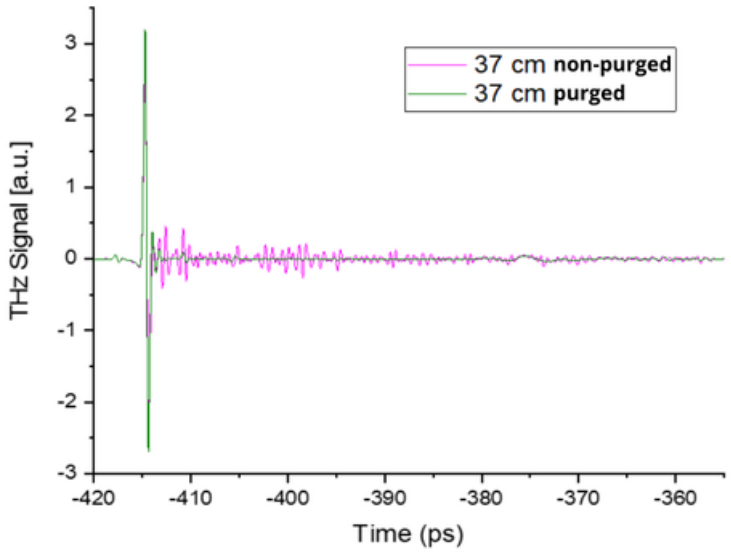


(a)

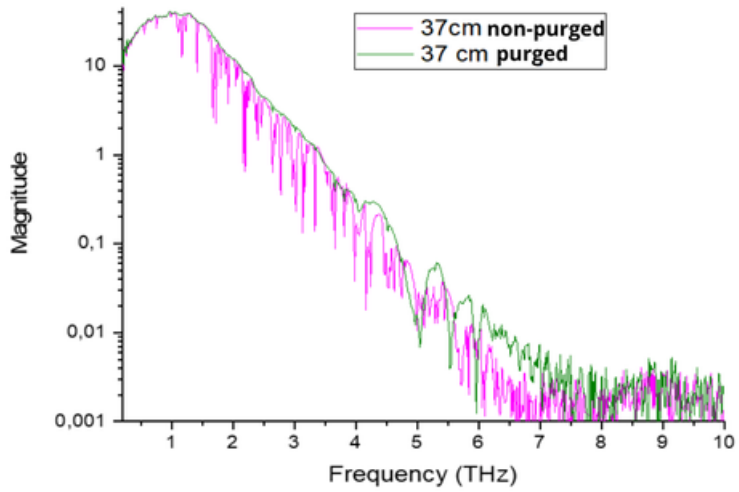


(b)

Figure 2.14: Purged and non-purged time-traces at 37 cm distance between the antennas for a 65 ps time-traces with 1000 averages (a) and the Fourier transforms of the time-traces (b).

A Fabry-Pérot effect (FP), characterized by multiple reflections within a material along the optical path, is observed around 5 THz in the frequency domain. This effect exhibits a spacing of 0.23 THz, corresponding to 4.5 ps in the time domain.

This segment of the time trace is predominantly influenced by water vapor resonances, which accounts for the inability to visualize the oscillations of the FP in the unpurged condition. Notably, these oscillations persist under various experimental conditions—whether the cell is present or absent, whether a window is used, or with varying path distances. Given that the antennas are the only consistent material present, and considering that 4.5 ps corresponds to a very short distance of approximately 0.7 mm, we can hypothesize that a coating within the antennas is interacting with the THz beam. Unfortunately, further investigation into the origin of this FP is limited, as the performance tests conducted by Fraunhofer were carried out in ambient air, and the exact compositions of the commercial antennas are not disclosed.

#### 2.4.1.4 Selection and characterization of window materials for the aerosol cell

At both ends of the aerosol cell, windows are positioned with an angle to optimize THz beam transmission. During the setup of the measurement bench, a thorough characterization of potential window materials was conducted to select the one with the best transmission across the measurement interval of 0.2 to 5 THz, while also ensuring suitable mechanical properties to withstand operational constraints.

Three low-loss polymer candidates were evaluated: polytetrafluoroethylene (PTFE, 2.5 mm thick), polymethylpentene (TPX, 2 mm), and polypropylene (PP, 50 microns). Their complex refractive indices (CRI) were extracted from time-traces obtained via THz time-domain spectroscopy (THz-TDS) [106]. The CRI is essential for this characterization because it provides detailed information about how the material interacts with electromagnetic waves, including both the speed of light within the material (real part) and how much the light is absorbed or scattered (imaginary part). Accurate knowledge of the CRI allows for the optimization of the THz beam transmission and minimizes losses, which is critical for achieving reliable measurements in the THz range.

The data were then fitted to theoretical models using the Fit@TDS software developed by members of the THz Photonic team at IEMN. The fitting process involves the Lorentz oscillator model with four parameters: permittivity, resonance frequency, linewidth, and oscillator strength for each resonance.

Extrapolation was performed for PTFE (beyond 5 THz) and for PP (beyond 7.3 THz), noting that the starting frequencies for extrapolation differ due to the more efficient antennas used in measuring PP films.

The CRI of PTFE from 0.2 to 8 THz is depicted in Figures 2.15 and 2.16. These figures reveal a Lorentzian-shaped resonant absorption peak at 0.91 THz with a linewidth of 0.12 THz, situated above a broad band of higher frequencies. Our

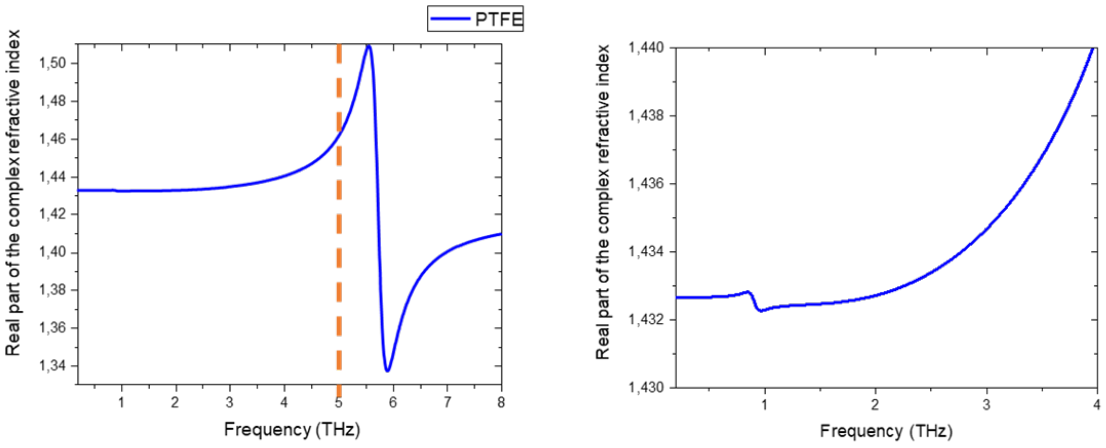


(a) (b)

Figure 2.15: Real part of the CRI of PTFE from 0.2 to 8 THz, extracted by the Fit@TDS algorithm on (a). There is a focus on the peak at 0.91 THz on the figure (b). The dashed line shows the start of the extrapolation.

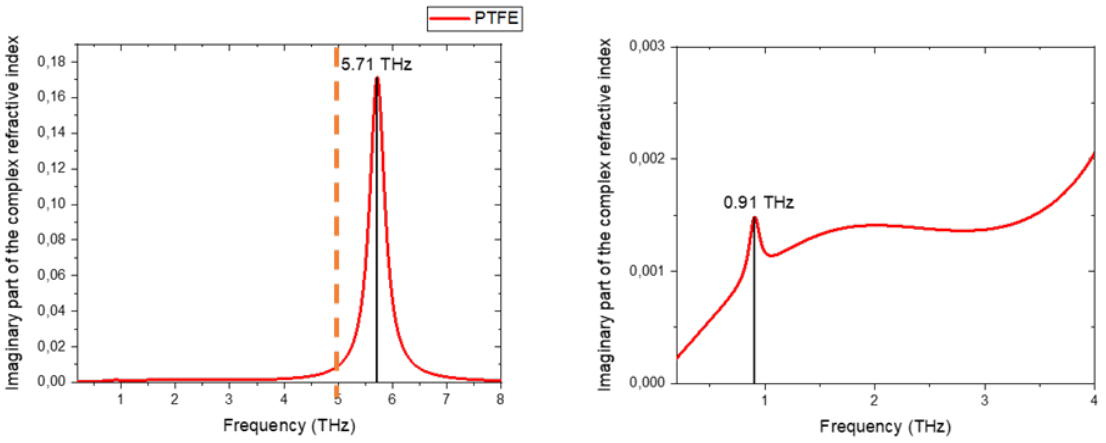


(a) (b)

Figure 2.16: Imaginary part of the CRI of PTFE from 0.2 to 8 THz, extracted by the Fit@TDS algorithm on (a). There is a focus on the peak at 0.91 THz on the figure (b). The dashed line shows the start of the extrapolation.

results indicate a broad absorption band with low oscillator strength at 2.48 THz, characteristic of low-loss polymers, attributed to weak lattice modes. A significant absorption peak at 5.71 THz was also observed, corresponding to the twisting mode of $CF_2$. Previous studies reported only a broad absorption band in this range; our findings extend this knowledge by identifying the weak absorption peak at 0.91 THz, made possible by a superior signal-to-noise ratio [107, 108].

For PP, three Lorentzian-shaped absorption peaks were identified at 2.32, 5.19, and 7.56 THz (Fig. 2.17). The two lower frequency peaks are likely associated with lattice modes, while the peak at 7.56 THz is probably related to CH vibrations.

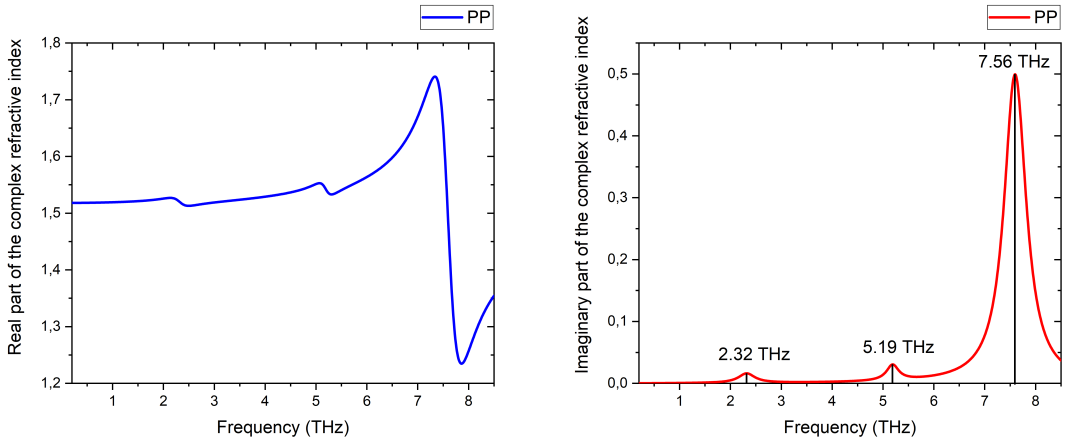


(a) (b)

Figure 2.17: The real (a) and imaginary (b) parts of the CRI of PP film from 0.2 to 8.5 THz. The dashed line shows the start of the extrapolation.

This conclusion aligns with previous reports on resonance frequencies [109]. Although the peak at 7.56 THz exhibits higher intensity compared to the others, the signal-to-noise ratio (S/N) in the literature limits direct comparison of peak intensities.

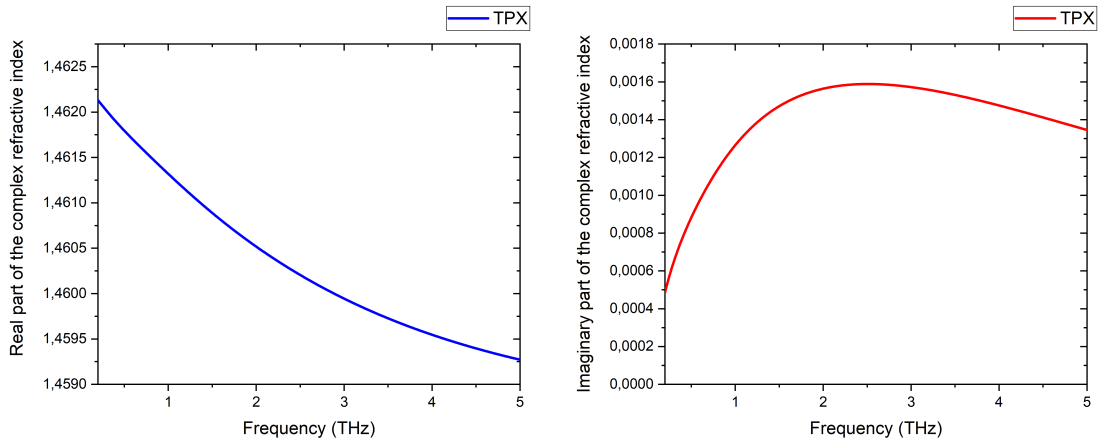


(a) (b)

Figure 2.18: The real (a) and imaginary (b) parts of the CRI of TPX from 0.2 to 5 THz.

TPX displays a broad absorption band with low oscillator strength, attributed to lattice mode vibrations (Fig. 2.18). The variations in the real and imaginary parts of its CRI are on the order of $10^{-3}$ across the measurement frequency range. TPX has therefore a stable refractive index, which is important for maintaining consistent optical performance.

Importantly, TPX does not show any absorption peaks from 0.2 to 5 THz that could interfere with measurements, although further investigations are war-

ranted to explore its behavior beyond 5 THz.

Overall, the optical characterization of PTFE, PP, and TPX aligns well with existing literature, yet our measurements demonstrate improved resolution at lower frequencies and enhanced S/N ratios. Additionally, our results extend beyond 8 THz in some cases, surpassing the typical limit of around 3 THz reported in most studies.

In addition to optical characterization, the materials were also assessed mechanically by calculating the Young's modulus and breaking stress. Young's modulus, or modulus of elasticity, quantifies a material's resistance to changes in length when subjected to tension or compression. A low Young's modulus indicates flexibility, while a high modulus signifies rigidity. Breaking stress measures the maximum internal resistance a material can endure before structural failure or rupture occurs. These mechanical properties are critical in ensuring the reliability and durability of the selected window materials under operational conditions.

| | PTFE | TPX | PP |
|---|---|---|---|
| color (visible) | White | Transparent | Transparent |
| Melting temperature ($°C$) | 327 | 240 | 160 |
| Density ($g.cm^{-3}$) | 22 | 0.83 | 0.9 |
| Thickness | 2.5 mm | 2 mm | 50 µm |
| Young modulus (MPa) | $5.5x10^{-1}$ | $1.6x10^{3}$ | $1.3x10^{3}$ |
| Breaking stress (MPa) | 13.6 | 25 | 5.5 |

Table 2.1: Physical and mechanical properties of PTFE, TPX and PP windows.

Ultimately, the most suitable material for the aerosol cell windows is PP film, as it remains transparent across the 0.2 to 5 THz range. The intense peak at 5.71 THz for PTFE could distort spectra around that frequency. Although TPX also shows transparency up to 5 THz, the cost of the material is a significant consideration, as windows become contaminated during aerosol resuspension and require frequent replacement. Moreover, the mechanical properties of PP film are adequate since the assembly is not under vacuum conditions. However, should the cell be placed under vacuum, PTFE or quartz would be preferable.

#### 2.4.1.5 Size distribution

At the outlet of the aerosol cell, particles are directed towards the optical particle size analyzer (OPS - PROMOLED 2300 - Palas), which records both particle concentration and size distribution. The PROMOLED 2300 offers real-time visualization of aerosol distributions by employing the principle of optical light scattering from individual particles. It operates within a detection range of 0.14 µm to 100

µm, accommodating particle concentrations from 0 to 20,000 particles/cm³. For our measurements, data were collected at 1-second intervals across 64 channels, specifically calibrated for particle sizes ranging from 0.14 µm to 10 µm.

The PROMOLED system features T-aperture technology, which eliminates border zone errors, ensuring precise measurements even at high particle concentrations (fig. 2.19). Promo® LED sensors with integrated signal converters can be positioned close to the sampling point, optimizing space utilization. This allows for the separation of the measuring probe and control unit, making the system ideal for challenging environmental conditions, such as in process analysis.

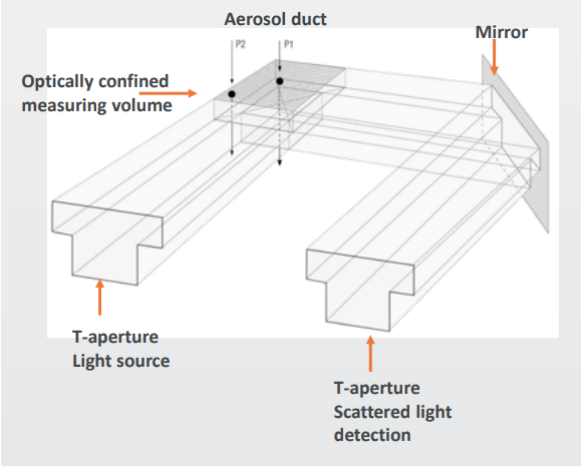


Figure 2.19: T-aperture technology, from Palas Brochure of PROMOLED 2000.

As particles enter the aerosol sensor, they pass through a polychromatic LED light source, illuminating the measurement volume. Each particle generates a scattered light pulse, which is detected at an angle of 90°. The number of scattered light pulses corresponds to the particle count, while the intensity of the scattered light allows for size determination. The signal processing electronics interpret these measurements, assigning particle counts to specific size channels.

To ensure accurate sizing across its entire range, the instrument is calibrated using silica particles (MonoDust 1500) of known sizes, applying Lorenz-Mie theory. The dust consists of silicon dioxide and the particles have a size of 1.28 µm. This calibration enables the sizing of measured particles that fall between the calibration points [110]. It is important to note that coincidence errors can occur when multiple particles are present in the sensing zone simultaneously, which may affect both size and concentration measurements.

The device features a user-friendly touch screen interface and runs on a Windows operating system. Compiled data is processed within the controller and can be saved or transferred via USB for further analysis with the software PDAnalyze.

An inter-comparison campaign was conducted, organized by the National Laboratory of Metrology and Testing (LNE), the Nano-metrology club (CNM), and the National Institute of Research and Security (INRS). During this campaign,

two powders—glass beads and green holi powder — were analyzed using an OPS, APS, and the PROMOLED 2300. The particle counters simultaneously measured the same particles, comparing parameters such as average diameter, standard deviation, and particle concentration. However, due to the confidentiality of the results from this campaign, the data will not be shown.

## 2.5 Morphological and chemical characterization of the samples

In the study of aerosols and their interaction with THz spectroscopy, it is crucial to understand the morphological and chemical characteristics of the samples being analyzed. While THz time-domain spectroscopy (THz-TDS) provides valuable information about the optical properties of aerosols, complementing this data with morphological and chemical analyses through techniques like scanning electron microscopy coupled with energy-dispersive X-ray spectroscopy (SEM-EDX) and X-ray diffraction (XRD) enhances the overall understanding of the samples. Additionally, we were able to confirm the consistency of the diameters measured by PROMOLED and APS with those obtained from SEM-EDX, further enhancing the morphological and chemical insights we gained.

### 2.5.1 Scanning Electron Microscopy - Energy Dispersive X-ray

#### 2.5.1.1 Principle

Scanning Electron Microscopy (SEM) is a powerful imaging technique that utilizes focused beams of electrons to generate high-resolution images of a sample's surface topography and composition. Unlike traditional light microscopy, SEM provides detailed three-dimensional images and allows for the analysis of materials at the micro- and nano-scale. EDX is integrated with SEM to provide qualitative and quantitative elemental analysis. The principle of EDX relies on the detection of X-rays emitted from the sample when it is bombarded by the electron beam. Each element has a unique set of characteristic X-ray energies, allowing for the identification and quantification of the elements present in the sample.

#### 2.5.1.2 Re-suspension and collection of particles

The resuspension process is accomplished by directing synthetic air into a glass vessel containing the particles, which are kept in motion through magnetic stirring. This setup facilitates the transport of particles to a buffer volume, where larger particles settle to the bottom while smaller ones are redirected to a filter [101]. The filters used are Nucleopore™ polycarbonate membranes with uniform pore sizes of 0.2 µm. As a result, the resuspended particles accurately represent those exposed to the THz beam. However, it's important to note that the ultrafine fraction of particles smaller than 0.2 µm is not retained due to the necessary porosity of the filters.

#### 2.5.1.3 Automated individual particles analysis

An automated JEOL JSM7100F Scanning Electron Microscope (SEM) with three Bruker QUANTAX 800 (3 x 30 $mm^2$) EDX spectrometers is deployed on GD particles with 10 mm working distance (WD) at 5kV and 200pA probe current through QUANTAX Esprit 2.0 software [111]. If one places the sample too close to the beam, that is to say with a small WD, the electrons will not be able to reach the EDX detector and the microscope could not perform EDX analysis. Backscattered electron (BSE) imaging is used for a basic assessment of homogeneity and existence of included phases, while the secondary electron (SE) detector produces topographic images and the EDX allows for the examination of elemental compositions.

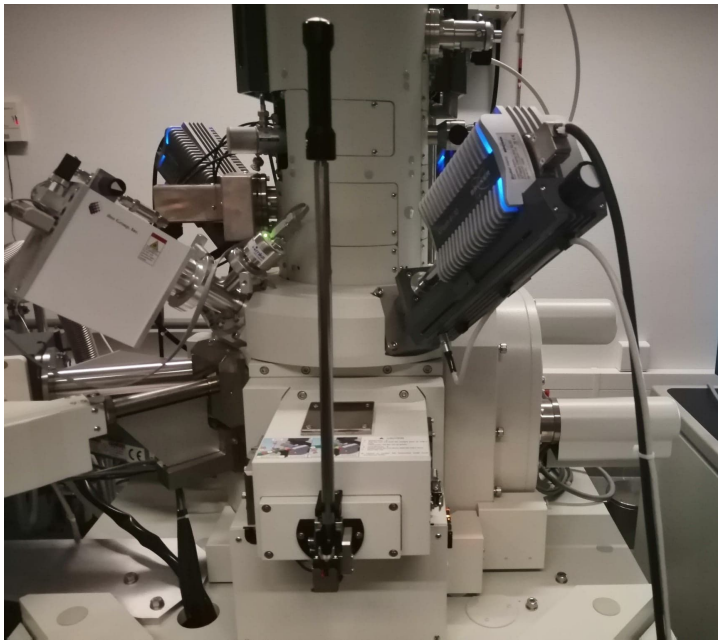

Figure 2.20: SEM-EDX from the LPCA laboratory.

A binarization process is carried out, consisting on the adjustment of the grayscale of the filters in order to reduce the amount of information to be treated. The main parameter of this adjustment is the threshold with which the brightness of the images are compared. The automated analysis is performed under morphological (post-binarization) filters such as erosion that returns the minimum value of the surrounding pixels. The analysis is also told to reject all border particles. The GD particles are coated using a sputter deposition device which applies a nanoscale layer of atoms removed from a piece of Chromium by ionized argon in a vacuum chamber in order to achieve higher resolution and magnification, as non-conductive samples often have a charging effect due to the accumulation of electrons on the surface which causes problems in collecting a proper image. The application of a potential difference between the target and the walls of the reactor within a vacuum chamber allows the creation of a cold plasma. Under

the effect of the electric field, the positive species of the plasma are attracted by the target, that is to say the cathode, and collide with the latter. They cause the sputtering of atoms in the form of neutral particles which condense on the substrate. The formation of the film takes place according to several mechanisms which depend on the forces of interactions between the substrate and the film. The presence of Cr in the analyzed particles is non-existent prior to the coating. This element is therefore not retained in the qualification element by element in the EDX spectra.

On the figure 2.20, one can see the instruments from the Laboratory of Physico-Chemistry of the Atmosphere (LPCA) in the University of Littoral Côte d'Opale (ULCO). It consists of several elements : the electron source (FEG-Field emission gun), the backscattered electron detector, the EDX detector, the secondary electron detector and the vacuum chamber (6x10$^{-4}$ Pa) where the sample is located. A first step is to slice the filters that are too large to fit into the microscope and stick them on the microscope device using a black polycarbonate surface (figure 2.21). This is done under a hood in a controlled environment, wearing gloves and with a one-time use blade. The filters are very fine and light, it may be necessary to cut the ventilation of the hood during delicate stages.

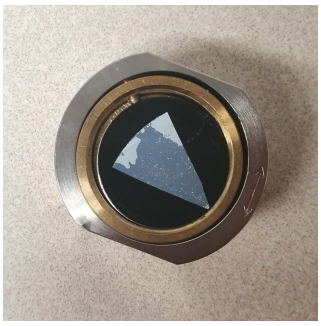

Figure 2.21: Sliced polycarbonate filter sticked on a black polycarbonate surface.

#### 2.5.1.4 Classification in clusters

Clustering consists of grouping particles according to their chemical compositions. The data collected by SEM-EDX undergoes a first sorting carried out by an iterative hard clustering technique that uses a learning algorithm in R programming language [112]. Subsequently, a second sorting is carried out by the researcher on the Esprit 2.0 software. This sorting consists in rejecting the particles such as those which moved during the analysis as well as removing or adding particles to clusters and eliminating or creating new clusters based on the elements weight percentage (wt%) ratios. Typically, a particle that contains $\geq$ 90wt% Si is classified as quartz [113]. Likewise with a calcite particle which contains a quantity $\geq$ 80wt% of Ca [114]. The clays are identified by their Si/Al wt% ratios that

are around 2.5 and they are differentiated by their other major elements such as Mg or Fe [115]. An element is considered major when it is present at $\geq$ 30wt%. The C and O content are not taken into account in the analysis because the filter is made of polycarbonate.

### 2.5.2 X-ray diffraction

X-ray diffraction (XRD) provides structural information and enables the identification of crystal phases in a sample e.g. in the case of clays where the proportion of minerals whose formula and structure vary considerably. Careful analysis of XRD data can help correlate microscopic observations with the overall sample.

The working principle of XRD is based on Bragg's Law, which describes the constructive interference of X-rays scattered by crystal planes. When a monochromatic beam of X-rays strikes a crystalline material, the atoms within the crystal lattice act as scattering centers. At certain angles, the scattered waves from different atomic planes interfere constructively, resulting in a detectable diffraction peak.

An X-ray instrument contains three main components: an X-ray source, a sample holder, and an XRD detector. The X-rays produced by the source illuminate the sample. It is then diffracted by the sample phase and enters the detector which measures the signal intensity. At the end, the processing is carried out by comparing the diffractograms obtained with those from the data library.

After the diffraction pattern is collected, the resulting diffractogram displays intensity peaks as a function of diffraction angle. Each peak corresponds to a specific set of crystallographic planes within the sample. The position, shape, and intensity of the peaks provide crucial information about the crystal structure, phase composition, and degree of crystallinity.

The obtained diffractograms are compared against standard reference patterns from crystallographic databases such as the International Centre for Diffraction Data (ICDD) or the Crystallography Open Database (COD). These libraries contain reference patterns for thousands of different minerals and materials, enabling precise phase identification.

## 2.6 Conclusion

This thesis presents the development of a novel experimental setup designed for the resuspension and THz analysis of atmospheric particles. This unique bench, carefully optimized for material selection, alignment, particle counting, and flow dynamics, allows for precise measurements that faithfully represent the behavior of aerosols in the THz domain. It marks a significant step forward in the experimental analysis of these particles under controlled conditions.

Key aspects of the data acquisition and processing were thoroughly addressed,

from capturing the signals to their refinement using the custom software tools Correct@TDS and Fit@TDS. These tools were central to the correction and fitting processes that ensured the accuracy of the retrieved data, particularly in determining the complex refractive index (CRI) and the associated uncertainties. The meticulous characterization of signal processing, including transmission and model parameter uncertainties, underscores the reliability of the methods employed.

The setup was successfully employed to investigate a range of aerosol samples, including calcite, kaolinite, and desert dust particles from the Gobi Desert. These initial experiments provide valuable insights into particle behavior in the THz range, opening the door for more advanced studies. Detailed results of these analyses will be discussed in Chapter 3, offering a deeper understanding of the THz optical properties of different mineral aerosols.

This work lays a foundation for future research, both in refining aerosol characterization techniques and extending the application of THz spectroscopy to a broader range of environmental and atmospheric studies.

# Chapter 3

# Optical characterization of desert dust and its main components in the THz domain coupled to morphological and chemical characterization at the single-particle scale

## 3.1 Introduction

Desert dust is a major atmospheric component with significant implications for climate, weather patterns, and atmospheric chemistry. Its optical properties, especially in the far-infrared and THz domains, are critical to understanding how dust interacts with solar and terrestrial radiation. In recent years, there has been growing interest in characterizing desert dust at these frequencies to better model its role in radiative forcing and to improve satellite remote sensing capabilities.

This chapter focuses on the optical characterization of desert dust in the THz domain, with a specific emphasis on dust particles from one of the largest sources of atmospheric dust : the Gobi Desert. This study can be challenging as the Gobi Desert contains a diverse array of mineral components, including quartz, calcite, illite and various feldspars. These components influence not only the chemical and morphological characteristics of the dust but also its interaction with THz radiation.

By coupling optical measurements with detailed morphological and chemical analyses at the single-particle scale, this chapter aims to provide a comprehensive understanding of how the different mineral components of Gobi Desert particles contribute to their overall optical behavior. Special attention is given to the complex refractive index (CRI) of the particles, which plays a central role in determining how desert dust absorbs and scatters THz radiation. In addition to Gobi

Desert particles, other key mineral components such as kaolinite, found in other desert regions, are analyzed to contextualize the broader implications for desert dust characterization.

All the dust samples were analyzed in pellet form, as this provides a quick and simple method to observe whether they exhibit any response in the THz range. The pellet form allows for rapid screening of the material's optical behavior, which is essential given the time constraints of this study. While this method provides valuable insights, only a subset of the samples were re-suspended into aerosols for further testing, due to limitations in time and resources.

However, having both pellet and aerosol measurements is particularly useful for comparing the effects of different environments on the samples. The THz range is highly sensitive to the medium surrounding the particles, and by analyzing the same material in both solid (pellet) and airborne (aerosol) forms, it becomes possible to better understand how the environmental context affects the material's optical properties. This comparison can highlight the role of the surrounding medium in THz absorption and scattering, offering more comprehensive data on the behavior of desert dust in real-world atmospheric conditions.

This chapter, therefore, seeks to bridge the gap between the detailed physical properties of desert dust and their large-scale optical effects in the THz domain, laying the groundwork for improved atmospheric models and remote sensing techniques.

In the table below, we summarize the analyses conducted on various samples, highlighting the methods employed and the results obtained.

| Sample | Chemical Formula | SEM-EDX | XRD | THz-TDS |
|---|---|---|---|---|
| **Potassium Feldspar** | $KAlSi_3O_8$ | ✗ | ✗ | Pellet |
| **Anorthic Feldspar** | $CaAl_2Si_2O_8$ | ✗ | ✗ | Pellet |
| **Soda Feldspar** | $NaAlSi_3O_8$ | ✗ | ✗ | Pellet |
| **Hematite** | $Fe_2O_3$ | ✗ | ✗ | Pellet |
| **Illite** | $(K,H_3O)(Al,Mg,Fe)_2(Si,Al)_4O_{10}[(OH)_2,(H_2O)]$ | ✓ | ✓ | Pellet |
| **Quartz** | $SiO_2$ | ✓ | ✓ | Pellet, Aerosol |
| **Kaolinite** | $Al_2Si_2O_5(OH)_4$ | ✓ | ✗ | Pellet, Aerosol |
| **Calcite** | $CaCO_3$ | ✓ | ✓ | Pellet, Aerosol |
| **Gobi Desert Particles** | Mixed Composition | ✓ | ✓ | Pellet, Aerosol |

Table 3.1: Summary of analyses conducted on natural atmospheric aerosol samples.

## 3.2 Sample sources description

The Gobi Desert particles analyzed in this study were sourced from an aeolian sample collected at Yanchi in Ningxia Province, China (36°29'14.39"N, 107°28'30.75"E). This site is frequently impacted by dust storms, allowing for the collection of significant amounts of atmospheric dust. A sieving process was employed to isolate particles below 100 μm in size [116–118].

For comparative analysis, we utilized several reference materials. Illite was obtained as a commercial sample of natural origin (IMt-2) from Silver Hill, Montana, USA, provided by the Clay Mineral Society. Kaolinite, another natural sample, was purchased from Sigma-Aldrich (Catalog No. 03584-250G). Quartz was sourced from Honeywell (Catalog No. S5631-100G, Lot No. G3070), while calcite was supplied by Riedel-deHaën (Catalog No. 31208).

Additionally, various feldspar samples, including anorthic feldspar (BAS-BCS-CRM 529), soda feldspar (BAS-BCS-CRM 375/1), and potassium feldspar (NCS DC61102), were acquired from LGC Standards.
Hematite (NCS DC14007A) was also sourced from LGC Standards, completing our suite of materials for comprehensive analysis.

## 3.3 Comprehensive analysis of Gobi desert particles

### 3.3.1 Elemental composition and crystallography

#### 3.3.1.1 Elemental compositions

Following the elemental analysis of 1156 particles, the GD particles are classified into three main clusters : clays (61.56% in number), calcite (cluster 2 - 29.38%)- and quartz (cluster 1 - 9.06%) (Fig. 3.1). The number of particles and elemental weight percentages in each cluster can be visualized on table 3.2. One additional cluster corresponding to particles whose signal is too weak was also designated as unworkable and contains 160 particles.

The clays of the Gobi desert are mainly composed of Si and Al oxides with varying amounts of Na, K, Mg, Ca, Fe and Ti. The composition of clays is highly variable depending on its source and any given locality can contain many subtly different types of clay minerals with radically changing individual composition in a few cm [119]. Their various compositions lead to the creation of seven secondary clusters, namely illite, and Fe rich, Ca rich, Fe-Mg rich, Ca-Fe rich, Ti rich and Ca-Mg rich aluminosilicates. We can hypothesize that the Ca-rich cluster is a calcite pole plagioclase, more commonly called anorthite [120, 121]. The Fe and Ti rich clusters are probably Fe and Ti oxides that are attached to or internally mixed with clay particles.

The absence of chloride in the Gobi Desert (GD) particles can be attributed to their origin, far from river basins, as minerals—except chloride-rich salts—typically

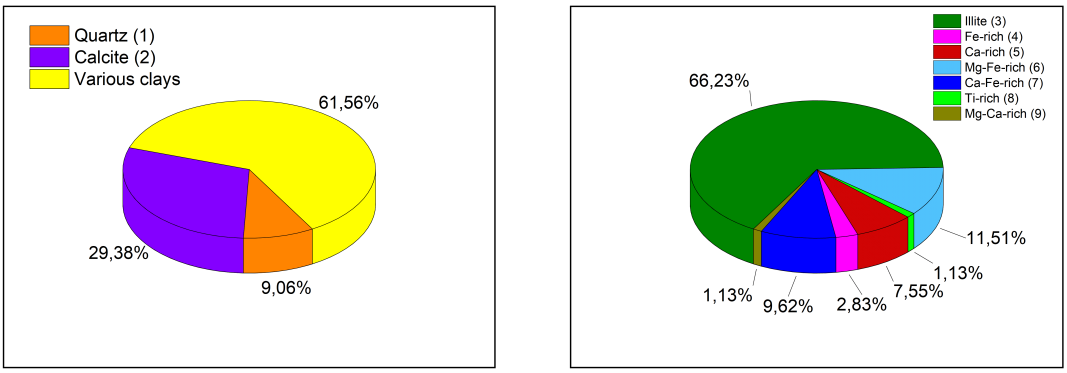


Figure 3.1: Cluster distribution diagram of main clusters on the left (i.e. clays for 61.6%, calcite for 29.4% and quartz for 9.1%. Secondary clay cluster distribution is represented on the right.

Table 3.2: Table of the number of particles, the total weight percentages of each cluster in the GD sample, elements weight ratios (excluding carbon, oxygen and chromium) in each cluster and the identification guess based on the main compounds.

| Cluster | 1 | 2 | 3 | 4 | 5 | 6 | 7 | 8 | 9 |
|---|---|---|---|---|---|---|---|---|---|
| Number | 90 | 293 | 406 | 17 | 46 | 71 | 59 | 7 | 7 |
| Total (wt%) | 9.1 | 29.4 | 40.8 | 1.7 | 4.6 | 7.1 | 5.9 | 0.7 | 0.7 |
| Si (wt%) | 92.1 | 9.0 | 54.3 | 9.4 | 29.5 | 32.3 | 34.9 | 20.6 | 7.9 |
| Al (wt%) | 3.7 | 3.8 | 20.9 | 5.7 | 10.8 | 17.7 | 16.2 | 8.2 | 2.9 |
| Ca (wt%) | 1.2 | 84.3 | 3.3 | 1.0 | 51.7 | 1.5 | 23.8 | 5.7 | 54.1 |
| Fe (wt%) | 1.7 | 0.7 | 8.0 | 78.9 | 4.3 | 35.2 | 15.0 | 4.5 | 3.8 |
| K (wt%) | 0.4 | 0.0 | 7.3 | 0.2 | 0.8 | 1.4 | 2.8 | 1.6 | 0.0 |
| Mg (wt%) | 0.8 | 1.8 | 4.5 | 1.9 | 2.9 | 11.1 | 5.7 | 1.8 | 31.2 |
| Na (wt%) | 0.1 | 0.0 | 1.2 | 0.2 | 0.1 | 0.4 | 0.2 | 0.0 | 0.0 |
| Ti (wt%) | 0.0 | 0.0 | 0.1 | 1.7 | 0.0 | 0.0 | 0.4 | 57.6 | 0.0 |
| Mn (wt%) | 0.0 | 0.0 | 0.0 | 0.5 | 0.0 | 0.0 | 0.0 | 0.0 | 0.0 |
| Zn (wt%) | 0.0 | 0.0 | 0.3 | 0.0 | 0.0 | 0.1 | 0.0 | 0.0 | 0.0 |
| S (wt%) | 0.0 | 0.3 | 0.0 | 0.3 | 0.0 | 0.0 | 0.3 | 0.0 | 0.0 |
| Cl (wt%) | 0.0 | 0.0 | 0.0 | 0.1 | 0.0 | 0.0 | 0.1 | 0.0 | 0.0 |
| P (wt%) | 0.0 | 0.1 | 0.0 | 0.1 | 0.0 | 0.1 | 0.5 | 0.0 | 0.0 |
| Guess | Quartz | Calcite | Illite | Fe rich | Ca rich | Fe-Mg rich | Ca-Fe rich | Ti rich | Ca-Mg rich |

contain low levels of chloride [122]. Furthermore, the formation of zinc-rich clays is often associated with the interaction between zinc-rich meteoric water and pre-existing clays. This process does not appear to have occurred in the GD particles [123, 124]. While preliminary identification of these clays can be proposed based on mass percentage ratios, definitive conclusions cannot be drawn without further analysis of their oxide structures. Consequently, we have opted to classify the clays based on their predominant compounds.

SEM-EDX was also performed on the commercial samples in order to compare with the main clusters. Only 80.5% of Illite from Montana matched the composition of the illite cluster of GD particles. Illite from Montana can be divided into 12 clusters, and therefore contains other clay compound clusters which also correspond to secondary clay clusters of the GD [119]. Elemental compositions of commercial quartz and calcite coincided with the quartz and calcite clusters from GB with around 7.9% impurities for cluster 1 and 15.7% for cluster 2, probably due to small particles from other clusters which are stuck on them. Alternatively, it could mean that the particles are internally mixed although quartz are known as not well mixed within the Mongolian Gobi particles [125].

#### 3.3.1.2 Crystallographic structures

The figure 3.2 shows the XRD patterns of the dust from GD and the 3 commercial samples: calcite, illite and quartz. It can be seen following the dotted lines that the peaks of the 3 commercial samples coincide with those of the natural Gobi dust except for peaks of negligible intensity such as at 22.2°or 41.9°. Quartz and calcite have strong peaks intensities, meaning that the amount of crystalline structure with the same phase is high compared to that of illite. The peaks are weaker and larger for illite from Montana, which can be an indicative of smaller crystallite sizes or the presence of a more disordered phase.

All major peaks from the main compounds—quartz, illite, and calcite—are present in the diffractogram of the Gobi particles, confirming that these minerals are dominant in the GD sample. This strong overlap suggests that the mineralogical composition of the Gobi dust includes significant quantities of these crystalline phases. The presence of all major peaks from calcite, quartz, and illite in the Gobi dust sample also points to the likelihood of mixed-phase materials.

The maximum intensity of the peak at 29.5°of the GD particles can be retrieved with an error of 0.03% by applying the weight percentage of the calcite cluster in Figure 3.1 to the intensity of its peak at 29.5°(see equations (3.1) and (3.2)).

$$I(29.5^\circ)_{Gobi} \approx I(29.5^\circ)_C \times wt_C \tag{3.1}$$

$$1532 \approx 5368 \times 0.294 \tag{3.2}$$

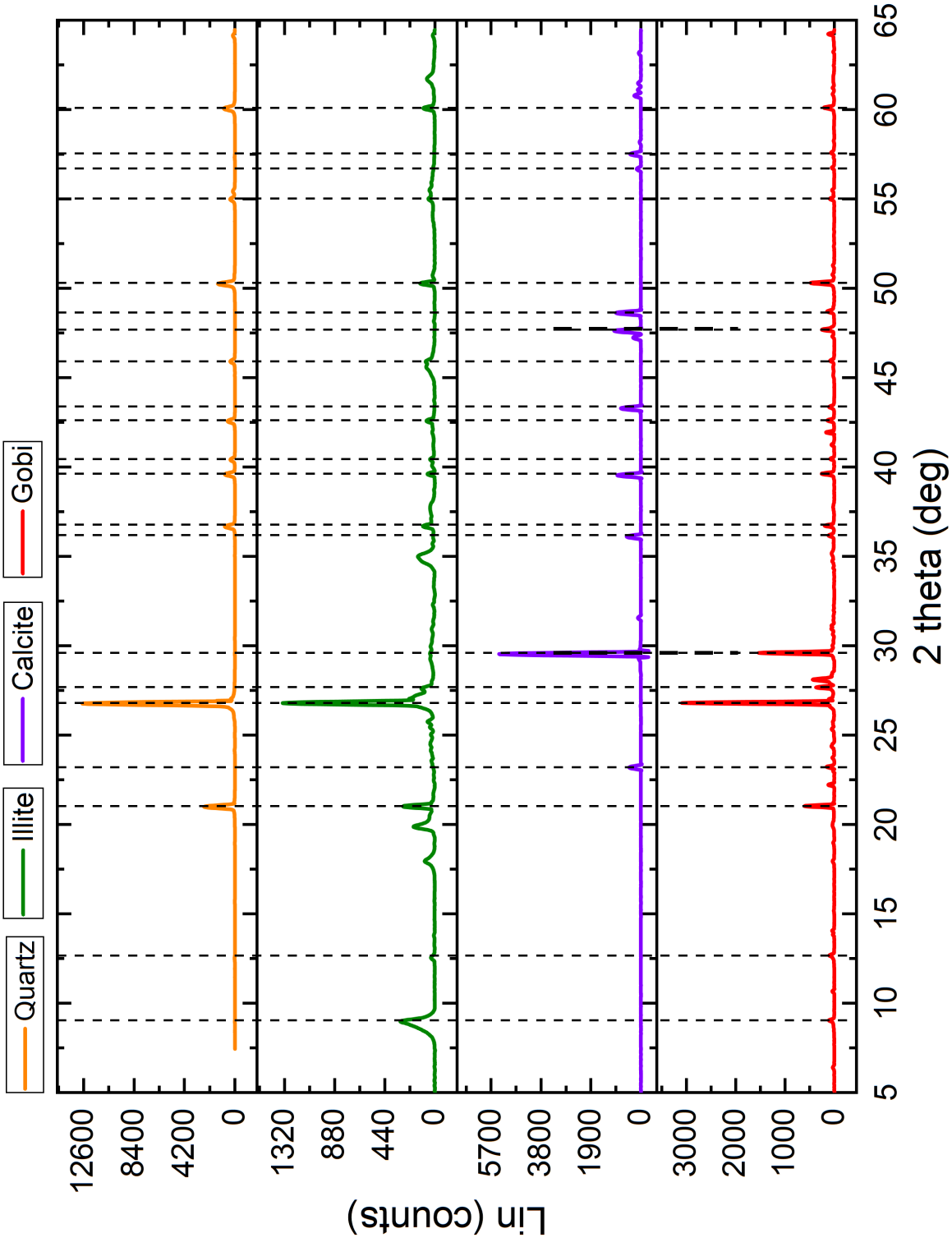


Figure 3.2: Powder X-ray diffraction patterns of pure commercial quartz (orange), illite from Montana (green), commercial calcite (purple) and Gobi desert particles (red).

However, this calculation is not applied to the peak at 26.7°for quartz, illite (Montana), or GD, as this peak likely corresponds to a common phase shared between quartz, illite, and other feldspars containing silicon oxides. Since 33.8% of the clay composition is not represented, and the Montana illite sample is not pure, this peak may represent overlapping contributions from multiple silicate phases, complicating its use for precise quantitative analysis.

When applying the mass percentage obtained from the automatic SEM analysis of Gobi dust particles to this peak, the resulting peak intensity is 1618, whereas the expected intensity is nearly double (see equations 3.3 and 3.4). Even when the mass percentage of all clays is applied to the illite peak intensity, the result still does not reach 3000. This suggests that the crystalline phases may be more abundant in the Gobi dust particles than in the commercial illite sample.

$$I(26.7^\circ)_Q \times wt_Q + I(26.7^\circ)_I \times wt_I \approx 12650 \times 0.091 + 1330 \times 0.351 \tag{3.3}$$

$$I(26.7^\circ)_Q \times wt_Q + I(26.7^\circ)_I \times wt_I \approx 1618 \tag{3.4}$$

With :

- $I(26.7^\circ)$ and $I(29.5^\circ)$, peak intensities at 26.7°and 29.5°respectively.
- $wt$ the weight percentage retrieved by automatic SEM-EDX analysis of Gobi Desert particles (calcite ($C$), quartz ($Q$) and illite ($I$)).

For comparison purposes, all data here were normalized according to the mass of each powder before plotting and comparing peak intensities.

These calculations should be interpreted with caution, as multiple factors can influence XRD peak intensities beyond the actual proportions of mineral phases in the sample. For instance, the crystallographic orientation of the particles relative to the X-ray beam can cause peak intensities to vary, meaning that observed intensities may not always reflect true phase abundance.

Additionally, particle size and shape play significant roles. Smaller crystallites or particles with irregular shapes can lead to peak broadening and intensity reduction, especially visible for minerals like illite, where broader peaks might indicate smaller or more disordered structures.

While the qualitative comparison between the XRD patterns shows good agreement between the Gobi dust and the commercial samples, a more quantitative analysis, such as using Rietveld refinement, could offer precise data on the relative proportions of quartz, calcite, and illite in the dust. This would help refine the understanding of the dust's mineralogical composition and allow for more accurate predictions of its environmental and geochemical impacts.

### 3.3.2 Morphological analysis linked to the chemical composition

The varied chemical compositions of GD particles generates very rich morphologies that can be visualized on the few micrographs presented in this study (figure 3.3). The spectrum corresponding to each particle is recorded (figure 3.4), which enables to obtain cluster affiliations of the analyzed particle.

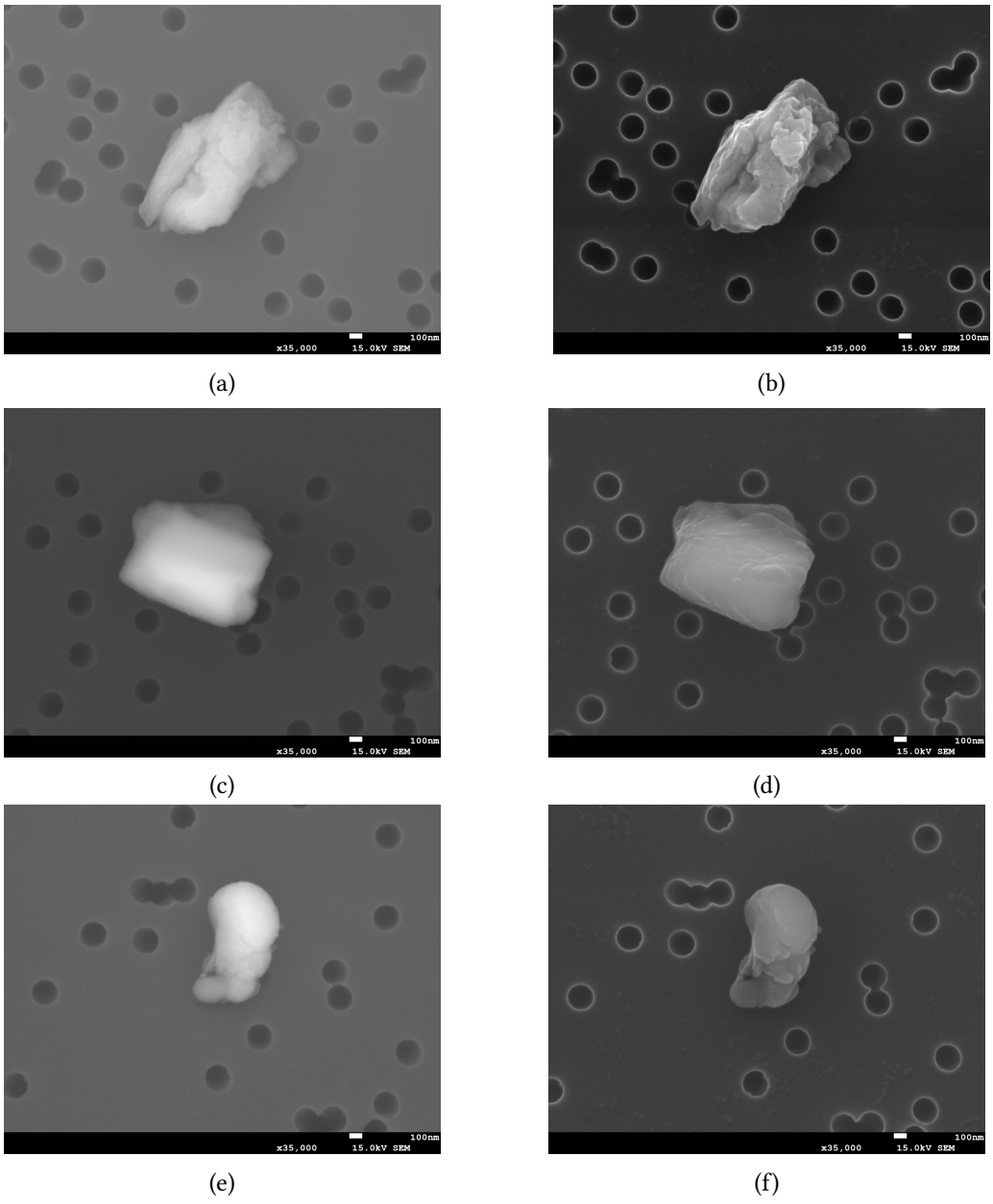


Figure 3.3: BSE (a-c-e) and SE (b-d-f) micrographs of particles from Gobi Desert particles. C and O are excluded from the analysis. Particles were coated with Cr. The particle in (a) and (b) corresponds to the cluster 5 (Ca rich Al-Si), the one in (c) and (d) matches with the cluster 8 (Fe rich Al-Si). Finally the particle in (e) and (f) is from the cluster 9 (MgCa rich Al-Si).

The particle shown in (a) and (b) on figure 3.3 corresponds to cluster 5 and is identified as a calcium-rich aluminosilicate, likely anorthite. This type of particle

shares similarities with the commercial calcite particles. It is clearly an aggregate composed of several particles, with smaller particles adhering to the larger ones.

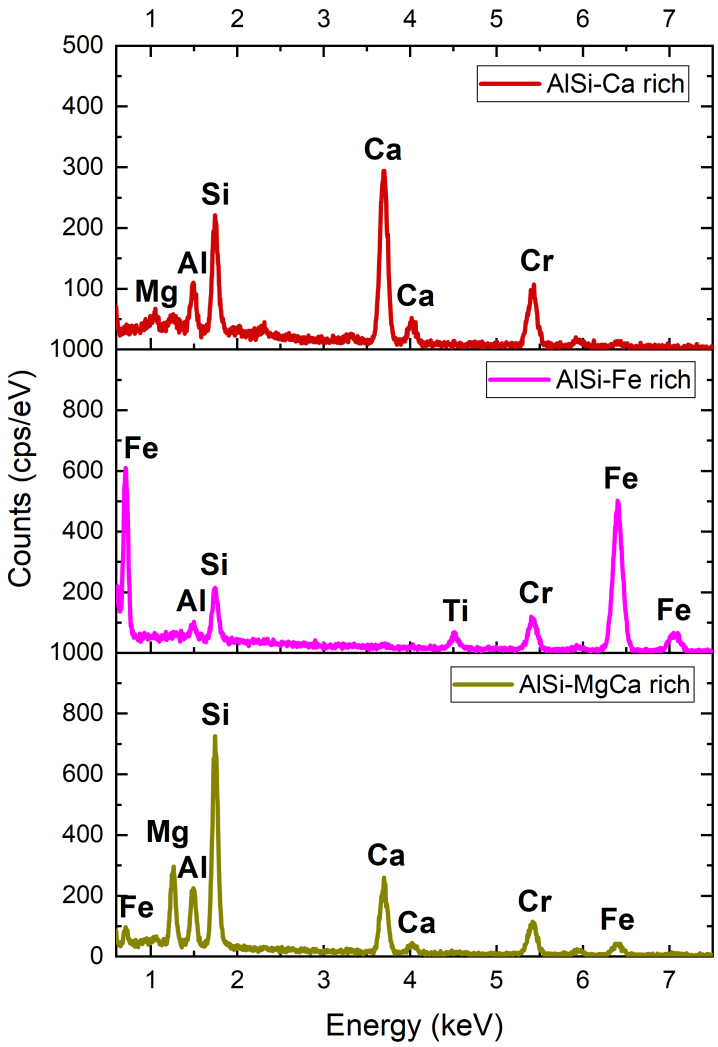


Figure 3.4: EDX spectrum corresponding to particles from the cluster 5 (Ca rich Al-Si), the cluster 8 (Fe rich Al-Si) and the cluster 9 (MgCa rich Al-Si).

The particle depicted in (c) and (d) belongs to cluster 8 and is an iron-rich aluminosilicate. It may represent an externally mixed particle containing feldspar and hematite, which would explain the presence of titanium, as hematite is known to contain trace elements like Mn and Ti. The hypothesis of external mixing is supported by the particle's rhombohedral shape observed in the micrograph, which is characteristic of hematite's crystal structure.

The final particle shown in (e) and (f) corresponds to cluster 9 and is a magnesium- and calcium-rich aluminosilicate. This particle, measuring a few hundred nanometers, appears to be constructed in a layered fashion, with smaller particles stacked on top of each other. This shape may result from the collection process, where

particles are deposited one atop the other.

The figure above (fig. 3.4) shows the EDX spectra acquired for these particles. These spectra are representative of all the particles within their corresponding clusters. As noted, there is always a consistent presence of silicon and aluminum in the spectra. The detected presence of chromium is attributed to the metallization process that was carried out prior to SEM-EDX analysis, where a thin chromium coating was applied to the samples for improved conductivity.

As previously mentioned, some particles are excluded from the analysis during sorting because their spectra show little or no detectable signal. Figure 3.5 provides an example of a micrograph of such a particle. The absence of signal in these particles is not due to their size, as this particle, measuring a few microns, is actually slightly larger than the average particle diameter analyzed. The BSE micrograph provides insight into the distribution of elements within the structure, though it does not indicate specific composition. In the case of this particle, the elements appear to be evenly distributed, and the recorded response is still strong, as indicated by the particle's bright appearance in the image. Therefore, the weak signal is not due to a lack of material.

These particles may, in some cases, consist of carbon, hydrogen, and oxygen, elements that are excluded from the analysis because the filter used is made of polycarbonate. This raises the possibility that they could be microplastics. A study conducted in the Badain Jaran Desert, the second largest desert in China, found that the abundance of microplastics in uninhabited areas was approximately 6.0 ± 15.4 items/kg. This microplastic pollution likely originates from atmospheric transport from populated areas or tourist activity in the desert [126].

Another possibility is contamination during sample resuspension or SEM-EDX analysis. However, particle-free reference filters (collected by placing them in the resuspension setup without particles) were also analyzed by SEM-EDX, and these tests confirmed that the filters were clean, making contamination from the experimental setup unlikely. That said, these particles account for 160 instances, which is a substantial number to attribute to contamination alone.

Nonetheless, the recording of EDX spectra from some initially signal-free particles revealed a chemical composition comparable to that of the clusters. These spectra were recorded by identifying and manually registering the EDX spectrum of a particle that initially showed no signal during automatic analysis. This reinforces the notion that the absence of signal in these cases may be attributed to technical issues during spectrum acquisition, and it should be considered a source of uncertainty in the measurements.

For instance, the initially signal-free particle identified is an external mixture of quartz and iron-rich aluminosilicate, as shown in figure 3.5. The quartz portion appears as the lighter section of the particle, which seems situated next to and slightly above the area containing an iron-rich aluminosilicate. This deter-

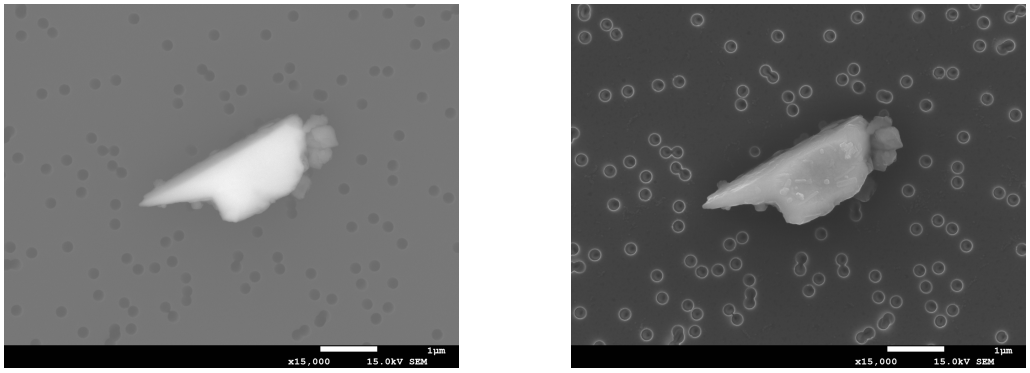


(a) (b)

Figure 3.5: BSE (a) and SE (b) micrographs of particle showing initially no signal on the EDX spectrum of the automatic analysis.

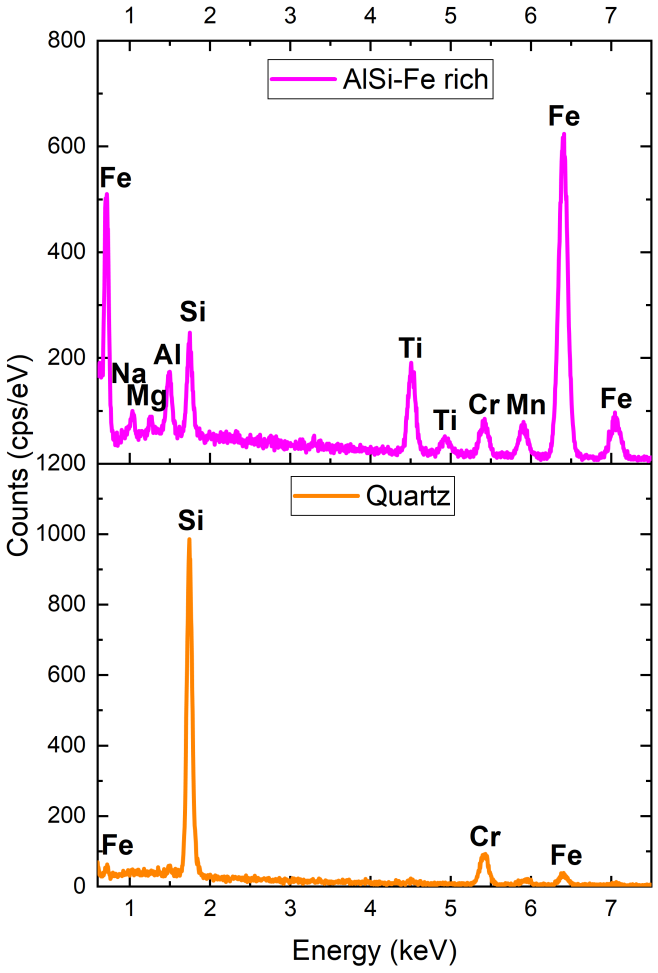


Figure 3.6: EDX spectra of the manually selected two areas of the particle initially showing no signal.

mination was made by selectively analyzing different regions of the particle and acquiring the spectrum specifically from the quartz and iron-rich aluminosilicate areas. These observations support the hypothesis that the quartz and iron-rich particles are externally mixed within the Gobi dust particles.

Figure 3.6 shows the two selectively acquired spectra. The spectrum of the quartz appears pure, with the exception of a trace of iron from the hematite. In contrast, the spectrum from the iron-rich aluminosilicate shows a composition typical of particles from cluster 4. However, the response from the iron oxide rich aluminosilicate could not be selectively separated here, preventing any conclusions about whether an internal or external mixing occurred.

Future studies should aim to utilize advanced imaging techniques to better distinguish between internal and external mixing. Understanding the formation mechanisms of these mixed particles can contribute to our understanding of the composition and behavior of Gobi Desert dust. This is particularly important for understanding their optical behavior, as the response of light will vary depending on whether the mixing is internal or external. This distinction is especially crucial in the THz range, where we are particularly sensitive to the structural characteristics of the particles.

### 3.3.3 Optical properties of Gobi Desert particles

#### 3.3.3.1 Pellet measurement

The Gobi Desert particles were initially analyzed in pellet form as a quick and efficient method for assessing their optical response in the THz domain. This approach is particularly advantageous given the limited supply of Gobi Desert particles available in the lab, as the pellet form allows for minimal sample usage.

For the pellet measurements, 12 mg of Gobi Desert particles were mixed with docosane to achieve a total mass of 100 mg. This mixture was then pressed under 5.01 tons of pressure for approximately 5 minutes to form a pellet.

The extinction spectrum of the Gobi particles in pellet form, shown in Figure 3.7, reveals a distinct band around 3 THz. This band appears to split into two components, with one peak near 2.8 THz and another at 3.2 THz.

While useful for initial characterization, pellet measurements may not fully capture the particles' behavior in a more dynamic atmospheric context, such as when they are suspended in air.

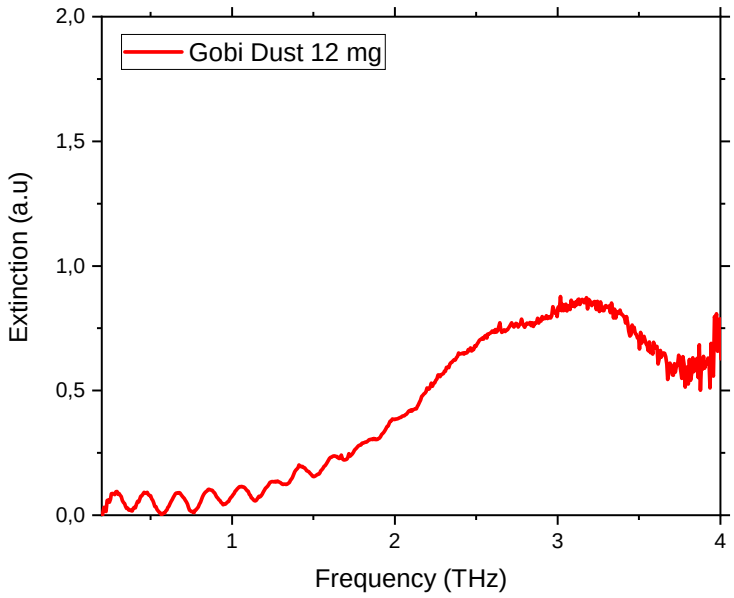


Figure 3.7: Pelletized Gobi Desert particles extinction for 12 mg in the THz range.

#### 3.3.3.2 Aerosol measurement

In comparison to the pellet measurements, the signal obtained from the aerosol analysis is notably weaker. The Gobi Desert particles displayed a prominent absorption feature centered at 3 THz, with a bandwidth of approximately 1 THz, when analyzed in aerosol form (Figure 3.8). This extinction was recorded at a particle concentration of 1.632 mg/m$^3$ and a particle count of 2.037 particles/cm$^3$. The differences between the responses in pellet and aerosol forms may be attributed to size effects, as the pellets consist of much larger particles, while only smaller particles are resuspended in the aerosol. This distinction in particle size is a significant factor in the observed variations in optical response, making it natural to expect different absorption characteristics between the two measurement methods.

The experimental particle size distribution shows that most Gobi particles have diameters below 1 µm, with a mode around 0.4 µm (Figure 3.9).

The experimental size distribution obtained was compared to the size distribution determined from automated SEM analysis, which provides average diameters that are the Feret diameters. The SEM analysis of 1,156 Gobi Desert particles revealed average diameters ranging from 0.171 to 7.596 µm. One limitation of the size distribution analysis is the uneven number of particles in each cluster, which may affect statistical accuracy. For example, Cluster 8 contains only 7 particles, and Cluster 9 was excluded from the size distribution analysis due to its small sample size. Nevertheless, several trends emerged from the data. Clusters 2 (cal-

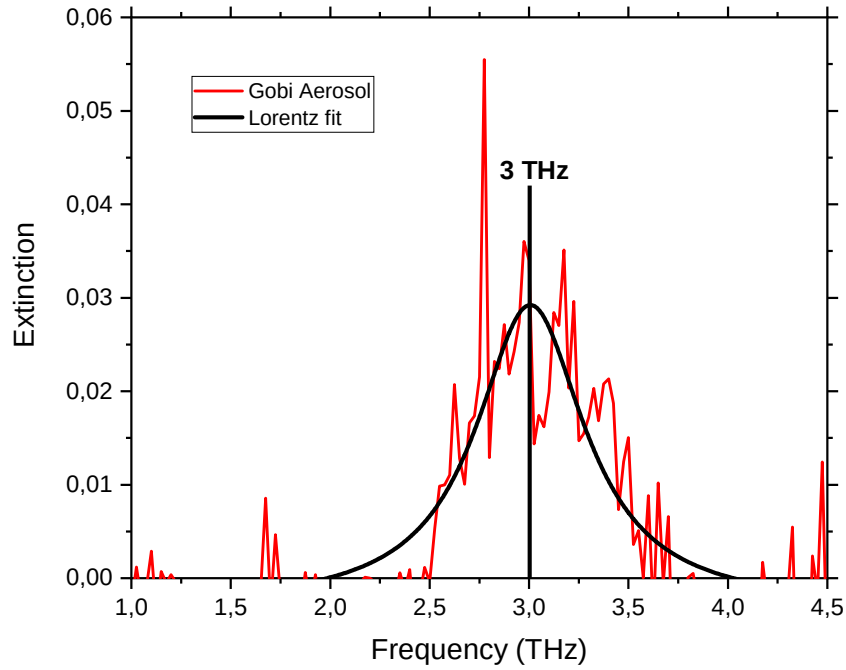


Figure 3.8: Resuspended Gobi Desert particles extinction in the THz range (red) and the Lorentian fit of the band (black).

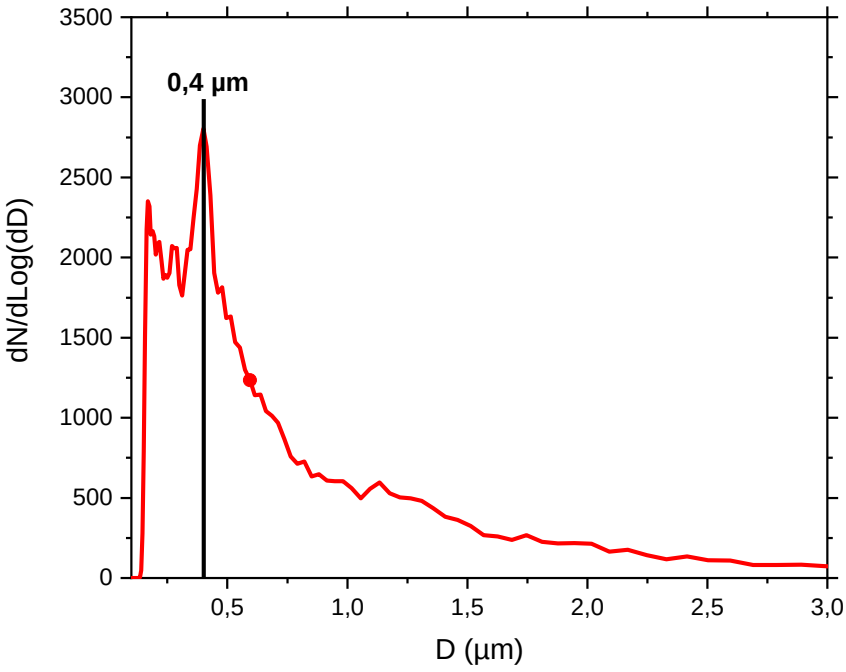


Figure 3.9: Resuspended Gobi Desert particles size distribution.

cite) and 3 (identified as illite) exhibit very similar size distributions. In contrast, Cluster 1 (quartz) and Cluster 7 contain particles with slightly larger diameters. The smallest particles were found in Clusters 5 and 8, consisting of aluminosilicate minerals rich in Ca and Ti, respectively, with 92% of the particles in Cluster 5 measuring less than 1.3 µm (figure 3.10).

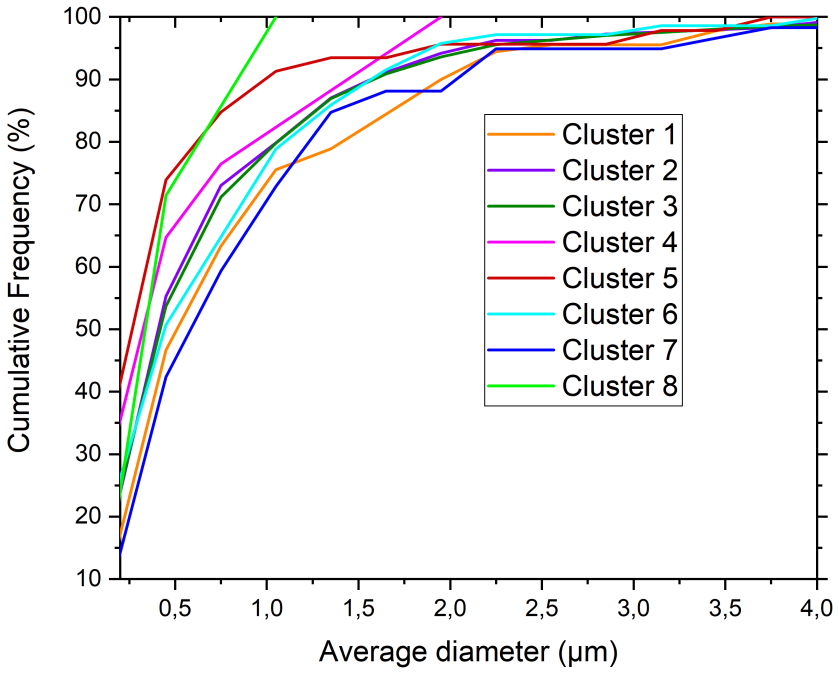


Figure 3.10: Cumulative frequency size distribution for each cluster of Gobi Desert particles.

The consistency between the PROMOLED and SEM results reinforces the observation that Gobi Desert particles, despite their varied morphologies and compositions, predominantly fall within the submicron size range. The close alignment of these two independent methods strengthens the reliability of the size distribution data, with both confirming a significant concentration of fine particles around the 0.4 µm mark in the Gobi Desert sample.

However, differences in particle sizes between these methods can also be attributed to the distinct measurement techniques used for determining diameters. The optical diameter obtained from PROMOLED measurements and the Feret diameter from SEM automated analysis represent particle size in different ways. The optical diameter reflects how a particle interacts with light and is defined as the diameter of a sphere that would produce the same optical response as the actual particle. This method assumes spherical behavior for simplicity, which makes it particularly relevant for optical studies.

On the other hand, the Feret diameter is a geometric measurement representing the distance between two parallel tangents on a particle's projection and can

vary depending on the particle's orientation in the image. Because it directly measures the particle's physical geometry, the Feret diameter accounts for irregular shapes, providing a more accurate representation of the particle's true size and form.

These differences in measurement techniques can explain some of the variations observed between the two methods. While the optical diameter is crucial for understanding optical responses and interactions with light, the Feret diameter offers a more detailed understanding of the particle's actual physical dimensions.

#### 3.3.3.3 Effective complex refractive index extraction

The refractive index analysis of the Gobi Desert particles in pellet form reveals that the extinction peak at 3.2 THz is significantly flatter in the imaginary part, likely due to the steeper slope of the real part. The pellet's optical response was fitted using two Lorentz oscillators and one Boltzmann term. The first Lorentz oscillator has a frequency mode at 2.68 THz with a linewidth of 1.67 THz, while the second one is centered at 3.29 THz with a linewidth of 0.74 THz. These frequency modes differ slightly from the direct measurements presented in Section 3.3.3.1, but are considered more reliable as they result from oscillator fits. The fitted thickness of the pellet is 0.52 mm.

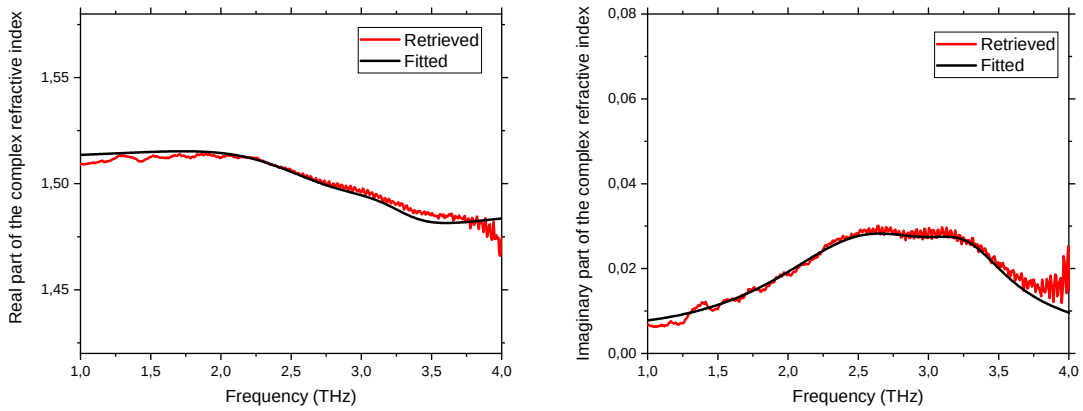


(a) (b)

Figure 3.11: The retrieved and fitted real (a) and imaginary (b) parts of pelletized Gobi Desert particles.

For the aerosol form, the fit resulted in a frequency mode of 3.00 THz with a linewidth of 0.80 THz. However, the real part shows less agreement with the Lorentz oscillator model, as shown in Figure 3.12.

The discrepancy in the real part suggests that the limitations of the measurements could have influenced the results; however, a lack of sufficient Gobi Desert particle samples prevents us from repeating the experiment. Notably, the real part

of the aerosol data indicates the presence of two oscillators, resembling the profile observed in pellet form.

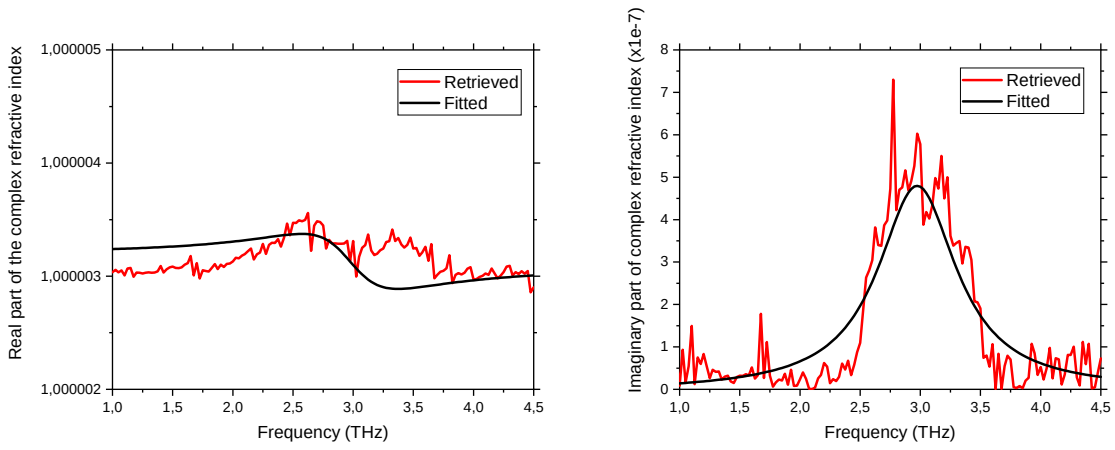


(a) (b)

Figure 3.12: The retrieved and fitted real (a) and imaginary (b) parts of the CRI of resuspended Gobi Desert particles in nitrogen flow at atmospheric pressure.

Aerosolized particles, particularly in complex mixtures like those derived from the Gobi Desert, often behave as an effective medium rather than as pure substances. For such external mixtures, models that consider each particle type independently and combine their optical effects by weighting according to volume or mass fractions provide a more accurate representation. Adopting this method could potentially yield better fits for the real part of the refractive index compared to the Lorentz oscillator approach.

## 3.4 Specific contribution of key components

As discussed earlier, the Gobi Desert particles represent a natural sample, with morphological and chemical characterization revealing a highly diverse composition. In the following sections of this chapter, we will focus on different pure compounds to better understand the optical response of the Gobi particles.

### 3.4.1 Illite

#### 3.4.1.1 Elementary composition and morphology

Illite is typically classified as an octahedral aluminous mineral belonging to the potassium mica family. However, its chemical structure can vary due to substitutions in the tetrahedral, octahedral, and interlayer sites [127]. The chemical composition of illite reported in previous studies, which identifies illite/smectite layers (47.1% Si, 35.4% Al, 12.8% K, 2.4% Mg, and 0.7% Fe), aligns with the composition provided by the Clay Mineral Society for the purchased sample [128].

In this study, a comprehensive SEM-EDX analysis was conducted on 533 resuspended and collected particles. The sample was categorized into 12 distinct clusters, with 89.12% of the particles identified as illite. This was followed by quartz, which constituted 6.38% of the sample, and Fe-rich Al-Si particles, accounting for 1.88%. The remaining clusters, which included P-rich Al-Si, Ca-rich Al-Si, and Ti-rich Al-Si, comprised less than 1% of the total sample and represented fewer than four particles out of the 533 analyzed, rendering their contributions negligible.

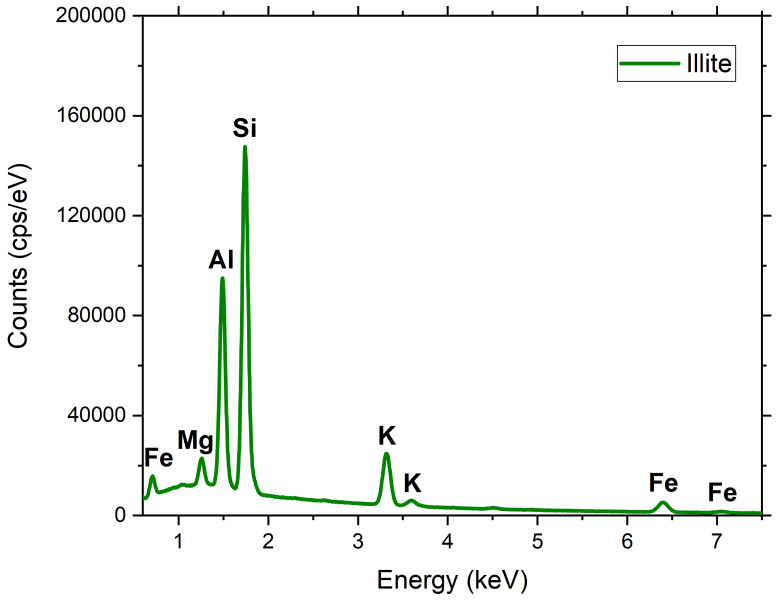


Figure 3.13: EDX spectrum of resuspended and collected illite particles that were collected on a polycarbonate filter with 0.2 µm pores. This spectrum corresponds to the illite cluster of the particles that accounts for 89.12% of the analyzed 533 particles. C and O are excluded from the analysis.

The illite cluster identified through the SEM-EDX analysis shows a composition of 47.8% Si, 22.6% Al, 13.9% K, 11.3% Fe, 2.6% Mg, with other trace elements such as Ca and Cl contributing less than 0.5%. The EDX spectrum for this cluster is shown in Figure 3.13. Interestingly, the Montana illite sample analyzed here contains a higher-than-expected Fe content, classifying it as Fe-illite. This Fe enrichment is likely due to external inputs of $K^+$, as well as seasonal wetting and drying cycles that cause soil particles to aggregate, promoting the accumulation of elements like Ca, Mg, and Fe [129].

Micrographs of the resuspended illite particles were captured using BSE detector for chemical contrast and the SE detector for topographical contrast, as shown in Figure 3.14. The background corresponds to the Nucleopore™ filter with 0.2 µm pores.

Illite is known for its unique structure, where the charge between its layers

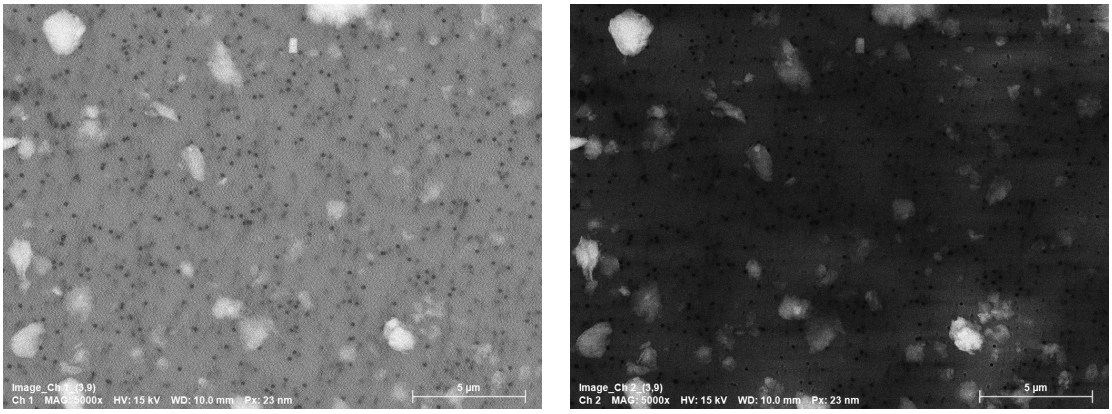


(a) (b)

Figure 3.14: BSE (a) and SE (b) micrographs of resuspended and collected illite particles.

is primarily balanced by potassium ions. These K-rich minerals often exhibit a crystalline structure similar to mica, forming stacks of extremely thin, cleavage-separable sheets [130]. The SEM analysis revealed this characteristic sheet-like arrangement in the illite particles.

The automatic SEM-EDX analysis provided an average particle diameter of 1.15 µm, with a standard deviation of 0.62 µm. The largest particle measured 1.58 µm in diameter, while the smallest measured 0.7 µm. The particles tend to exhibit an elongated shape, with an average aspect ratio of 1.65, indicating that their length is greater than their width.

#### 3.4.1.2 Pellet measurement

For this measurement, 12 mg of illite were mixed with docosane to achieve a total mass of 100 mg, and a pressure of 5.21 tons was applied for about 5 minutes to form the pellet. Similar to the Gobi Desert particles, the extinction spectrum of illite reveals two distinct bands around 3 THz, with one peak at 2.8 THz and another at 3.2 THz. Previous studies on illite in the far-infrared region identified similar bands at 93 $cm^{-1}$ (2.8 THz) and 107 $cm^{-1}$ (3.2 THz) [131]. Based on research on potassium micas (K-micas), these bands have been attributed to the torsional mode of the interlayer cations, supporting the findings of this study.

The extinction spectrum of illite closely resembles that of the Gobi Desert particles. As illustrated in Figure 3.15, The extinction of pure illite at 70% aligns well with a portion of the extinction of Gobi Desert particles, when comparing equal masses. However, there remains a more intense feature around 3 THz that illite alone cannot account for. This suggests that other mineral components in the Gobi sample contribute to the remaining extinction. This band is likely due to the more complex mineral composition and interactions between the different components in the Gobi sample, in contrast to the relatively pure illite spectrum.

The extinction characteristics are also influenced by the diverse morphologies

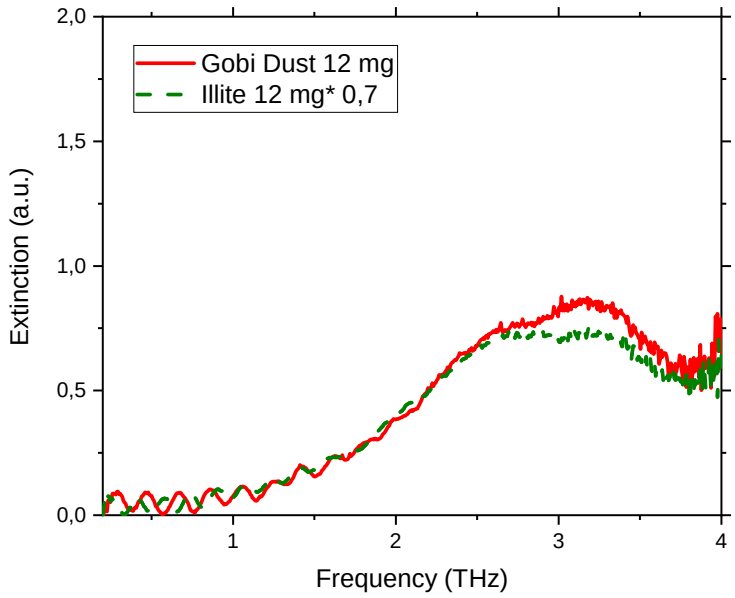


Figure 3.15: Pelletized illite particles extinction for 12 mg in the THz range compared to that of 12 mg Gobi Desert particles, both diluted in docosane.

of the particles. Illite, a sheet-like mineral, has different scattering and absorption properties compared to more compact or irregularly shaped minerals, which may explain the broader and more complex extinction profile of the Gobi Desert particles. Additionally, desert dust particles, including those from the Gobi, tend to absorb moisture from the atmosphere. The water content in these particles could alter the THz extinction, potentially broadening or shifting absorption bands. Illite, known for its hydrophilic properties, may also interact with water vapor, which can further complicate the spectral response compared to the pure illite sample.

In conclusion, while illite plays a major role in the extinction spectrum of Gobi Desert particles, the unique mineralogical composition and particle size distribution of the Gobi dust introduce additional complexities. Unfortunately, illite particles could not be resuspended for direct comparison with Gobi particles due to the limited sample availability, preventing further aerosol-based investigations to confirm these hypotheses.

#### 3.4.1.3 Effective complex refractive index extraction

The extracted effective complex refractive index of pelletized illite is shown in Figure 3.16. As anticipated, its refractive index closely resembles that of the pelletized Gobi Desert particles. Both the real and imaginary parts of the refractive index were successfully fitted using two Lorentz oscillators and one Boltzmann

term, consistent with the modeling applied to the Gobi Desert particles. The Lorentzian components capture the resonance effects, while the Boltzmann term accounts for the broader background absorption. The similarity between the illite

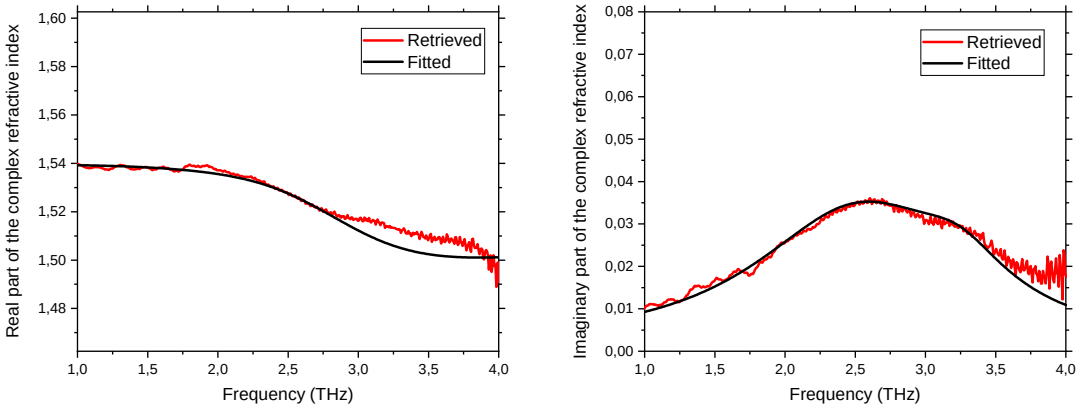


(a) (b)

Figure 3.16: The retrieved and fitted real (a) and imaginary (b) parts of pelletized illite particles.

and Gobi Desert particles in terms of their refractive index validates our modeling approach, confirming the robustness of the retrieval methods used. This close match also suggests that illite is a major contributor to the overall THz response of Gobi Desert aerosols.

### 3.4.2 Calcite

#### 3.4.2.1 Elementary composition and morphology

The calcite sample used in this study is synthetically produced, ensuring that its chemical composition is considered pure. Calcite particles are easily identifiable by the presence of a single prominent calcium (Ca) peak in the EDX spectrum, as carbon (C) and oxygen (O) are excluded from the analysis.

In addition to the calcium peak, the absence of other significant elemental signals further supports the conclusion that the calcite sample is free from common impurities such as magnesium or iron, which can often be found in naturally occurring calcite. This level of control is crucial for comparative studies involving naturally occurring dust particles, such as those from the Gobi Desert, where chemical variability can introduce complexities in data interpretation.

The micrograph of resuspended calcite aerosols, displayed in figure 3.18, reveals that most particles exhibit the typical rhombohedral shape associated with calcite.

In some instances, smaller nanometer-scale particles are seen adhering to larger micron-sized particles, likely due to calcite's hygroscopic properties, which cause it to absorb moisture from the air. Alternatively, these aggregations may result

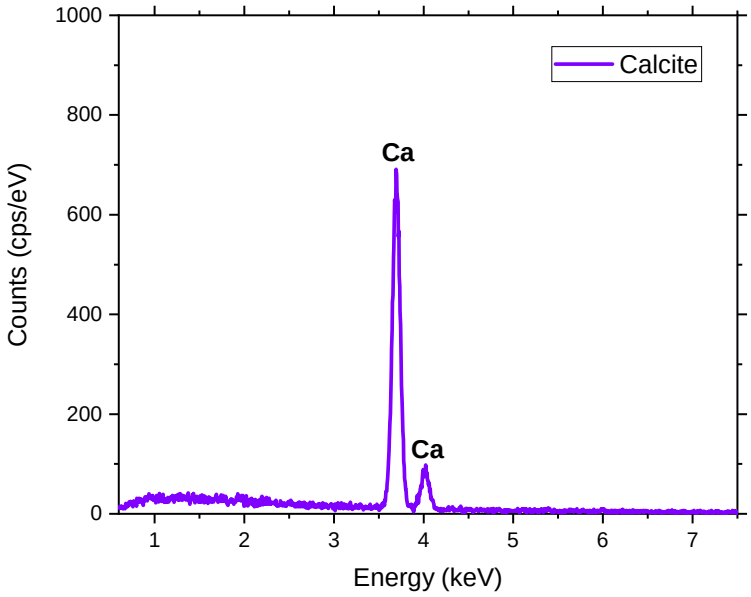


Figure 3.17: EDX spectrum of resuspended and collected calcite particles that were collected on a polycarbonate filter with 0.2 µm pores. C and O are excluded from the analysis.

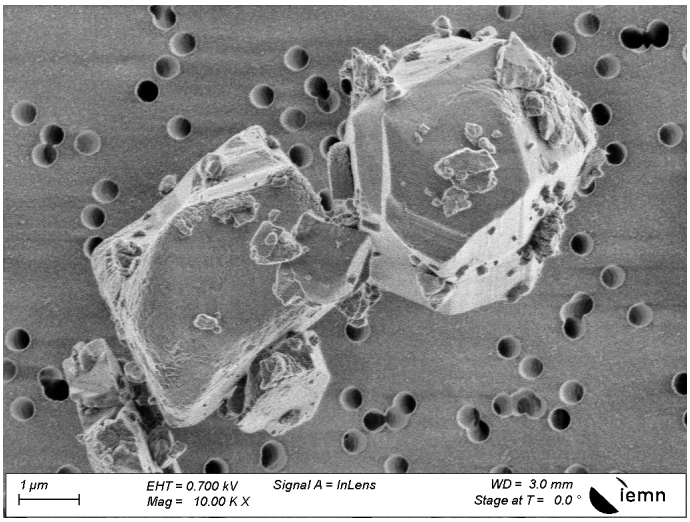


Figure 3.18: SE micrograph of resuspended and collected calcite particles.

from electrostatic interactions during the particle collection process. To determine the exact cause, further experiments under controlled atmospheric conditions would be necessary to confirm the influence of humidity or electrostatic forces on the aggregation behavior.

The average particle diameter is measured at 1.76 µm, with sizes ranging from 0.30 µm to 5.43 µm. The aspect ratio of the particles, averaging 1.53 with a standard deviation of 0.30, suggests a relatively uniform shape distribution across the sample. The relatively low variance in the aspect ratio indicates that while the particles have slightly elongated forms, their shapes remain fairly consistent.

#### 3.4.2.2 Pellet measurement

The optical response of a pellet containing 10 mg of calcite mixed with 140 mg of docosane matrix revealed a broad extinction band around 3 THz. A Lorentz oscillator fit showed that this band consists of two distinct peaks at 2.84 THz and 3.49 THz.

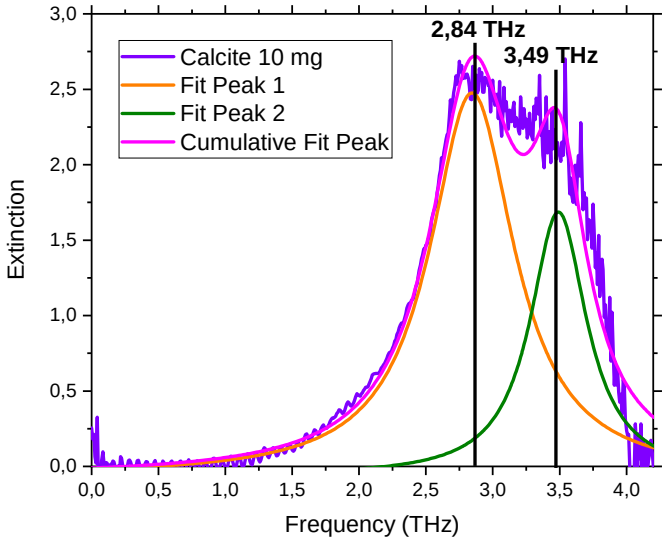


Figure 3.19: Extinction of 10 mg calcite diluted in 140 mg docosane in the pelletized form. The experimental data were fitted with the Lorentz oscillator model. Pelletized calcite exhibits two peaks at 2.84 and 3.49 THz.

These peaks correspond to phonon modes, which are intrinsic vibrational states of the calcite crystal structure. The calcite crystal lattice has vibrational modes due to the stretching and bending of the carbonate ions ($CO_3^{2-}$) and the movement of calcium ions relative to the carbonate groups. Slight variations in the calcite particle size and distribution in the matrix, lead to different local environments and a spread in the phonon resonance frequencies and explain the broad nature of the extinction band. The peak at 2.84 THz likely corresponds to a transverse

optical (TO) phonon mode, while the peak at 3.49 THz could be linked to another optical phonon mode and will be discussed during Chapter 4.

The phonon modes observed at 2.84 THz and 3.49 THz align with previous spectroscopic studies of calcite, which have reported similar vibrational frequencies associated with phonon resonances ( [132]). The precise positioning of these peaks can offer valuable insights into structural changes or strain effects within the calcite crystals, as even small shifts in phonon frequencies may reflect variations in crystal quality or external factors like temperature and pressure. Notably, the pressure applied during the pelletizing process can distort the crystal structure, which may influence the phonon response. To minimize such distortions, we limit the applied pressure to no more than 5 tons during pelletization [133].

#### 3.4.2.3 Aerosol measurement

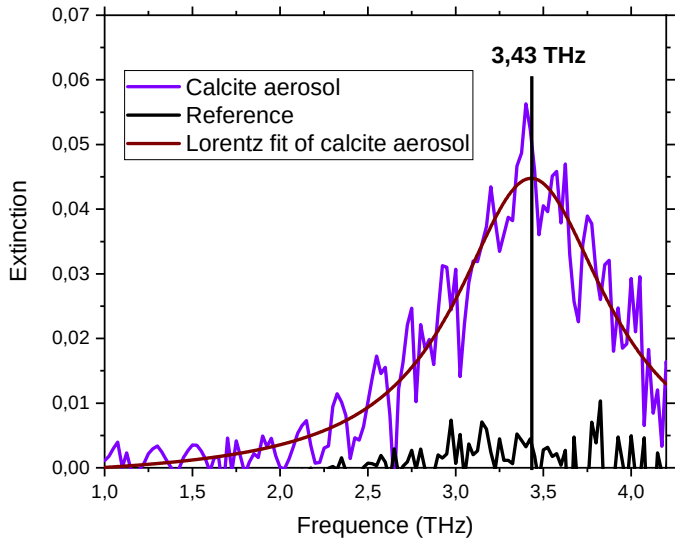


Figure 3.20: Extinction for calcite aerosol for 10400 particles/cm$^3$. The lorentz oscillator peak shows a peak maximum at 3.43 THz.

The extinction spectrum of calcite particles resuspended in a nitrogen ($N_2$) carrier gas, measured at a concentration of 10,400 particles/cm$^3$ i.e. 64 mg/m$^3$ revealed a dominant extinction band at 3.43 THz (Figure 3.20). This represents a shift from the peaks observed in pelletized samples, likely due to the smaller size of resuspended particles compared to those in pelletized or deposited forms, which significantly influences the THz response. In pelletized calcite samples, particles are densely packed, resulting in compression and potential structural modifications that shift the phonon modes. By contrast, resuspended particles experience much less mechanical stress, which may explain the difference in the extinction peaks. This highlights the importance of particle morphology and sam-

ple state (compressed versus free-flowing) when interpreting THz spectra across different experimental setups.

The size distribution of resuspended calcite particles, as shown in Figure 3.21, exhibits three distinct modes at 0.31 µm, 0.45 µm, and 1.49 µm. This multi-modal distribution is somewhat unusual for polydisperse aerosols and has been thoroughly analyzed.

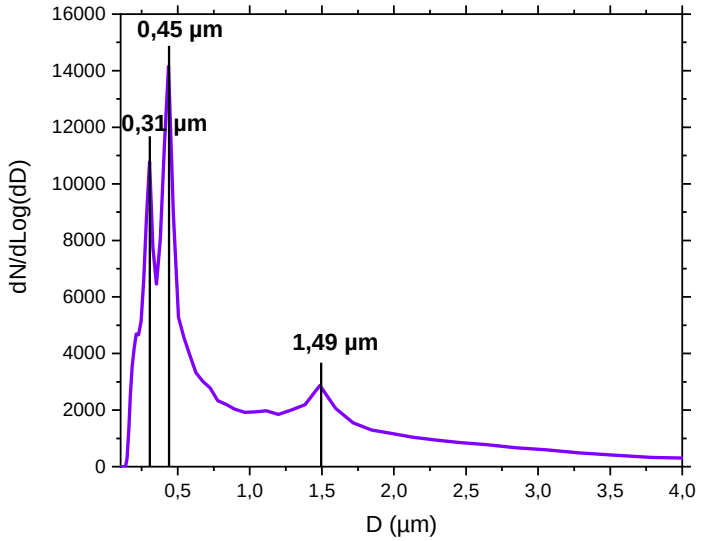


Figure 3.21: Corresponding size distribution of the resuspended calcite particles. The size distribution shows three main modes at 0.31, 0.45 and 1.49 µm.

When comparing these results with SEM-EDX data, which showed an average particle diameter of 1.77 µm with a standard deviation of 1.16 µm, we initially believed that the larger particle sizes in SEM-EDX were due to differences in resuspension methods. SEM-EDX employed the initial suspension setup, while the aerosol measurements used the RBG, leading to the hypothesis that the RBG method might generate smaller, more uniform particles, while the initial suspension setup could result in larger aggregates.

However, subsequent tests on additional samples demonstrated that this assumption was incorrect. The observed variation in particle sizes between SEM-EDX and PROMOLED is not directly linked to the resuspension method. Instead, the most likely explanation is the rhombohedral shape of calcite particles. This geometry significantly influences how the particles interact with light, creating complex scattering effects that account for the observed size distribution and discrepancies between different measurement techniques.

In conclusion, the rhombohedral shape of calcite particles plays a crucial role in their optical response and size distribution, and is the key factor behind the distinct modes seen in these size measurements. Differences in particle size data

between SEM-EDX and PROMOLED are not due to resuspension techniques but rather the inherent geometry of the calcite particles.

**Sensibility of the set-up to calcite particles** The sensitivity of the aerosol setup to varying concentrations of resuspended calcite particles was evaluated across a range from 3 mg/m$^3$ to 64 mg/m$^3$.

As illustrated in Figure 3.22, the extinction spectra are clearly distinguishable at concentrations of 10 mg/m$^3$ and above. However, differentiating between concentrations of 10, 5, and 3 mg/m$^3$ proves challenging, indicating that 10 mg/m$^3$ may be the current detection limit of the setup. The ability to distinguish lower concentrations may improve in the future with the use of a multipass cell. Despite these limitations, the setup remains capable of detecting calcite aerosol concentrations similar to those encountered during significant dust storms. For example, during a major dust storm event in Beijing in 2002, total suspended particle concentrations reached 12 mg/m$^3$ [134].

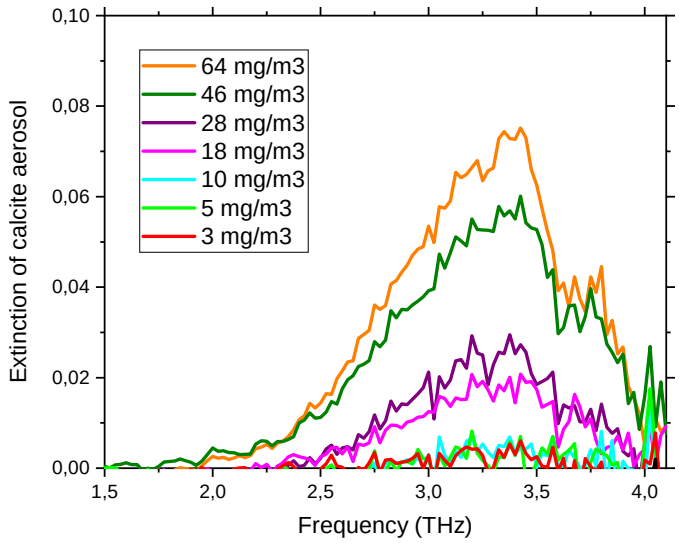


Figure 3.22: Extinction of calcite aerosol at different concentrations (64 mg/m$^3$, 46 mg/m$^3$, 28 mg/m$^3$, 18 mg/m$^3$, 10 mg/m$^3$, 5 mg/m$^3$ and 3 mg/m$^3$).

Figure 3.23 demonstrates the proportional relationship between particle volume concentration and extinction at the peak of the band (3.43 THz). This relationship underscores the linearity of the system's response to variations in particle concentration, confirming the reliability of the setup for quantifying calcite aerosol levels.

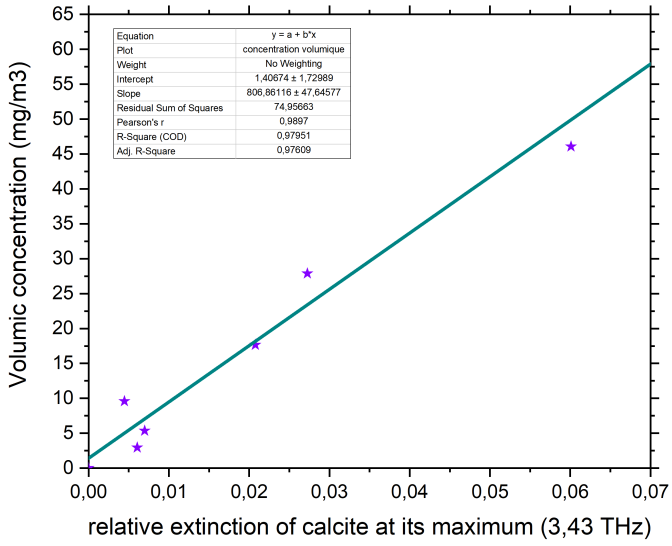


Figure 3.23: Proportionality betwwen the volume concentration and the extinction of resuspended calcite particles at the maximum of the band (3.43 THz).

#### 3.4.2.4 Effective complex refractive index extraction

Calcite is well-known for its strong birefringence, exhibiting different refractive indices for light polarized in various directions. However, this characteristic is not a concern in our study since the calcite particles are randomly oriented, whether resuspended in the aerosol or compacted into a pellet form.

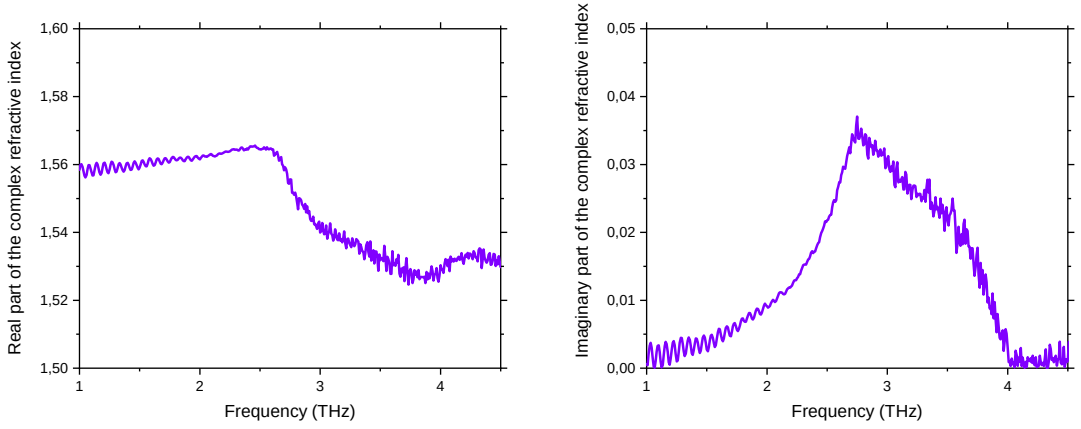


(a) (b)

Figure 3.24: The retrieved and fitted real (a) and imaginary (b) parts of the effective CRI of pelletized calcite particles.

The effective CRI of calcite pellet and aerosol was determined using the Fit@TDS algorithm. For the pelletized calcite sample with 10 mg calcite, the retrieved real

and imaginary parts of the CRI are depicted in Figure 3.24. The Fit@TDS model fit yielded an effective permittivity ($\varepsilon$) of 2.068, with a pellet thickness of 1.911 mm. Notably, the resulting spectral shape is characteristic of polaritonic modes, which will be explored in greater detail in Chapter 4.

For resuspended calcite particles, the retrieved and fitted real and imaginary parts of the CRI are illustrated in figure 3.25. The results align closely with extinction measurements, further validating the characterization of the aerosol. For the fit, the frequency mode was 3.26 THz with a linewidth of 0.80 THz.

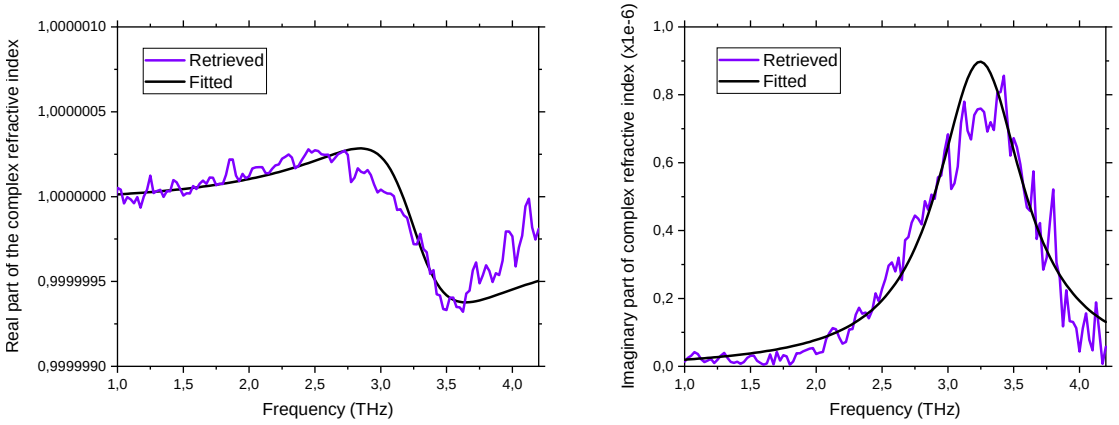


(a) (b)

Figure 3.25: The retrieved and fitted real (a) and imaginary (b) parts of the CRI of resuspended calcite particles in nitrogen flow at atmospheric pressure.

However, the real part of the CRI dips below 1, which does not reflect physical reality. This discrepancy arises from a temporal delay that, while corrected with Fit@TDS, has not been consistently adjusted across different samples. Efforts are currently underway to address this issue and refine the process for future measurements.

To ensure the validity of our findings, we also calculated the analytical error associated with the imaginary part of the refractive index. This was done to demonstrate that the observed response is genuinely due to the resuspended particles rather than being coincidental. Figure 3.26 compares the analytically calculated error, as outlined in Chapter 2, with the error bars provided by the Fit@TDS algorithm. The close agreement between these two values confirms that the retrieved refractive index is distinguishable from the baseline. This comparison underscores the robustness of the Fit@TDS approach, illustrating that the numerically derived results align with the analytical methodology.

In conclusion, the optical response of calcite particles around 3 THz is significant, as calcite constitutes approximately 30% of the particles found in Gobi dust.

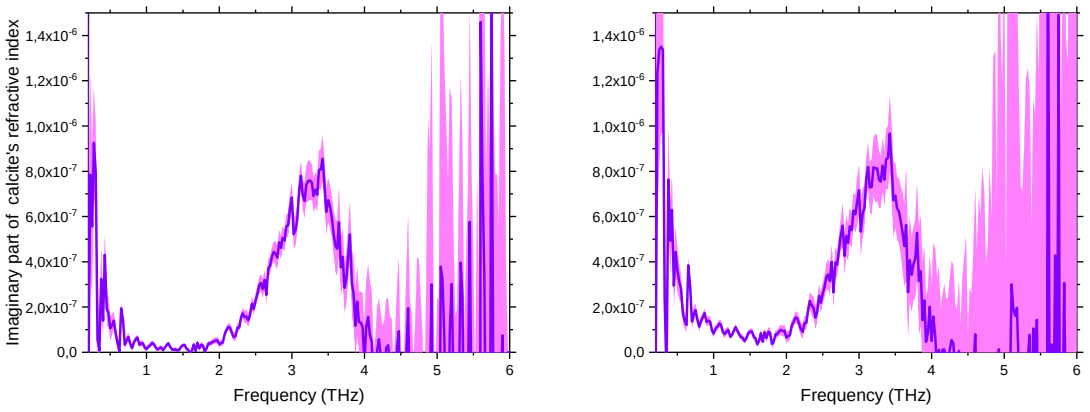


Figure 3.26: Error bars calculated by Fit@TDS algorithm (a) and analytical error (b) for imaginary part of effective CRI of calcite particles resuspended in nitrogen.

This suggests that the optical response attributed to calcite could potentially fill the spectral region left vacant by illite around 3 THz. Therefore, the interactions and contributions of calcite, alongside other mineral constituents, are crucial for a comprehensive understanding of the optical characteristics of Gobi dust.

### 3.4.3 Quartz

#### 3.4.3.1 Elementary composition and morphology

Quartz is a crystalline mineral composed primarily of silicon and oxygen, classified within the silicate group. It ranks as the second most abundant mineral in the Earth's crust, following the feldspar family. The quartz utilized in this study is a synthetic sample characterized by a homogeneous and pure chemical composition. Due to its high purity, automated elemental analysis was not performed; instead, hand-selected particles were subjected to analysis for verification. EDX spectra were recorded for these particles, revealing a prominent peak corresponding to silicon (Si), which is sufficient for the chemical identification of quartz, as shown in Figure 3.27. It is important to note that oxygen was excluded from the analysis. To enhance image resolution and magnification during microscopy, the quartz particles were coated with chromium (Cr).

At room temperature, quartz crystallizes in the trigonal crystal system, typically forming doubly terminated crystals that resemble pyramids. The micrographs reveal that quartz particles have smooth, non-rough surfaces, which is characteristic of their hardness. The particles vary in size, with larger particles often forming clusters surrounded by smaller particles, as illustrated in Figure 3.28.

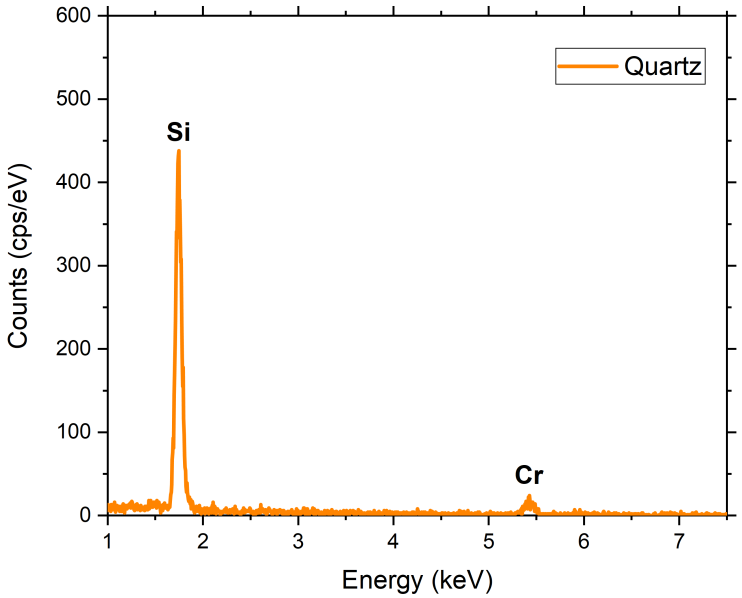


Figure 3.27: EDX spectrum of resuspended quartz particles that were collected on a polycarbonate filter with 0.2 µm pores. C and O are excluded from the analysis. Particles were coated with Cr.

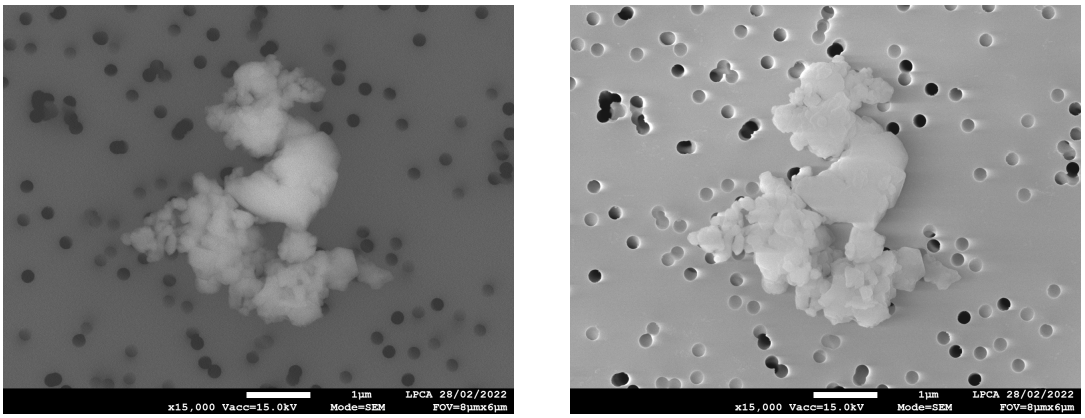


Figure 3.28: BSE (a) and SE (b) micrographs of resuspended and collected quartz particles.

#### 3.4.3.2 Pellet measurement

Quartz, characterized as a trigonal uniaxial crystal, exhibits birefringence, which refers to its ability to have different refractive indices depending on the direction of light polarization. In the ordinary spectrum, the optical phonon resonance of quartz occurs at approximately 3.855 ± 0.005 THz [135].

In the pelletized state, the phonon resonance is observed to be weak due to the random orientation of the particles, which means that neither the ordinary nor the extraordinary optical axes are preferentially aligned. Despite this lack of alignment, a broad absorption band can be detected beneath the 3.9 THz phonon

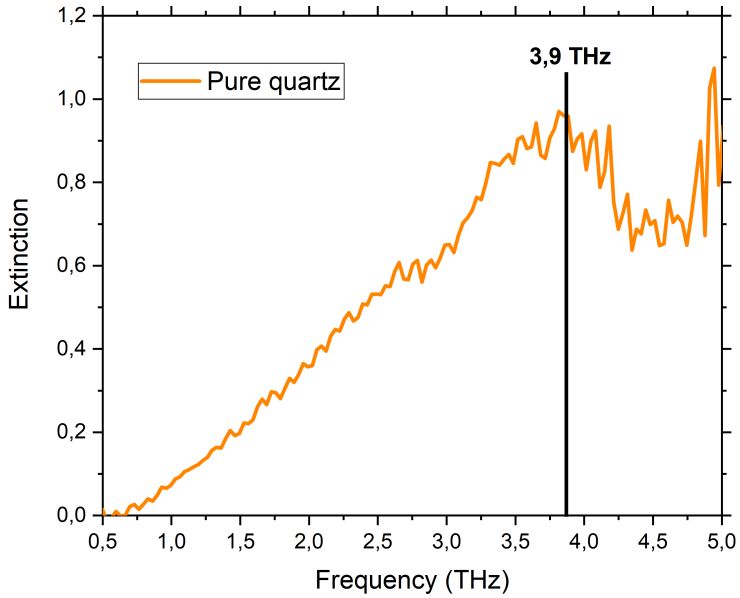


Figure 3.29: Pelletized pure quartz particles extinction in the THz range, showing the 3.9 THz phonon. 1000 averages.

resonance (Figure 3.29). The absorption and scattering of quartz are known to increase with frequency, likely due to a strong phonon mode present at 7.95 THz [136]. Another contributing factor to the broad absorption band may be the partial amorphization of the particles, resulting from the pressure applied during the pelletization process.

Although quartz was also resuspended for further analysis, the response was too weak to detect any meaningful signal. While the weak response of resuspended quartz in the THz range highlights the challenges of detecting certain materials in this state, it also opens avenues for exploring the effects of processing conditions and material properties on optical performance.

Despite quartz constituting approximately 10% of the particles found in Gobi dust, its weak optical response suggests that it is unlikely to contribute significantly to the overall optical behavior of Gobi particles.

### 3.4.4 Various feldspars and minerals

Key minerals identified in dust storm particles from the Gobi Desert include clays including various feldspars and minerals, which are prevalent in arid regions. Various feldspars and minerals together comprise nearly half of the dust composition in the Gobi Desert [137].

#### 3.4.4.1 Potassium Feldspar series : microcline

Dust particles are primarily composed of elements such as Si, Al, Fe, Mg, K, Ca, Na, Ti, and S. Within these particles, clay and feldspar minerals are predominantly composed of silicon (Si) and aluminum (Al). The Si/Al ratio serves as a key marker for classifying dust particles: when this ratio is approximately 3, the particles are typically identified as feldspars. Feldspars are further divided into potassium feldspar and plagioclase feldspar. Potassium feldspar ($K[AlSi_3O_8]$) is distinguished by its higher potassium content.

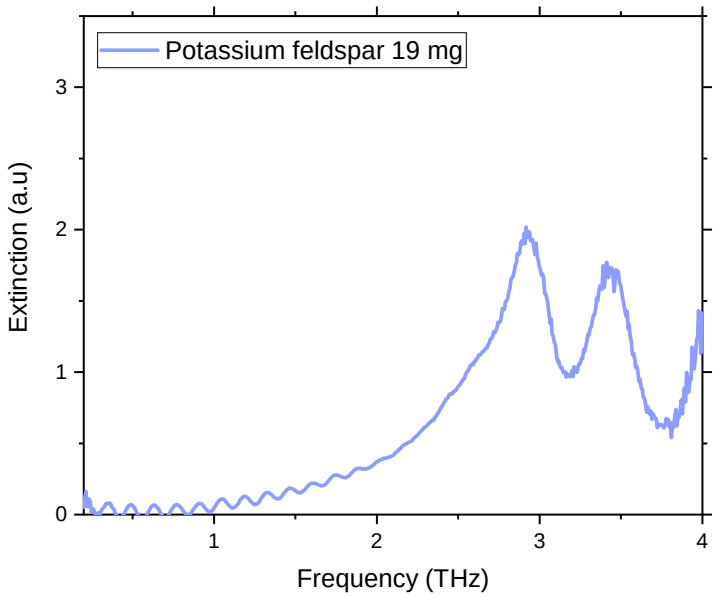


Figure 3.30: Pelletized potassium feldspar - microcline - (19 mg diluted into 81 mg of docosane) THz extinction.

The mass percentage of potassium (K) in Gobi dust is generally low, except a value of around 7.3% observed in the illite clusters, consistent with its chemical composition. However, while potassium feldspars are not a major component of Gobi Desert dust, studying them provides valuable insights into the role of feldspars in dust from other desert regions where these minerals are more abundant.

Potassium feldspars display characteristic absorption bands in both the infrared and terahertz (THz) spectral regions, particularly below 200 $cm^{-1}$ (6 THz). For example, sanidine, a less-ordered polymorph, shows broad absorption bands around 154 $cm^{-1}$ (4.6 THz) and 114 $cm^{-1}$ (3.4 THz). In contrast, microcline, a more ordered structure, exhibits a stronger band at 4.6 THz, with the band at 3.4 THz splitting into two sharper peaks due to its higher degree of crystallographic order. These spectral features are linked to K-O vibrations, and the difference in band splitting and intensity between sanidine and microcline highlights the role

of structural ordering in shaping the optical properties of these minerals [138]. The splitting of the 3.4 THz band in microcline and the emergence of a stronger band at 4.6 THz are shown in figure 3.30, which shows the THz extinction spectrum for a pellet containing 19 mg of microcline diluted in docosane, resulting in a total mass of 100 mg.

#### 3.4.4.2 Plagioclase feldspars series : soda and anorthic feldspars ( 4.6% of Gobi Desert particles)

Plagioclase feldspar, in contrast to potassium feldspar, contains higher amounts of sodium (Na) or calcium (Ca), commonly appearing in the forms $Na[AlSi_3O_8]$ (albite) or $Ca[Al_2Si_2O_8]$ (anorthite).

The mass percentage of sodium (Na) in Gobi Desert particles is relatively low, ranging from 0 to 1.2% in various clusters, suggesting that soda feldspars are not abundant in this region. However, one of the clusters, composed of aluminosilicates rich in calcium, constitutes 4.6% (cluster 5) of the Gobi Desert dust particles. This cluster likely corresponds to the calcium-rich form of plagioclase feldspar, specifically anorthite.

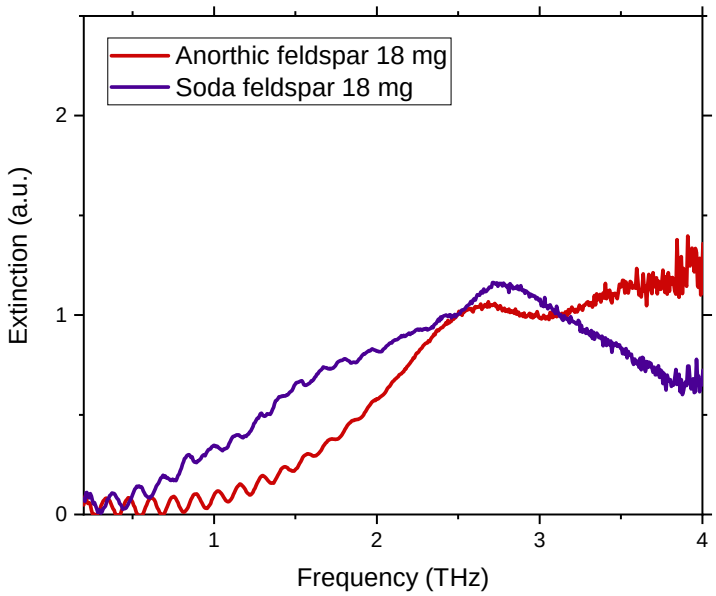


Figure 3.31: Pelletized anorthic feldspar (18 mg diluted into 82 mg of docosane - red) and soda feldspar (18 mg diluted into 82 mg of docosane - purple) THz extinction.

Within the plagioclase feldspar series, which spans from albite (sodium-rich) to anorthite (calcium-rich), characteristic vibrational bands provide insights into the mineral's composition. Albite exhibits a strong spectral band at 187 $cm^{-1}$ (5.6 THz), which shifts to higher frequencies as the calcium content increases in the plagioclase series. This shift is attributed to Na-O vibrations in albite and Ca-O

vibrations in anorthite. As calcium, being nearly twice the size of sodium, substitutes for sodium in the $(Si, Al)O_4$ tetrahedra, it causes progressive distortions in the crystal structure, further affecting the vibrational properties.

In addition to the 187 $cm^{-1}$ (5.6 THz) band, albite also shows a notable band around 90 $cm^{-1}$ (2.7 THz), while anorthite exhibits a strong band near 150 $cm^{-1}$ (4.5 THz). These spectral features help differentiate between the sodium and calcium poles of plagioclase feldspar. In nature, pure albite and anorthite are less common, and most plagioclase feldspars exist as intermediate mixtures, with varying sodium and calcium content. The optical response captured here helps characterize the end-members of plagioclase feldspar.

As illustrated in Figure 3.31, the spectral response of both sodium-rich (albite) and calcium-rich (anorthite) feldspars can be observed. In this case, 18 mg of albite and anorthite were each diluted into 82 mg of docosane and pelletized. A peak around 2.7 THz is clearly visible for albite, while anorthite shows a more gradual increase in extinction up to a peak near 4.5 THz, highlighting the differences in their spectral characteristics.

Given that Cluster 5 of the Gobi dust particles showed only 0.1% sodium by mass, it is likely that these particles correspond more closely to the calcium-rich, anorthitic end of the plagioclase feldspar series.

#### 3.4.4.3 Hematite

Hematite, an iron oxide mineral, constitutes approximately 1.7% of the total composition of Gobi Desert dust. Represented chemically as $Fe_2O_3$, hematite plays a crucial role in the optical properties of dust aerosols due to its strong absorption of sunlight, particularly in the visible and near-infrared regions. This absorption gives hematite its distinctive reddish-brown color, which contributes to the overall coloration observed during dust storm events.

The pelletized hematite sample depicted in figure 3.32, comprising 15 mg of hematite diluted into 85 mg of docosane, illustrates its characteristic extinction behavior in the THz domain. Unlike many minerals, hematite exhibits a broad absorption band rather than distinct peaks.

Notably, the majority of absorption peaks for hematite seem to appear at approximately 300 $cm^{-1}$, which corresponds to around 9 THz. However, this sample has not been extensively studied beyond 200 $cm^{-1}$ (approximately 6 THz) [139].

Due to its iron content, hematite-rich dust particles have implications beyond their optical properties. When transported over long distances, such as from the Gobi Desert to other regions, they can deposit iron-rich material that may fertilize ecosystems, especially marine environments. This is crucial because iron is a limiting nutrient for phytoplankton growth in certain oceanic regions. The presence of hematite in dust can, therefore, indirectly influence carbon cycling and biological productivity. Thus, the role of hematite in Gobi Desert dust extends far

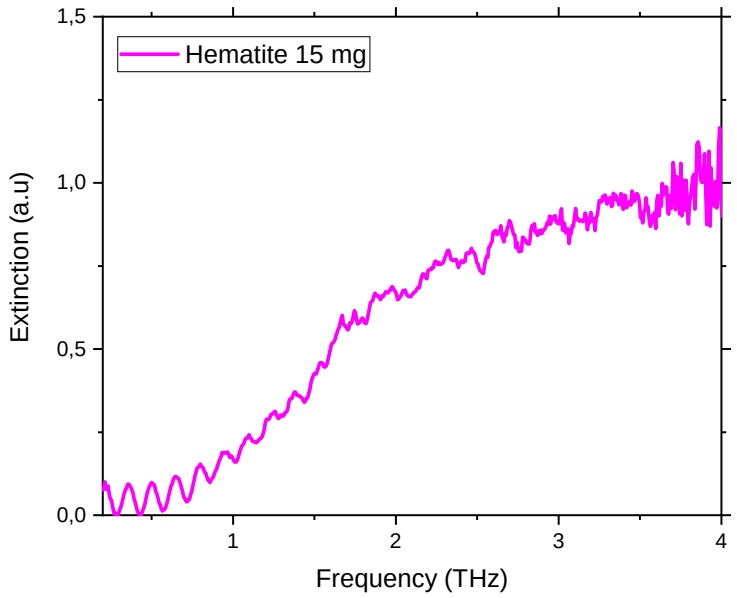


Figure 3.32: Pelletized hematite (15 mg diluted into 85 mg of docosane) THz extinction.

beyond its optical characteristics, with profound effects on radiative balance and ecosystem health.

### 3.4.5 Kaolinite : in Sahara and other deserts

In addition to the components found in Gobi Desert dust, it is important to consider other minerals that are typically absent from this region but prevalent in other deserts, such as kaolinite, which is commonly encountered in the Sahara Desert and is often associated with regions that experience significant weathering and erosion processes.

#### 3.4.5.1 Elementary composition and morphology

The chemical formula of the purchased kaolinite is $Al_2O_3$ $2SiO_2 2H_2O$, which allows for its identification through an equivalent intensity peaks for aluminum (Al) and silicon (Si) in EDX spectra. A total of 301 particles were analyzed; however, 33 were excluded from the analysis due to movement during examination or lack of detectable signal. The remaining 268 particles were classified into 11 distinct clusters. Notably, pure kaolinite constitutes 74.25% of the analyzed particles.

The composition of the remaining particles includes 5.97% kaolinite with trace amounts of iron (Fe), 5.97% potassium-rich aluminosilicate, 4.48% aluminum phosphate with minor silicon, and 2.61% quartz, among others. Additionally, four clusters represented impurities, such as iron oxide or titanium-containing aluminosilicate, each comprising less than 1% of the total particles. The EDX spectrum

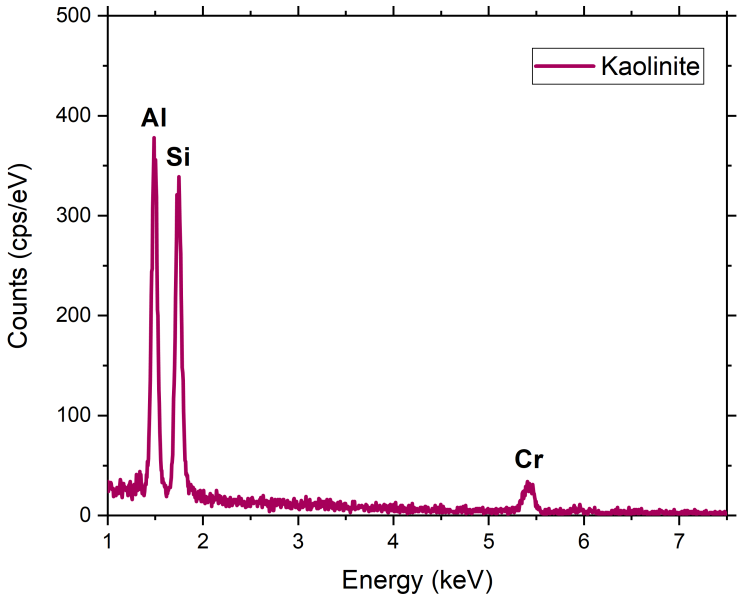


Figure 3.33: EDX spectrum of resuspended and collected kaolinite particles that were collected on a polycarbonate filter with 0.2 µm pores. This spectrum corresponds to the kaolinite cluster that accounts for 74.25% of the analyzed 268 particles. C and O are excluded from the analysis. Particles were coated with Cr.

corresponding to the kaolinite cluster, which represents 74.25% of the analyzed particles, is illustrated in Figure 3.33.

Kaolinite is classified as a hydrated aluminosilicate consisting of alternating 1:1 layers. Each layer comprises a tetrahedral sheet centered on $Si^{4+}$ and an octahedral sheet centered on $Al^{3+}$, arranged alternately. These successive layers are interconnected by hydrogen bonds, which significantly enhance the cohesive energy between them [140].

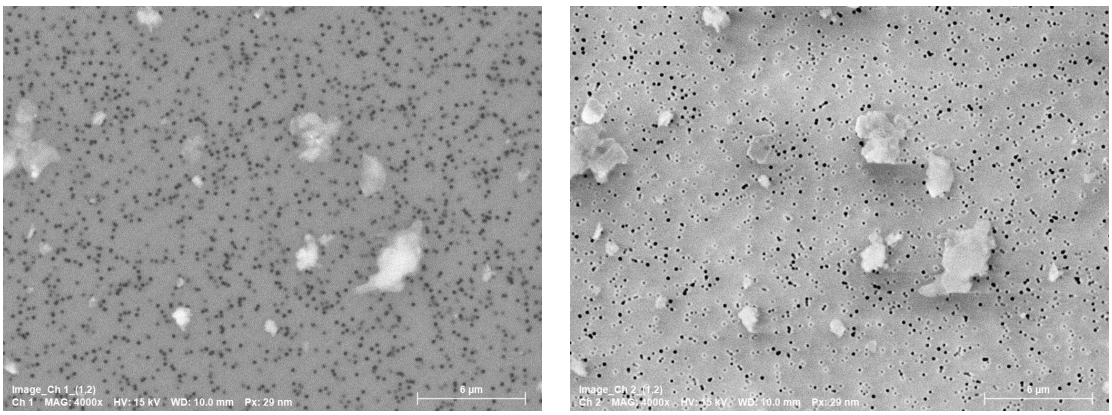

Figure 3.34: BSE (a) and SE (b) micrographs of kaolinite particles.

BSE and SE micrographs of kaolinite particles seem to reveal the characteristic

layered structure typical of clay minerals, as shown in figure 3.34. The average diameter of the analyzed kaolinite particles is 0.76 µm, with a standard deviation of 0.70 µm. The average aspect ratio of the particles is 1.75, indicating a tendency for them to be elongated in shape.

#### 3.4.5.2 Pellet measurement

Kaolinite particles were first processed into pellets, with 20 mg of kaolinite mixed into docosane powder for a total mass of 200 mg. The measured extinction spectrum, presented in Figure 3.35, shows two prominent peaks, one at 2.77 THz and another at 3.66 THz, corresponding to oscillations within the deformed $Si_2O_5$ layer. According to the literature, only a single peak at 3.6 THz is typically observed [141], raising questions about the origins of the additional feature in our measurements.

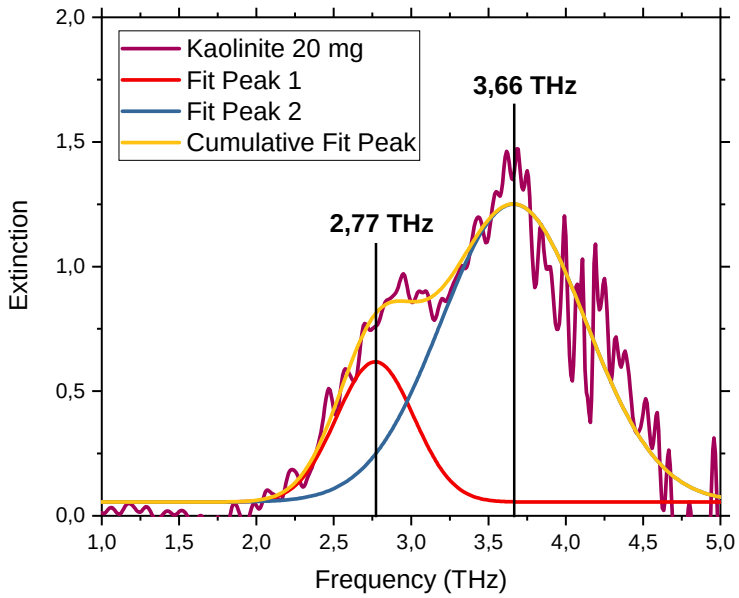


Figure 3.35: Pelletized kaolinite THz extinction and its lorentz cumulative fit.

.

The peak at 2.77 THz appears as a shoulder and may have been overlooked in prior studies due to insufficient spectral resolution. Our experimental setup, with potentially higher resolution (8 GHz for pellet measurements), could have revealed this finer structure that was not previously detectable. The presence of the 2.77 THz peak might be attributed to the broad particle size distribution in the pellet, where larger particles could induce Mie resonances, thus giving rise to this additional spectral feature. The deviation from the single peak reported at 3.6 THz in previous studies possibly indicates that factors like lower resolution,

different pellet preparation, or varying packing densities in those studies might have masked the finer spectral details we observed.

The two peaks were further analyzed using a Lorentz oscillator model, which provided an excellent fit to the measured extinction spectrum. The Lorentzian fit confirms that the observed modes can be well described by resonant behavior, characteristic of the vibrational modes of the kaolinite lattice. This analysis not only supports the hypothesis of multiple resonances but also emphasizes the potential complexity of kaolinite's THz response, which may be richer than previously reported.

#### 3.4.5.3 Aerosol measurement

The extinction spectrum of resuspended kaolinite exhibits a single, broad absorption band centered around 3.6 THz, further characterized by a Lorentzian fit (Figure 3.36). However, the spectrum is noticeably disrupted by water vapor absorption lines, likely due to the residual moisture content in the kaolinite, even after steaming. The purchased kaolinite sample is naturally hydrated, and it is hypothesized that mechanical collisions during the resuspension process could have released water trapped within the kaolinite structure in gaseous form. This released water vapor could obscure certain spectral features, such as the 2.77 THz peak observed in the pelletized sample that possibly masked by overlapping water vapor absorption bands in the aerosol measurement.

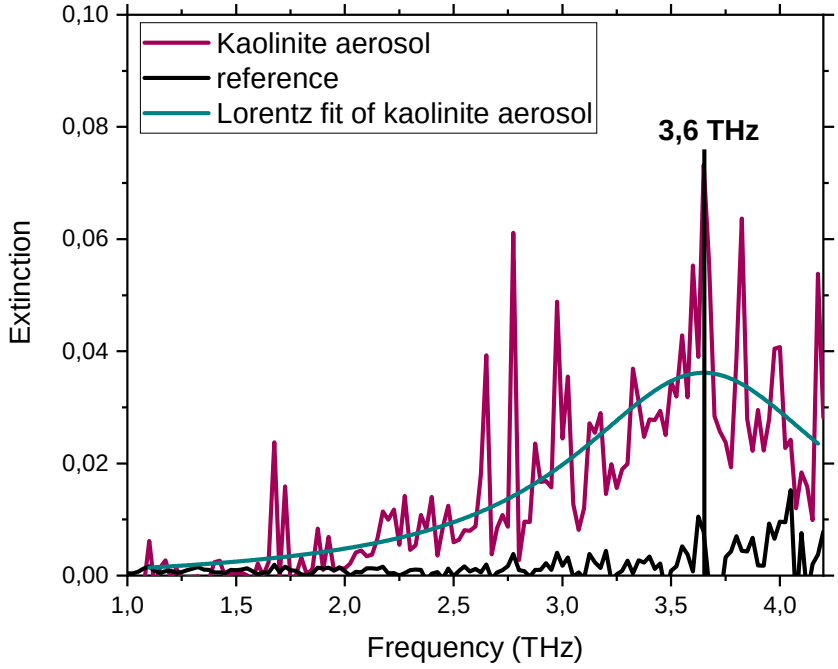


Figure 3.36: Resuspended kaolinite particles THz extinction for 5000 particles.cm$^{-3}$.

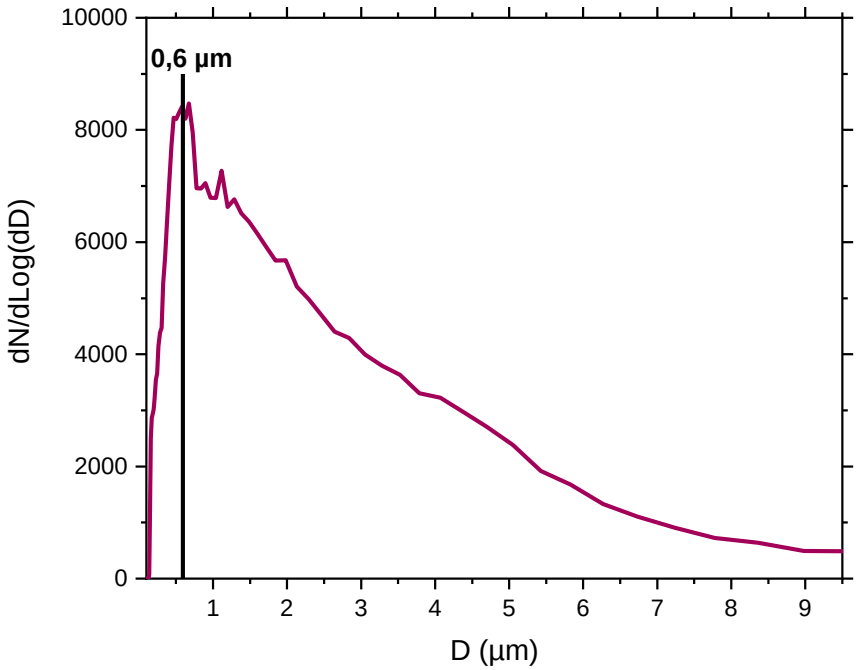


Figure 3.37: Size distribution of the resuspended kaolinite particles

The particle size distribution shows that the main mode is at 0.6 µm, which is close to the 0.76 µm stated by the automatic analysis with the SEM-EDX. The particle sizes appear well dispersed, with a majority of particles less than 1 µm. However, the analyzed sample also contains larger particles up to 10 µm in diameter. This dispersion of sizes is also consistent with the standard deviation of the mean diameter given by the SEM-EDX which was of the order of the mean diameter.

The observed differences between the pelletized and aerosolized kaolinite spectra suggest that the hydration level (in addition to size distribution) plays a significant role in shaping the measured optical properties. Future studies could focus on reducing water vapor interference, either by further drying the samples or by conducting the measurements in a low-humidity environment to better isolate the intrinsic absorption features of kaolinite. Alternatively, subtracting the water signal from the kaolinite spectrum via signal processing techniques would help to isolate the kaolinite's true spectral features [142]. Moreover, a more detailed exploration of particle size effects on the extinction spectrum, possibly through size-selective sampling or theoretical modeling, could provide deeper insights into the contribution of different particle populations to the overall optical response.

#### 3.4.5.4 Effective complex refractive index extraction

The real and imaginary components of the extracted complex refractive index (CRI) for pelletized kaolinite particles are shown in Figure 3.38. The fitted permittivity of the material is determined to be 2.46, and the thickness of the pellet was fitted to be approximately 1.78 mm.

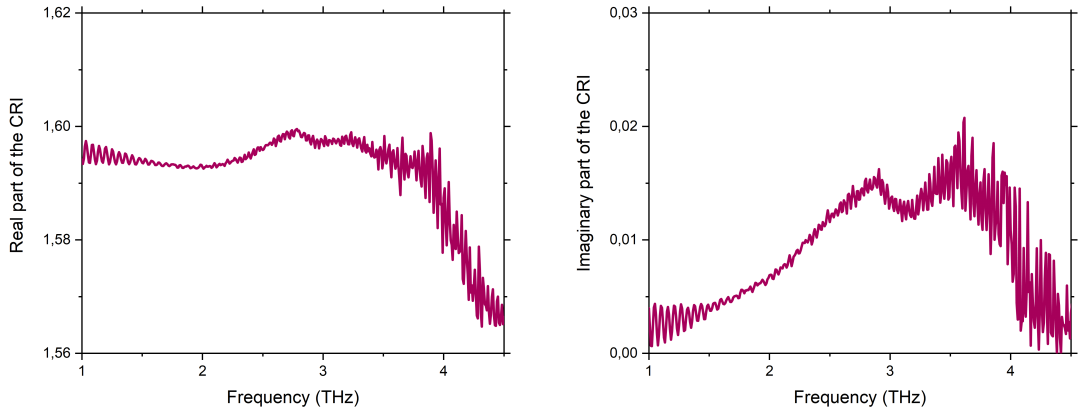


(a) (b)

Figure 3.38: The retrieved and fitted real (a) and imaginary (b) parts of the CRI of pelletized kaolinite particles.

The characteristic peaks at 2.77 THz and 3.66 THz are clearly identifiable in the imaginary part of the CRI (Figure 3.38b), which corresponds to the material's absorption behavior. These two resonances are also reflected in the real part of the index (Figure 3.38a). At the high frequencies, there is a noticeable drop in both the real and imaginary parts of the CRI, indicating the transitioning out of its resonant behavior. As the system moves beyond the resonant frequencies, the material absorbs less energy and becomes less effective at refracting light, which explains the observed decrease.

The extraction of the CRI for resuspended kaolinite particles is currently challenging due to the significant presence of water vapor in the THz measurements.

The CRI extraction in such complex environments, especially in the presence of both Mie scattering and overlapping spectral features from water vapor, underscores the importance of improving experimental setups and using refined data analysis techniques. A multi-pass cell design or further drying of the sample could also enhance the sensitivity and accuracy of future measurements.

## 3.5 Conclusion

Our findings indicate that the optical response of minerals and feldspars in the THz domain remains inadequately understood, both experimentally and computationally, as only a limited number of studies have investigated this frequency

range at sufficient resolution. The discrepancies observed in the optical responses highlight the urgent need for direct measurements on resuspended micro- and nanoparticles to effectively utilize these results for the remote sensing of atmospheric aerosols.

Most samples analyzed in this study are relatively uncharacterized in the far-infrared region, which complicates comparisons with existing literature. Nevertheless, we are confident in the reliability of our findings as we calculated the error bars for aerosol measurements, particularly for calcite in aerosol form, demonstrating that the analytical errors align with those obtained using our Fit@TDS algorithm. Additionally, we extended our analysis by plotting the proportionality between extinction and the concentration of resuspended particles. The various measurements displayed strong alignment and proportionality.

The sensitivity of our setup was assessed using calcite particles, revealing a detection limit of approximately 10 mg/m$^3$ for calcite. Notably, the resuspension of Gobi Desert particles was performed at a concentration of around 1.6 mg/m$^3$, well below the detection limit for calcite. This suggests that the detection limit is sample-dependent, and the capabilities of our setup may be better than initially assumed.

In a detailed compositional analysis, we determined that the Gobi Desert particle sample consisted of approximately 40.8% illite, 29.4% calcite, 9.1% quartz, and 20.7% various clays. Chemical characterizations also indicated a tendency for external mixing within the particles.Approximately 70% of the extinction observed for illite in pellet form explains nearly the entire THz extinction response of pelletized Gobi Desert particles for the same mass, with only a minor additional contribution around 3 THz. Unfortunately, we were unable to suspend illite for aerosol comparison due to supply limitations, which restricted our ability to assess its behavior in aerosol form. The remaining response around 3 THz is likely due to calcite, which constitutes about 30% of the Gobi particle composition. In summary, the THz response of Gobi Desert particles likely results from a combination of the dominant illite response, with a minor contribution from calcite. The lack of an observable response from quartz reinforces the idea that it does not play a significant role in the optical response of Gobi particles in the THz range, contrary to its behavior in the infrared (IR) range [143].

In the upcoming chapter, we will shift our focus to a detailed examination of calcite's optical response. This will be achieved through Finite-Difference Time-Domain (FDTD) simulations, Mie theory calculations, and the application of effective medium theories, such as Maxwell-Garnett theory. This comprehensive approach aims to deepen our understanding of calcite's behavior in the THz range and its implications for aerosol studies.

# Chapter 4

# Single-particle simulations and complex refractive index restitution methodology applied to calcite

## 4.1 Introduction

The experimental results presented in Chapter 3 highlight the critical need for simulations to enhance our understanding of THz-aerosol interactions at the single-particle level. To address this, we will utilize Finite Difference Time Domain (FDTD) simulations to explore the absorption and scattering cross sections as functions of particle radius, with a particular focus on materials such as quartz and calcite.

Our investigation will commence with a comparative analysis of quartz phonon and the phonon polariton of calcite. Following this, we will delve into the size-dependent effects on the phonon polariton of calcite. To validate the accuracy of our simulated results, we will compare them against a custom-developed Mie theory code and align them with experimental data [144].

In our analysis, we will calculate extinction using two distinct numerical approaches: one will incorporate the simulated extinction cross sections as inputs, while the other will employ a Mie theory code that computes extinction using Bessel functions.

This chapter will also provide a detailed overview of effective medium theories, including the Bruggeman and Maxwell-Garnett models, leading to our selection of the extended Maxwell-Garnett theory in conjunction with Mie theory (MGM) for a thorough analysis.

Finally, we will explore the potential implications of our findings on Earth's radiative balance, emphasizing their importance within the broader framework of atmospheric science and climate dynamics.

## 4.2 Finite difference time domain simulations

The Finite Difference Time Domain (FDTD) method, also known as the Yee method, is a widely used 3D full-wave electromagnetic solver ideal for modeling the behavior of nanophotonic devices, materials, and processes. FDTD is particularly advantageous for broadband simulations, as it computes the transmission, diffraction, reflection, scattering, interference, and absorption of light in a material over a broad frequency range. Its time-domain nature allows for the extraction of broadband results from a single simulation, functioning as a type of numerical THz-TDS. The automated Fourier transform enables efficient frequency analysis, enhancing the overall effectiveness of the approach. The simulations in this thesis were carried out using Ansys Lumerical software, which solves a modified form of Maxwell's coupled differential equations by iteratively alternating between the electric and magnetic fields at each spatial and temporal point in the simulation grid [145]. The method also incorporates Gauss's law, Faraday's law of induction, and Ampère's law to ensure physical accuracy.

FDTD is the preferred tool for simulating photonic designs such as photonic crystals, metamaterials, and plasmonic structures due to its ability to capture complex electromagnetic interactions. For instance, FDTD has been applied to study naturalistic broadband light interactions with micro- and nano-scale living organisms [146], as well as the optical properties of gold nanoparticles, investigating the impact of particle size and interparticle spacing on local electric fields and extinction properties [147].

### 4.2.1 Simulation set-up

In this work, the simulation volume was carefully constructed based on the principle of a Yee cell. The central element is a spherical particle with an assigned refractive index and radius, which is placed in the center of the simulation box.

Surrounding this sphere are the absorption analysis group, a Total Field Scattered Field (TFSF) light source, and the scattering analysis group (see Figure 4.1). The simulation volume was set to 100 $\mu m^3$, and the dimensions of the analysis groups were defined based on the particle radius, adapting dynamically as the radius changes.

For instance, the absorption analysis group varies in volume, ranging from 0.20 $\mu m^3$ for a particle radius of 0.1 µm to 50.20 $\mu m^3$ for a radius of 20.50 µm. Similarly, the TFSF light source spans from 0.24 $\mu m^3$ at a radius of 0.1 µm to 60.24 $\mu m^3$ at a radius of 20.50 µm. The scattering analysis group also adjusts accordingly, ranging from 0.28 $\mu m^3$ for a radius of 0.1 µm to 70.28 $\mu m^3$ for a radius of 20.50 µm. This careful calibration ensures accurate analysis of the particle's optical properties across different sizes.

The light source used in the simulations is a Total-Field Scattered-Field (TFSF) source, which is ideal for analyzing scattering in non-periodic structures illumi-

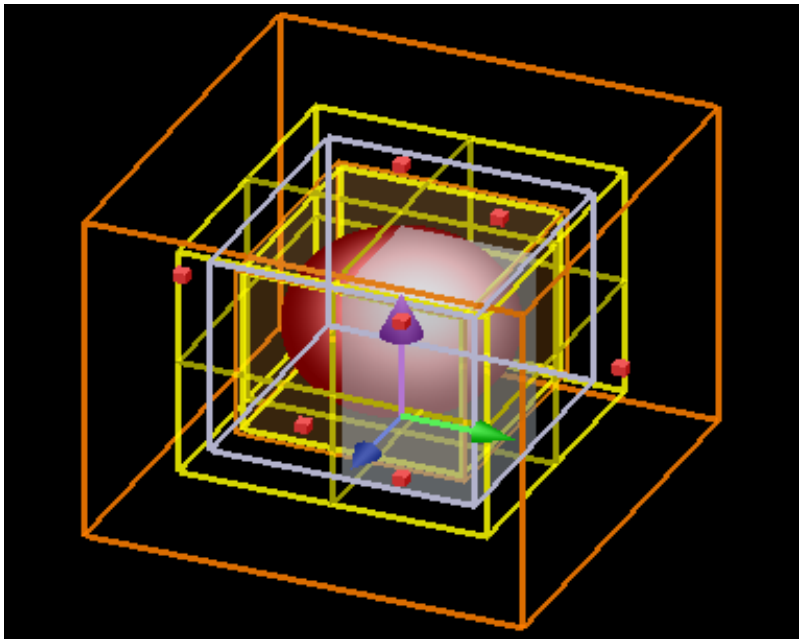

Figure 4.1: Perspective view of the Yee cell in the Ansys Lumerical FDTD platform. From outside to inside : Simulation volume, scattering analysis group, TSFSF source, absorption analysis group, material sphere.

nated by a plane wave. This source simplifies scattering analysis by separating the scattered field from the incident field, with the incident wave propagating along the z-axis. For these simulations, a broadband frequency range from 0.2 THz to 6.5 THz was specified, which aligns with the frequency range utilized in our experiments and measurements.

### 4.2.2 Grid meshing and boundary conditions

FDTD divides the simulation domain into a discrete grid (mesh), where the electromagnetic fields are computed at each time step. The mesh size plays a critical role in balancing simulation speed and accuracy. A finer mesh provides more accurate results but at the cost of longer computation times. For this study, the mesh size was set to the particle radius divided by 20, and a second mesh with an equivalent index of 6 was implemented to enhance precision. The equivalent index is used to determine the mesh spacing based on the refractive index of the materials in the simulation, with a higher index resulting in a finer mesh for improved accuracy in modeling light-matter interactions.

Boundary conditions are essential to avoid unwanted reflections and artifacts. Perfectly Matched Layer (PML) boundary conditions were applied to absorb outgoing waves and prevent reflections from the simulation boundaries, thereby ensuring the integrity of the results [148]. This technique involves smoothly transitioning between regions of different refractive indices, effectively minimizing reflections at the boundaries.

### 4.2.3 Material properties and refractive indices

The optical properties of the simulated materials, specifically quartz and calcite, are defined by their refractive indices. While Lumerical includes an extensive library of material indices, the refractive index data for quartz and calcite in this study were sourced from [149] and [150], respectively. These indices were fitted using the Lorentz oscillator model, which is commonly employed to describe the interaction between light and absorbing materials. To simulate particles in air, the refractive index of the surrounding medium is set to 1.

Quartz has characteristic phonon at 3.9 THz. However, its optical response in the THz range is notably weaker than that of calcite (chapter 3). This discrepancy raises an intriguing question: why does calcite exhibit a significantly stronger response at 3.6 THz, despite quartz's phononic activity at a similar frequency?

### 4.2.4 Analysis of simulation results

In the simulation setup, monitors are used to capture and record the electromagnetic fields in specific regions around the particle. The monitors in the scattering analysis group are positioned around the particle to detect the electromagnetic energy radiated away from the particle in all directions. For absorption, the monitors in the absorption analysis group are placed close to the particle to record the decrease in energy as the incident electromagnetic field interacts with the particle and is absorbed. These cross-sections were calculated by integrating the power across the monitors positioned in the scattering and absorption analysis groups.

The scattering cross-section was computed as:

$$\sigma_{scat} = \frac{P_{scat}(\omega)}{I_{incident}(\omega)} \tag{4.1}$$

Where $P_{scat}(\omega)$ and $I_{incident}(\omega)$ are respectively the total scattered power and the intensity of the incident source.

The absorption cross-section can be calculated according the following equation :

$$\sigma_{abs} = \frac{P_{abs}(\omega)}{I_{incident}(\omega)} \tag{4.2}$$

Where $P_{abs}(\omega)$ is the total power absorbed by the particle.

The scattered and absorbed power are expressed in $W$ and the intensity in $W/m^2$.

The simulations were validated by comparing the results with those obtained from a custom-developed Mie scattering code. Following this validation, we conducted parameter sweeps using 50 values for particle radius, ranging from 0.1 microns to 2.5 microns. This approach allowed us to systematically explore how variations in particle size influence the scattering and absorption cross sections.

### 4.2.5 Field visualizations and frequency domain analysis

The FDTD simulations provide valuable insights into the electric and magnetic field distributions around the particles. Field plots were generated for the x-normal profile, with frequency-domain field monitors capturing the local field enhancement. These monitors record the electric (Ex, Ey, Ez) and magnetic (Hx, Hy, Hz) field components, as well as the Poynting vector, over the spatial domain (figure 4.1).

By analyzing these field distributions, we gain a better understanding of the particle's interaction with the electromagnetic wave. For example, abrupt changes in color in the field plots indicate the edges of the TFSF source. Inside the source, the total field (incident + scattered) is visible, while only the scattered field is present outside. The absence of units in these visualizations is because the colors represent normalized or relative values, making it easier to visualize the field distributions without needing to know the exact values.

## 4.3 Phonon-polaritons in calcite

As discussed in Chapter 3, both quartz and calcite are major components of Gobi Desert dust, with quartz comprising around 9% and calcite nearly 30%. These compounds are crucial in studying atmospheric particles and their impact on the environment.

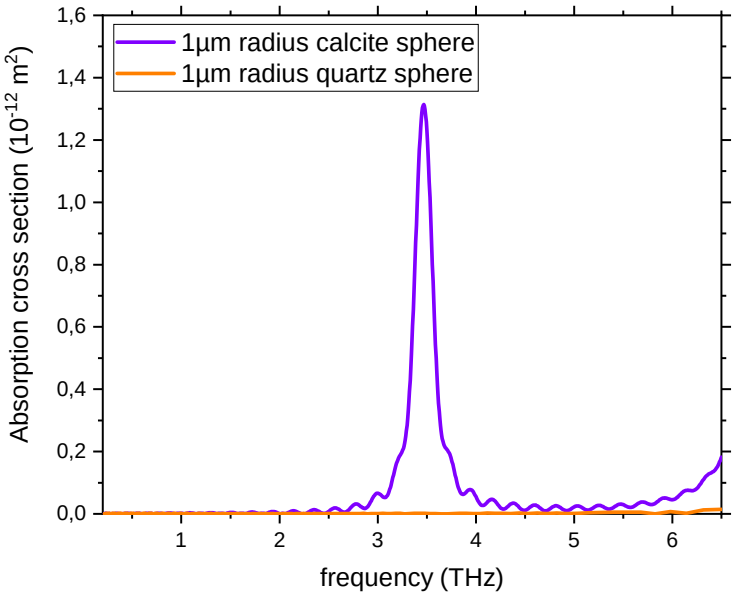


Figure 4.2: Absorption cross sections of 1 µm radius calcite sphere (purple) and 1 µm radius quartz sphere (orange).

A comparison of the optical response between a 100 mg pure quartz pellet and a calcite pellet diluted to 10 mg reveals that calcite's extinction is approximately 30 times stronger than that of quartz for the same mass. Interestingly, during resuspension of quartz particles using the aerosol setup, no significant response was observed, underscoring the need to focus on calcite's behavior. Consequently, the absorption and scattering properties of calcite and quartz were investigated at the single-particle scale, focusing on particles with a radius of 1 µm.

Figure 4.2 compares the absorption cross sections of a 1 µm calcite sphere and a 1 µm quartz sphere. The selected particle sizes align with those measured by the PROMOLED during resuspension, representing typical sizes of atmospheric aerosols. This comparison clearly illustrates the markedly lower optical response of quartz, with its phonon at 3.9 THz essentially vanishing when juxtaposed with calcite's much stronger phonon at 3.6 THz. The discrepancy in optical behavior is stark, highlighting the dominance of calcite in terms of both absorption and scattering cross sections.

### 4.3.1 Electric field plots and light-matter interaction

To gain deeper insights into the strength of phonon-polariton coupling in calcite compared to quartz, we analyzed the electric field distribution plots for both materials. In Figure 4.3, the electric field distribution for a 1 µm calcite particle at 3.6 THz displays a uniformly high intensity across the entire particle, represented in red. This strong uniformity signifies that the interaction between the THz beam and calcite is exceptionally robust, indicating effective light-matter coupling. The red regions throughout the figure illustrate the significant enhancement of the electric field, which is characteristic of calcite's pronounced phonon-polariton resonance at this frequency.

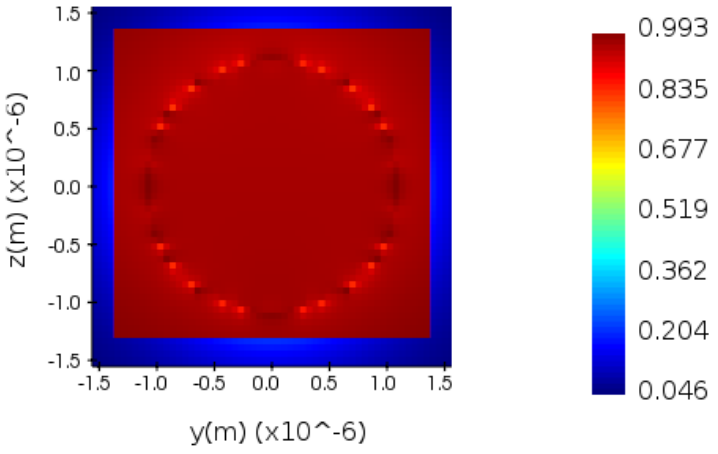


Figure 4.3: Electrical field distribution plots for calcite particle of 1 µm radius at 3.6 THz.

In contrast, Figure 4.4 depicts the electric field distribution for a 1 µm quartz particle at 3.9 THz. Here, while the spherical shape of the particle is clearly recognizable, the electric field distribution is markedly weaker compared to calcite. The lower intensity levels suggest that the interaction between the THz beam and quartz is limited, reinforcing the notion that quartz exhibits negligible phonon influence at this frequency. The absence of pronounced electric field enhancements indicates a weaker light-matter coupling, in line with the expected behavior of quartz's phonon modes.

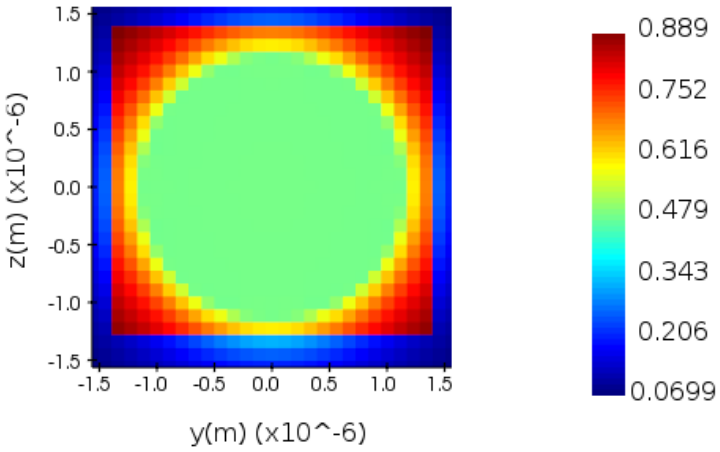


Figure 4.4: Electrical field distribution plots for quartz particle of 1 µm radius at 3.9 Thz.

Overall, the analysis of these figures highlights the distinct differences in phonon-polariton coupling between calcite and quartz. The intense electric field response in calcite contrasts with the relatively lower intensity observed in quartz, underscoring the different light-matter interaction behaviors exhibited by the two materials.

### 4.3.2 Dispersion relation and phonon-polariton excitation

In addition to the electric field distribution plots, the resonance characteristics of calcite and quartz can be further analyzed by examining their respective permittivity and dispersion curves. A key indicator of a material's interaction with an incident electromagnetic field is its dispersion relation, which characterizes how waves propagate within the material. The dispersion relation for calcite, shown in Figure 4.5, is described by the equation:

$$\omega(k) = \frac{2\pi\omega}{nc} \tag{4.3}$$

With :

- $\omega$ the angular frequency in rad/s.

- $n$ the real part of the material's CRI.
- $c$ is the speed of light in m/s.

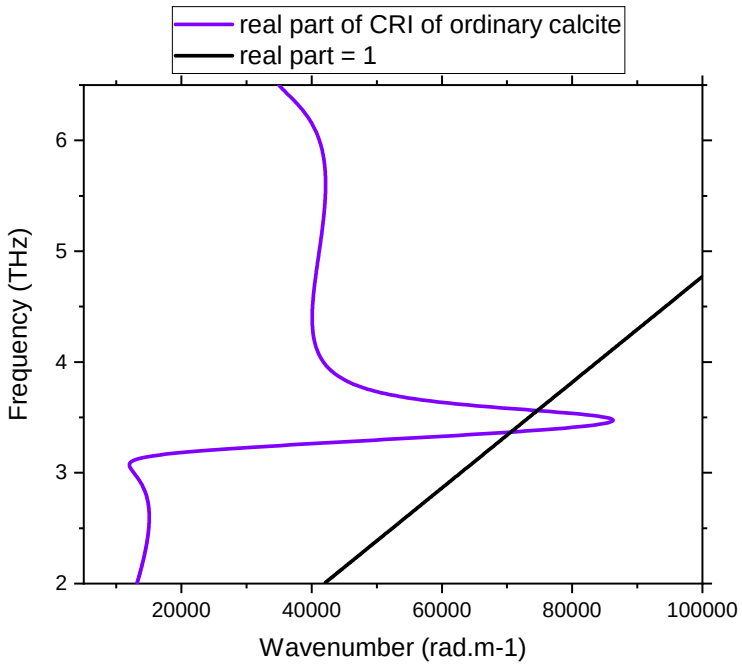


Figure 4.5: Plot of the dispersion relation as a function of the angular wavenumber. The purple line represents the value calculated with the real part of CRI of calcite and the black line the value for a real part that is equal to 1.

The purple line in Figure 4.5 represents the dispersion relation for calcite, calculated using its real part of the CRI, while the black line corresponds to a scenario where the real part of the CRI is equal to 1. This graph provides insight into the wave propagation behavior in calcite: when the real part of the CRI exceeds the black line, the wave is propagative in the bulk; below this line, the wave becomes non-propagative.

The dispersion relation indicates a strong coupling excitation at 3.6 THz, signifying the existence of a phonon-polariton mode in calcite. This notable feature closely corresponds with the frequencies of the transverse and longitudinal optical modes, as demonstrated in prior studies of phonon-polaritons across various materials [151–153]. The pronounced phonon-polariton coupling in calcite arises from its crystal anisotropy, which facilitates enhanced light-matter interactions at THz frequencies.

Calcite's uniaxial crystal structure adds complexity to its interaction with electromagnetic waves. The different refractive indices for the ordinary and extraordinary axes (for x, y, and z directions, respectively) can further influence the phonon-polariton behavior, depending on the polarization of the incident light.

The results presented focus primarily on a single polarization, but future work could explore how varying polarization impacts both the scattering and absorption cross-sections. Given that calcite's optical response is sensitive to polarization, the exploration of such effects could yield richer insights into its light-matter coupling mechanisms.

## 4.4 Particle size effects on polariton mode

As previously mentioned, calcite's real part of the complex refractive index (CRI) significantly impacts its behavior, particularly due to the presence of polaritons. When examining the effect of particle size on polariton modes, this influence becomes increasingly complex, as size-dependent changes introduce higher-order electromagnetic interactions. According to Mie theory, for nanoparticles much smaller than the incident wavelength, only dipole effects dominate. However, as the particle size increases into the micro-scale range, these interactions evolve, and higher-order multipole effects appear, altering the particle's electromagnetic field distribution and optical properties [154].

This section investigates how particle size influences the optical properties and electric field distribution of calcite. Particles with radii of 5, 10, and 15 µm are used as examples to illustrate these size effects.

### 4.4.1 5 µm radius particle: emergence of dipolar Mie mode

For a calcite particle with a radius of 5 µm, the phonon-polariton mode is recovered at 3.6 THz. However, a dipolar Mie mode also begins to appear at 2.8 THz, as indicated by the electric field distribution shown in Figure 4.7. At this size, both the absorption and scattering cross sections are comparable at 3.6 THz.

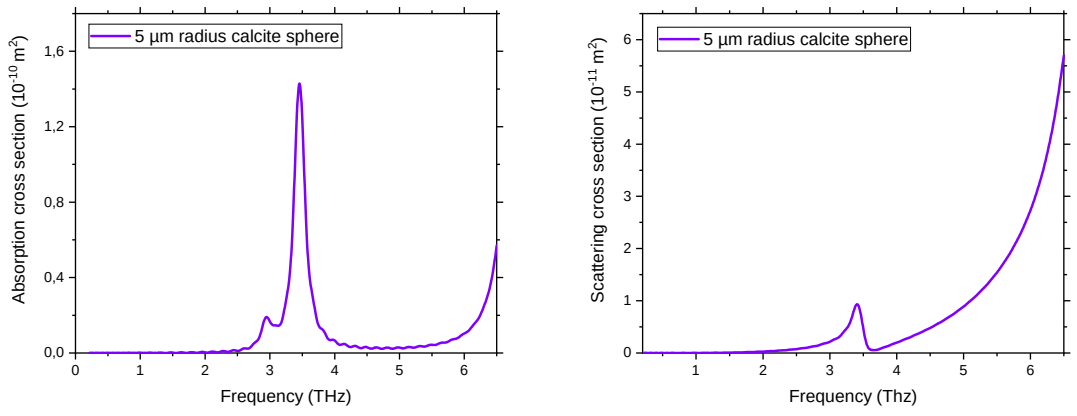


(a) (b)

Figure 4.6: Absorption (a) and scattering (b) cross sections of calcite particle of 5 µm radius.

The electric field distribution at 2.8 THz (Figure 4.7) demonstrates the onset of the dipolar Mie mode, while the distribution at 3.6 THz (Figure 4.7) continues to highlight the phonon-polariton resonance.

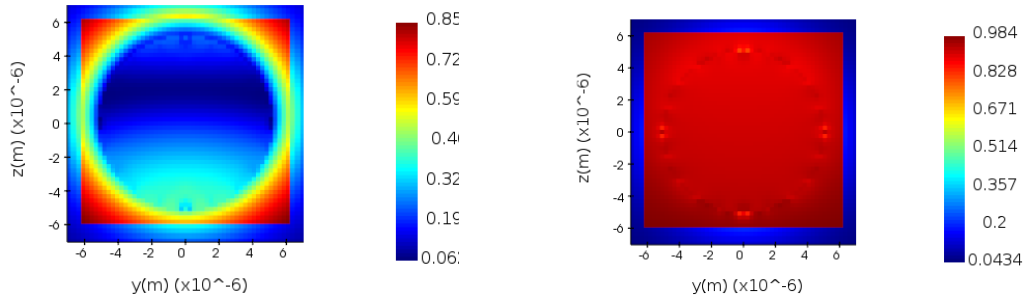


(a) (b)

Figure 4.7: Electrical field distribution plots for calcite particle of 5 µm radius, at 2.8 THz (a) and 3.6 THz (b).

### 4.4.2 10 µm radius particle: broadened peaks and new modes

For a calcite particle with a 10 µm radius, both the absorption and scattering peaks broaden and shift to lower frequencies. Additionally, new features begin to emerge, particularly a bulk mode absorption. A second Mie mode appears at 5.5 THz, while a quadrupole mode arises at 6.3 THz. These new modes reflect the particle's increased ability to support more complex modes as its size grows.

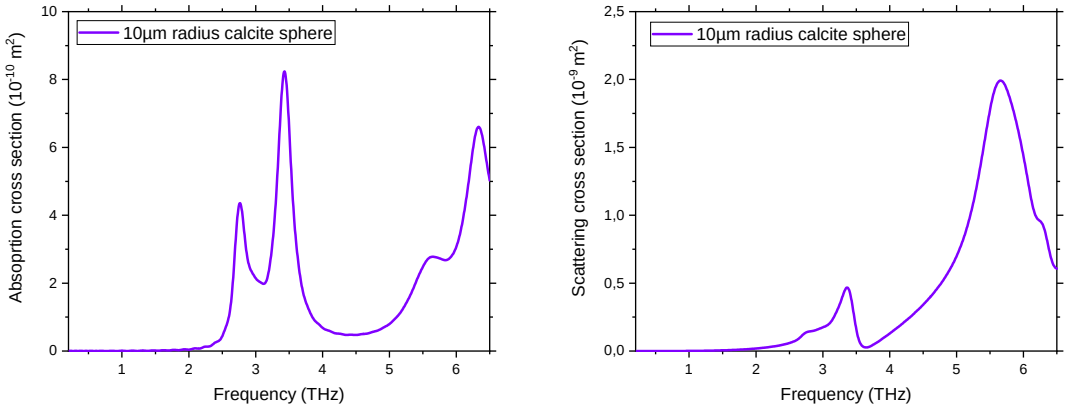


(a) (b)

Figure 4.8: Absorption (a) and scattering (b) cross sections of calcite particle of 10 µm radius.

The electric field distributions at various frequencies (Figure 4.9) illustrate the evolution of higher-order modes. At 2.7 THz (Figure 4.9), the dipolar Mie resonance is still discernible. However, at 5.5 THz (Figure 4.9), another dipolar mode

emerges. The quadrupole mode at 6.3 THz (Figure 4.9) exhibits an increasingly intricate interaction between the particle and the incident field.

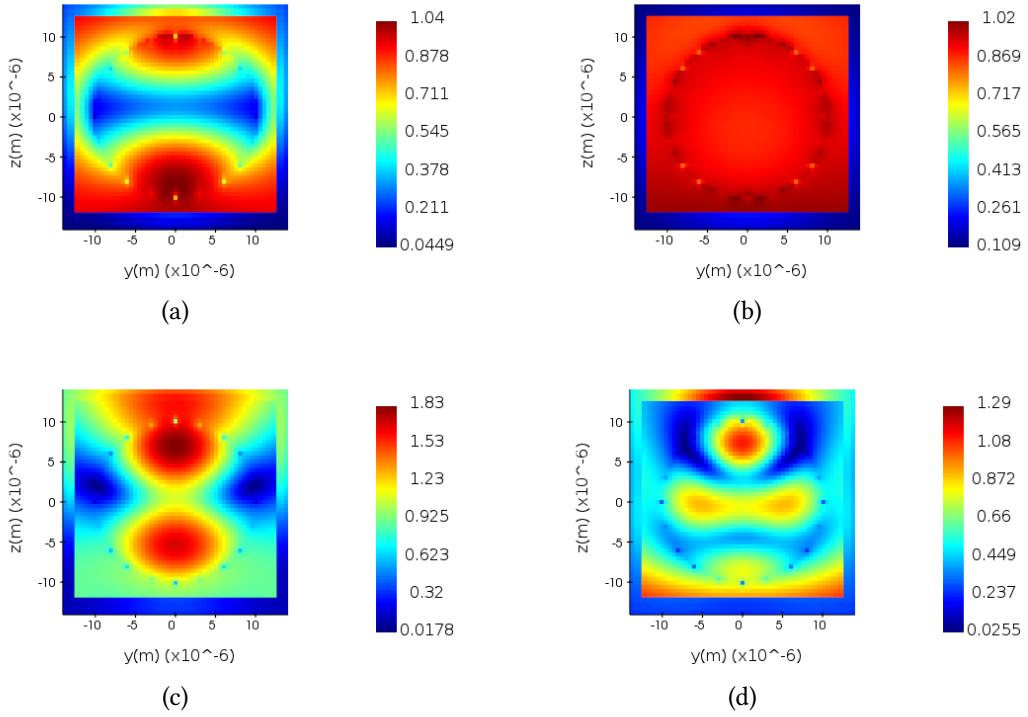


Figure 4.9: Electrical field distribution plots for calcite particle of 10 µm radius, at 2.7 THz (a), 3.5 THz (b), 5.5 THz (c) and 6.3 THz (d).

### 4.4.3 15 µm radius particle: emergence of additional multipolar modes

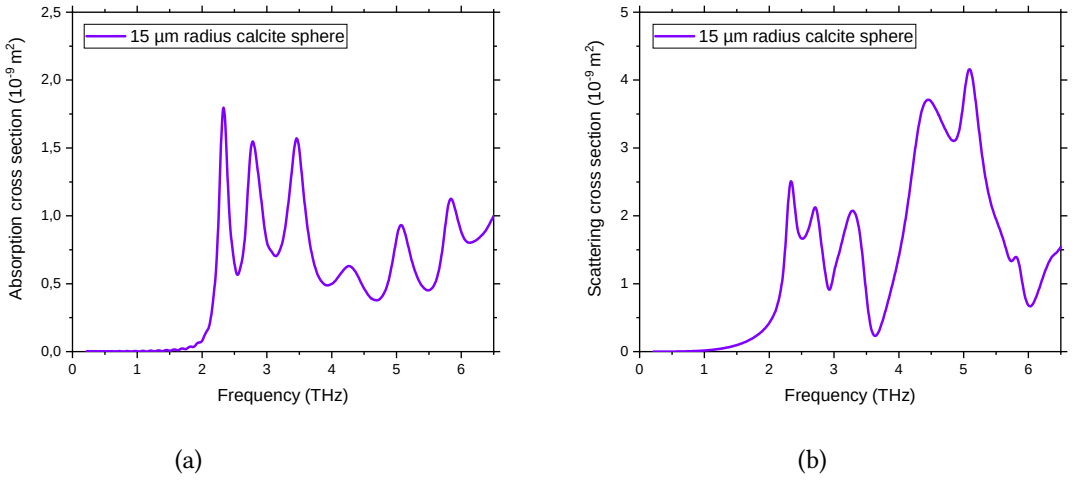


Figure 4.10: Absorption (a) and scattering (b) cross sections of calcite particle of 15 µm radius.

For particles with even larger radii, such as 15 µm, bulk absorption continues

to increase, and additional multipolar modes emerge. Figure 4.10 shows the absorption and scattering cross sections, where more complex modes dominate the particle's optical response.

The corresponding electric field distributions presented in Figure 4.11 highlight the occurrence of increasingly complex interactions. Notably, at 5 THz, a quadrupolar mode becomes evident, while at 5.8 THz, a hexapolar mode manifests.

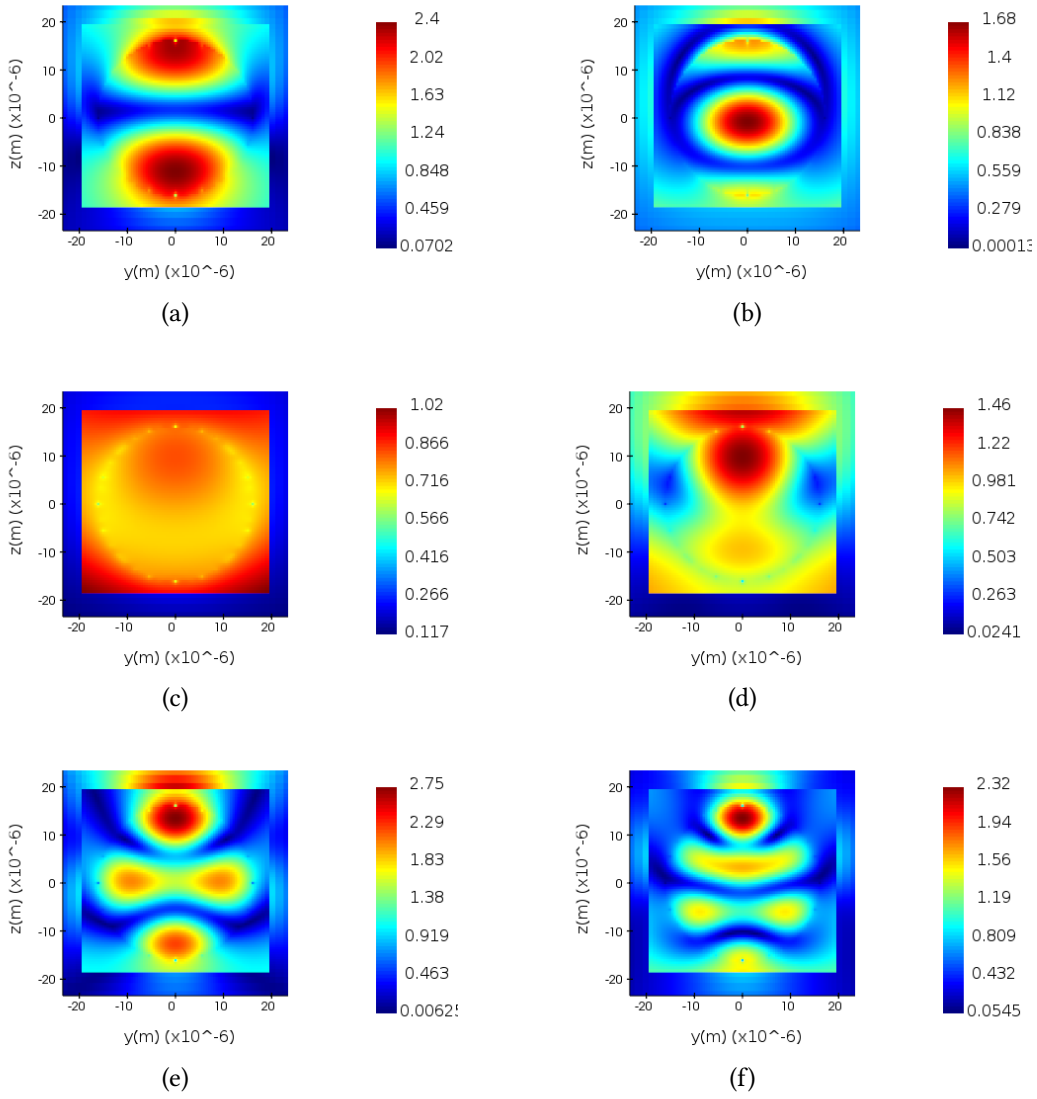


Figure 4.11: Electrical field distribution plots for calcite particle of 15 µm radius, at 2.3 THz (a), 2.75 THz (b), 3.4 THz (c), 4.2 THz (d), 5 THz (e) and 5.8 THz (f).

### 4.4.4 Comparison of experimental and simulated cross sections

Finally, a comparison between experimental and simulated results highlights the significant role particle size plays in the extinction cross section. Figure 4.12 compares the experimentally derived absorption cross sections of calcite aerosols and pelletized samples with simulated cross sections for calcite spheres of 2.65 µm and 12.35 µm radii. The experimental results confirm that smaller particles, as found in aerosols, show a single peak corresponding to the polariton resonance, while larger particles exhibit additional Mie dipolar modes, as seen in the pelletized samples.

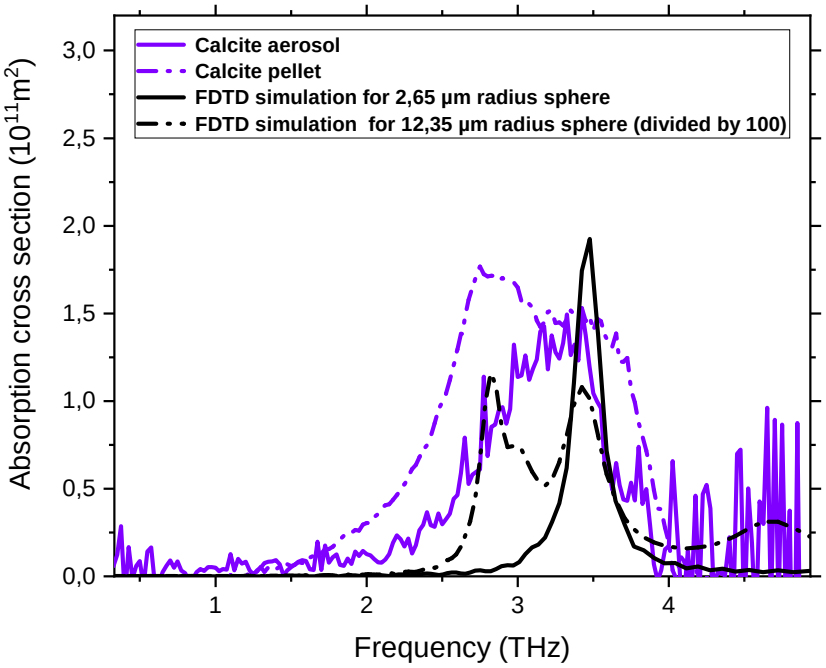


Figure 4.12: Calculated effective cross section of calcite aerosol (purple) and calcite pellet (dotted purple) compared to simulated absorption cross section of a single calcite sphere of 2.65 µm radius (black) and of 12.35 µm radius (dotted black) in the 0.2-5 THz range. The cross section of 12.35 µm has been scaled by dividing by 100.

In conclusion, larger calcite particles exhibit stronger absorption and scattering cross sections due to their ability to support multiple Mie and polariton modes. Coarse particles (larger than 10 µm), which constitute about a quarter of atmospheric aerosols, have absorption and scattering cross sections up to 100 times greater than smaller particles. Despite being fewer in number, their enhanced optical properties give them a disproportionately large influence on the radiative properties of atmospheric particles, contributing significantly to atmospheric energy balance and radiative forcing. This makes their study essential for understanding aerosol-climate interactions.

## 4.5 Numerical methods for extinction and effective medium approximations

### 4.5.1 Extinction calculations

To compare the extinction cross-sections, two Python codes were developed. The first code calculates extinction cross-sections using simulated absorption and scattering data, while the second relies on Mie theory combined with spherical Bessel functions.

Both codes take as input the lognormal fit of the experimentally measured size distribution. This distribution corresponds to a calcite aerosol concentration of 64 mg/m³, with a mean particle diameter of 385 nm and a standard deviation of 2 µm, as shown in Figure 4.13.

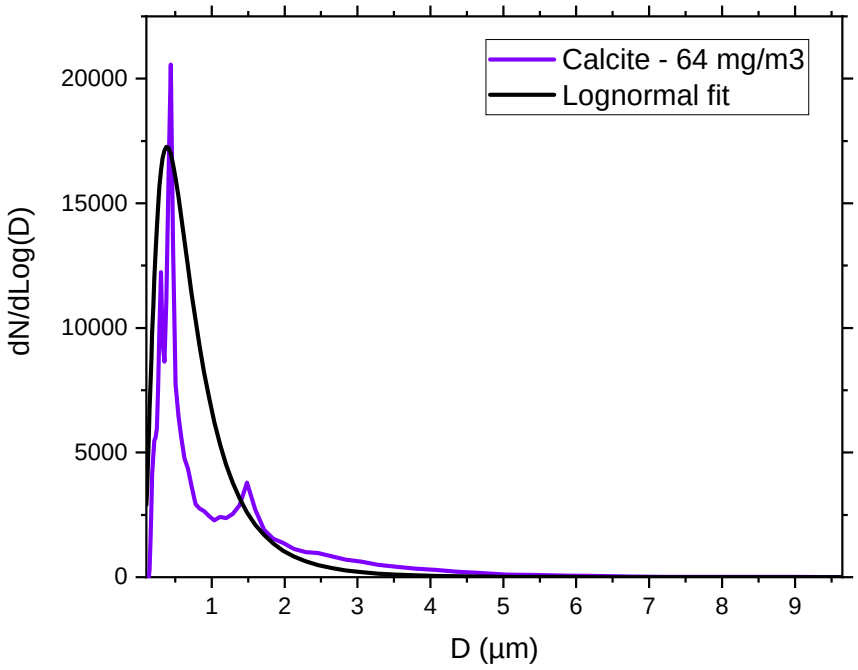


Figure 4.13: Lognormal fit of the size distribution for a concentration of 64 mg/m$^3$ for a mean diameter of 385 nm and a standard deviation of 2.

#### 4.5.1.1 Method 1: simulated extinction calculation

The first method involves calculating the extinction cross-section as the sum of absorption and scattering cross-sections obtained from FDTD (Finite-Difference Time-Domain) simulations. The input particle diameters range from 0.2 µm to 9.2 µm, incremented by 1 µm for each size. For each size, the extinction cross-section is computed and multiplied by the corresponding weight in the size distribution,

determined using linear interpolation. The total extinction is then normalized by the total size distribution weight.

#### 4.5.1.2 Method 2: Mie theory extinction calculation

The second method uses Mie theory, where extinction is derived by calculating the Mie coefficients, $a_n$ and $b_n$, for each particle size. These coefficients are solutions to Maxwell's equations for spherical particles and depend on the refractive index and size parameter of the particles. The Mie coefficients $a_n$ and $b_n$ are derived using spherical Bessel functions and the Riccati-Bessel function, which incorporates the complex refractive index.

$$a_n = \frac{\tilde{n}\psi_n(\tilde{n}x)\psi_n'(x) - \psi_n(x)\psi_n'(\tilde{n}x)}{\tilde{n}\psi_n(\tilde{n}x)\xi_n'(x) - \xi_n(x)\psi_n'(\tilde{n}x)} \tag{4.4}$$

$$b_n = \frac{\psi_n(\tilde{n}x)\psi_n'(x) - \tilde{n}\psi_n(x)\psi_n'(\tilde{n}x)}{\psi_n(\tilde{n}x)\xi_n'(x) - \tilde{n}\xi_n(x)\psi_n'(\tilde{n}x)} \tag{4.5}$$

With :

- $\tilde{n}$ the complex refractive index.
- $x$ the size parameter.
- $\psi_n(x)$ the spherical Bessel function of the first kind.
- $Y_n(x)$ spherical Bessel function of the second kind.
- $\xi_n(x) = \psi_n(x) - iY_n(x)$ the Riccati-Bessel function.

The extinction efficiency factor, $Q_{ext}$, is computed as follows:

$$Q_{\text{ext}} = \frac{2}{x^2}\sum_{n=1}^{\infty}(2n+1)\Re(a_n + b_n) \tag{4.6}$$

Where $n_{max}$ is the maximum number of terms included, which is based on the size of the particle and wavelength of the light.

The factor $\frac{2}{x^2}$ normalizes the result based on the size parameter to give the extinction cross-section relative to the geometrical cross-section of the particle. It comes from the ratio of the Mie extinction cross-section to the geometric cross-section of the particle, ensuring that the extinction efficiency is properly scaled and dimensionless.

The imaginary part of the Mie coefficients does not represent a loss of energy from the incident wave but rather a temporary storage of energy that is returned to the electromagnetic field. By taking only the real part, the formula accounts for the energy that is permanently removed from the incident wave. The extinction cross-sections are weighted according to the particle size distribution and summed to obtain the total extinction spectrum.

#### 4.5.1.3 Comparison of results

Figure 4.14 shows the extinction spectrum derived from the FDTD simulation and the Mie theory-based method.

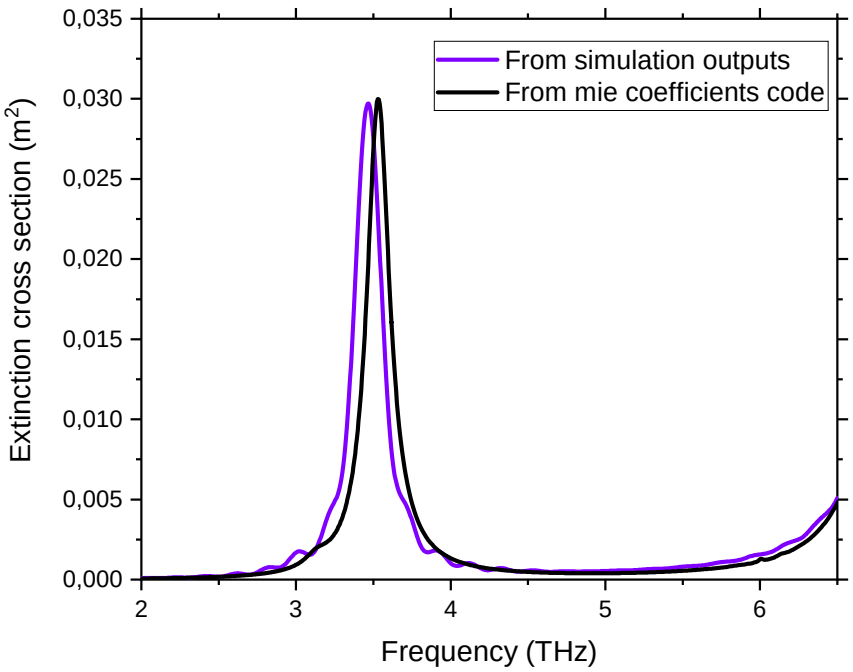


Figure 4.14: Extinction spectrum calculated from the simulations outputs (i.e. absorption and scattering cross sections at different particle radii) in purple, compared to the extinction spectrum calculated with the Mie coefficients code in black.

The simulated extinction spectrum and the one that is calculated from Mie theory overlap well. The similarity between these two extinction spectra obtained using two different calculation methods for the same input indices demonstrates that the cross sections obtained during the FDTD simulations are reliable. The extinction calculated with the simulated cross sections averages only the data for 10 sizes, which may explain the slight difference between the two extinctions.

A final observation is that the simulated extinction spectra are finer than those measured experimentally, suggesting that the particle size distribution may indeed include larger particles. Consequently, the THz beam is likely capable of detecting a broader range of particle sizes. However, larger particles may sediment more rapidly and could impact the experimental cell, preventing them from being captured by the PROMOLED particle counter. This highlights the need for a comprehensive understanding of the entire particle size distribution to accurately interpret the optical responses observed in the experiments.

### 4.5.2 Effective Medium Theory (EMT)

Effective Medium Theory (EMT) is a powerful tool used to predict the macroscopic properties of composite materials based on their microscopic structure. It allows for the treatment of heterogeneous mixtures as homogeneous media by averaging the properties of individual components.

#### 4.5.2.1 Local field correction in EMT

The local field correction, often referred to as the Lorentz local field correction, plays a crucial role in effective medium theories like the Clausius-Mossotti relation. This correction accounts for the fact that, in a material, the local field experienced by an individual particle is not the same as the macroscopic external field applied to the entire material. Instead, it is influenced by the nearby particles and the surrounding medium.

In the context of the Clausius-Mossotti relation, this correction assumes that the long-range interactions between particles are isotropic, particularly for systems composed of spherical particles. Isotropy here implies that the particles interact with each other in a uniform way, regardless of direction. This assumption greatly simplifies the modeling of how these particles collectively influence the macroscopic properties of the material. For spherical particles, the assumption of isotropy holds well because the shape symmetry ensures that the local interactions average out uniformly in all directions. However, for non-spherical particles, the local field correction becomes more complicated, as anisotropy must be accounted for.

The Clausius-Mossotti relation itself is a classical equation that links the macroscopic dielectric constant (or permittivity) of a material to the polarizability of its individual particles. It is derived by considering the balance between the applied electric field and the local electric field experienced by each particle, including the effect of nearby particles via the Lorentz local field correction.

$$\frac{\alpha}{\nu} = \frac{3}{4\pi}\frac{\epsilon - 1}{\epsilon + 2} \tag{4.7}$$

$$\alpha = \frac{\epsilon_i - 1}{\epsilon_i + 2} r^3 \tag{4.8}$$

With :

- $r$ sphere radius in m.
- $\alpha$ the polarisability of each particle.
- $\nu$ the specific volume, $\frac{N}{V}$, N being the number of particles and V the total volume.

The volume fraction for spherical particles is :

$$f_i = \frac{4\pi r^3 N}{3V} \tag{4.9}$$

$$f_i = \frac{4\pi r^3}{3\nu} \tag{4.10}$$

In summary, the Lorentz local field correction in the Clausius-Mossotti relation and similar effective medium theories serves to bridge the gap between microscopic particle interactions and the observable macroscopic properties of composite materials. This approach is particularly powerful when dealing with systems where long-range interactions are isotropic, such as those involving spherical particles, leading to reliable predictions of material properties.

#### 4.5.2.2 Bruggeman and Inverse Bruggeman approximations

In addition to the Clausius-Mossotti relation, Bruggeman theory is another important effective medium theory (EMT) that extends the approach to mixtures of different materials. While the Clausius-Mossotti relation applies to systems where one phase is embedded in a continuous matrix (such as a suspension of particles in a fluid), the Bruggeman theory is more general and symmetric. It treats the different phases on equal footing, making it particularly useful for describing materials where multiple phases are distributed randomly, such as in composites or porous media. The key difference in Bruggeman's approach is that no component is assumed to dominate or act as a host matrix. Instead, all phases are considered symmetrically, and the effective property of the medium is derived by averaging the contributions of all components. For a two-component system, Bruggeman theory uses a self-consistent equation that relates the volume fractions and properties of each phase to the overall effective property of the mixture [155, 156]. For example, in the case of electrical permittivity, the Bruggeman equation for a binary mixture of materials with permittivities and volume fractions is given by:

$$f_i \frac{\epsilon_i - \epsilon_{eff}^{BG}}{\epsilon_i + 2\epsilon_{eff}^{BG}} + f_m \frac{\epsilon_m - \epsilon_{eff}^{BG}}{\epsilon_m + 2\epsilon_{eff}^{BG}} = 0 \tag{4.11}$$

With :

- $\epsilon_{eff}$ the effective permittivity of the mixture.
- $\epsilon_m$ and $\epsilon_i$, permittivity of the medium and the inclusions, respectively.
- $f_m$ and $f_i$, volume fractions of the medium and the inclusions.

The inverse Bruggeman equation for a two-phase system where one phase is dominant can be written as:

$$\epsilon_i = \epsilon_{eff}^{BG} \frac{(f_i - 2f_m)\epsilon_m + 2\epsilon_{eff}^{BG}}{f_m(\epsilon_m - \epsilon_{eff}^{BG}) + f_i(\epsilon_m - 2\epsilon_{eff}^{BG})} \tag{4.12}$$

In the terahertz frequency range, the Bruggeman theory is particularly useful for modeling aerosols with higher concentrations of particles, non-spherical particles or irregularly shaped particles, which are more common in natural aerosols. It can also suit to mixed-phase aerosols, such as water droplets combined with solid particles, where the phases have comparable volume fractions and interactions between particles cannot be neglected.

#### 4.5.2.3 Maxwell-Garnett and Inverse Maxwell-Garnett approximations

Maxwell Garnett theory, however, is specifically suited for cases where a material consists of small inclusions of one phase embedded within a continuous host medium (or matrix). This approach assumes that the inclusions are much smaller than the wavelength of any incident electromagnetic field, and that the interactions between inclusions are weak.

For a composite with spherical inclusions of dielectric constant embedded in a matrix with dielectric constant and a volume fraction of inclusions, the effective permittivity is given by the Maxwell Garnett formula:

$$\epsilon_{eff}^{MG} = \epsilon_m \frac{\epsilon_i + 2\epsilon_m + 2f_i(\epsilon_i - \epsilon_m)}{\epsilon_i + 2\epsilon_m - f_i(\epsilon_i - \epsilon_m)} \tag{4.13}$$

This formula assumes that :

- The inclusions are small compared to the wavelength of any electromagnetic field, meaning they do not disturb the field too much.
- Inclusions do not strongly interact with each other; their effects on the macroscopic properties are largely independent.
- The volume fraction of inclusions is generally small, so the host medium is the dominant component of the composite.

Inverse Maxwell Garnett theory, on the other hand, works in reverse. It is used to retrieve the permittivity of the inclusions based on known values for the effective permittivity of the composite, the permittivity of the host medium, and the volume fraction of inclusions :

$$\epsilon_i = \epsilon_m \frac{\epsilon_{eff}^{MG}(f_i + 2) - 2f_m\epsilon_m}{\epsilon_m(2f_i + 1) - \epsilon_{eff}^{MG} f_m} \tag{4.14}$$

At THz frequencies, many aerosol particles are typically smaller than the wavelength, which makes the Maxwell Garnett assumption of weakly interacting inclusions valid.

However, it is crucial to recognize the numerical limitations associated with these methods, which necessitate a more analytical approach. The challenges inherent in the Inverse Maxwell-Garnett theory stem from several factors related

to its foundational assumptions. For instance, the numerical implementation of these models can experience instabilities, particularly when calculating permittivity at extreme volume fractions. Additionally, strong interactions among inclusions can lead to significant deviations from the predicted effective permittivity, complicating the numerical analysis further.

Initially, I attempted to implement the inverse formulas directly; however, I discovered that utilizing optimization codes for minimization yielded more reliable results. Currently, I am focused on integrating this methodology into Fit@TDS, which will enable the extraction of the material's refractive index independently of the inclusion volume fraction. This approach promises to enhance the accuracy and robustness of our analyses.

### 4.5.3 Maxwell-Garnett Mie theory (MGM)

The Maxwell Garnett theory is based on the assumption that aerosol particles are much smaller than the wavelength of the electromagnetic waves interacting with them. In this scenario, the particles are treated as dipoles and their interactions with the electromagnetic field are described by Rayleigh scattering. When the particle size becomes comparable to the THz wavelength, simple Rayleigh scattering breaks down, and Mie scattering must be used to accurately describe the interaction of electromagnetic waves with particles.

The Modified Maxwell-Garnett with Mie correction is an extension of the classical Maxwell-Garnett effective medium theory. It accounts for the scattering and absorption effects that occur when light interacts with particles whose size is comparable to the wavelength of light. This is achieved by incorporating the Mie theory, which describes how spherical particles scatter electromagnetic waves.

The Mie correction is derived from the Mie coefficients and accounts for the scattering efficiencies:

$$\text{Mie correction} = \sum_{n=1}^{n_{max}} \left( |a_n|^2 + |b_n|^2 \right) \tag{4.15}$$

Where $a_n$ and $b_n$ are the electric and magnetic Mie coefficients for different scattering modes, and $n_{max}$ is the maximum order of the Mie modes (determined by the size of the particle and the wavelength of light).

The Mie correction modifies the original Maxwell-Garnett formula to account for the additional scattering and absorption effects. The modified formula becomes:

$$\epsilon_{effcorrected} = \epsilon_{eff} + \text{Mie correction} \times \epsilon_{matrix} \times f \tag{4.16}$$

The Mie correction is applied to the permittivity of the matrix in the Modified Maxwell-Garnett formula because the correction reflects how the scattering and absorption effects modify the electromagnetic response of the host medium when light interacts with the dispersed particles. The scattering and absorption effects

represented by the Mie correction describe how the presence of particles modifies the wave propagation in the surrounding medium, which is the matrix. The correction is also multiplied by the volume fraction of of the particles, because the scattering and absorption effects only affect a portion of the matrix depending on the concentration of particles.

This modification adds a term proportional to the scattering efficiency to the effective permittivity, thereby capturing the additional optical effects caused by the interaction of light with the particles. Each size has its own Mie correction, and the total effective permittivity is computed by weighting the corrected permittivities according to the particle size distribution.

The code applies the Maxwell-Garnett theory modified with Mie coefficients, to determine the effective permittivity of the matrix containing the particles. For each frequency, it calculates Mie coefficients for each particle size in the distribution and weights the contribution of each size to the effective permittivity. The effective refractive index is then computed from the effective permittivity for each frequency [157].

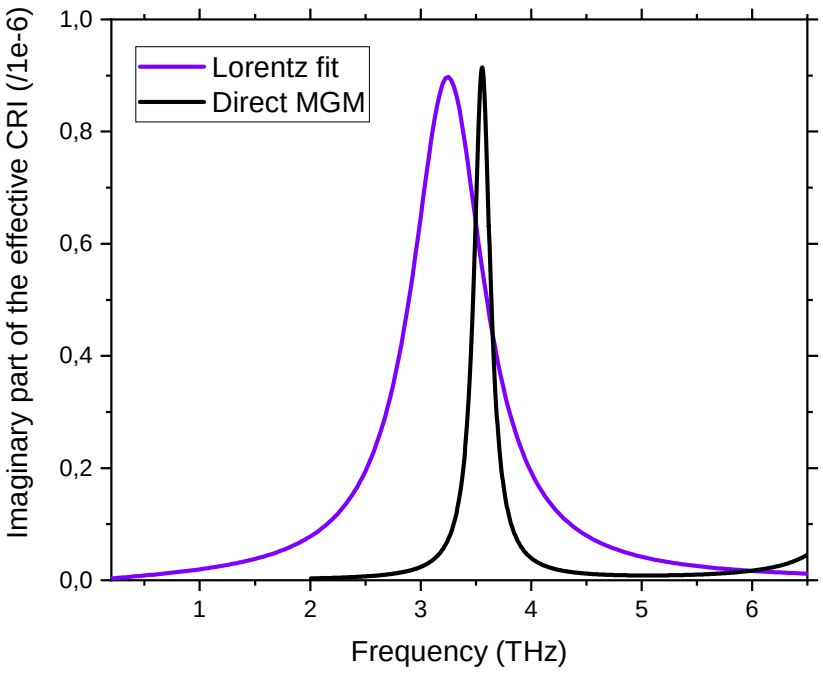


Figure 4.15: The imaginary part of the effective CRI of the calcite aerosols' Lorentz oscillator fit in purple compared to the imaginary part of the effective CRI calculated from de MGM code in black.

The results indicate that the real and imaginary parts of the effective index derived from the FIT@TDS software are broader compared to those from the MGM code (figures 4.15, 4.16). Additionally, there is a noticeable shift to higher frequen-

cies with the MGM code, showing values of 3.4 THz for MGM compared to 3.2 THz for FIT@TDS. This discrepancy suggests that the size distribution provided by the optical particle sizer does not accurately represent the particles interacting with the THz beam. The effective CRI from the MGM code was calculated for a volume fraction of $2 \times 10^{-6}$ which is consistent with the experiment.

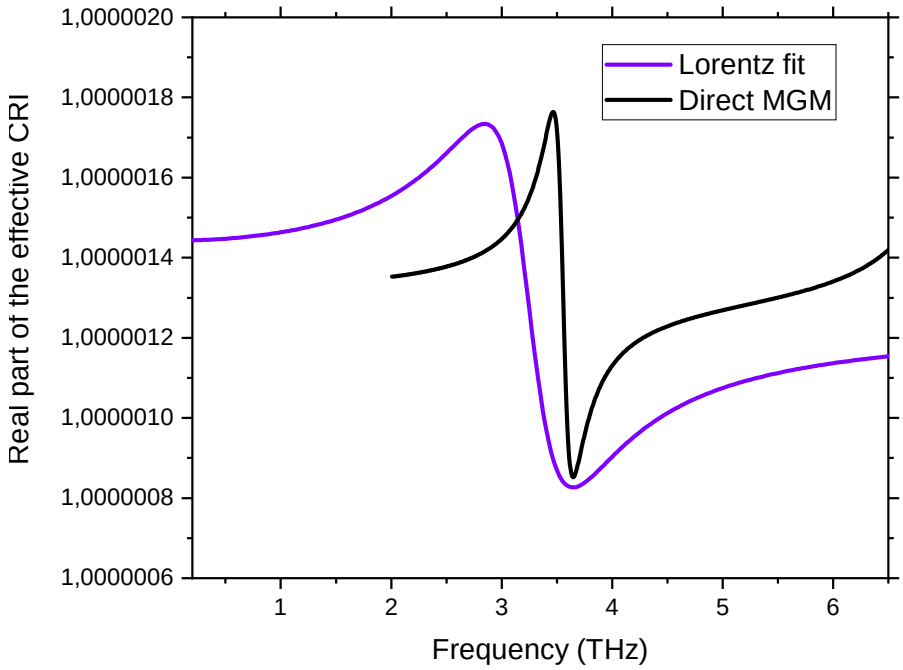


Figure 4.16: The real part of the effective CRI of the calcite aerosols' Lorentz oscillator fit in purple compared to the real part of the effective CRI calculated from de MGM code in black.

In conclusion, developing a dedicated code to infer the particle size distribution from the effective index of the suspended calcite particles, along with the expected index values, would provide valuable insights into the interaction between THz radiation and aerosol particles. As previously mentioned, the experimental granulometric distribution may not fully capture the range of particle sizes that the THz beam interacts with. It is plausible that particles with diameters around 10 µm are present and interact with the beam, significantly influencing the effective index recorded in our experiments.

To address this discrepancy, a subsequent step would involve performing an inverse Maxwell-Garnett (MGM) analysis. This process would utilize the granulometric distribution along with the measured effective index to directly deduce the refractive index of the suspended calcite particles.

Furthermore, this approach not only aims to enhance our understanding of the optical properties of calcite aerosols but also seeks to refine the predictive

models used in aerosol science. By correlating the effective index with the actual size distribution, we can improve the accuracy of our theoretical predictions, which is essential for applications in atmospheric science, remote sensing, and environmental monitoring.

The development of these two codes—one for extracting the particle size distribution from the effective index and the other for performing the inverse MGM analysis—is currently underway. Preliminary results and findings from these analyses may be presented during the thesis defense, showcasing the potential for advancing our understanding of THz interactions with aerosol particles.

## 4.6 Conclusion

In this chapter, we explored numerical methods for calculating extinction cross sections and discussed EMT for characterizing the complex behavior of calcite aerosols in the THz frequency range. The comparison of extinction spectra using two different approaches —simulated absorption and scattering cross sections from FDTD simulations and Mie theory—demonstrated strong agreement between the methods, validating the reliability of both approaches. While minor differences were noted, these are attributed to the discrete particle sizes considered in the simulations and the inherent limitations of numerical averaging.

The effective medium approximations provided a deeper understanding of how the macroscopic electromagnetic properties of a composite material, such as aerosols, can be derived from its microscopic structure. Classical models like the Clausius-Mossotti relation, Bruggeman theory, and Maxwell-Garnett theory, along with their inverse counterparts, were examined. These models offer valuable insights into the behavior of particles in different concentration regimes and their interactions with the surrounding matrix.

To bridge the gap between Rayleigh scattering for small particles and Mie scattering for larger ones, we introduced the Modified Maxwell-Garnett Theory with Mie corrections. This approach allows for a more accurate representation of light-particle interactions, particularly when particle sizes are comparable to the THz wavelength. By incorporating Mie coefficients, the method accounts for both scattering and absorption effects, providing a refined calculation of the effective complex refractive index (CRI).

The results of the MGM code were compared with experimental data from the FIT@TDS software, revealing discrepancies in both the broadening and frequency shifts of the effective CRI. These differences highlight the limitations of the optical particle sizer in capturing the full range of particle sizes that interact with the THz beam. Overall, this work underscores the importance of combining various theoretical and numerical approaches to better understand aerosol behavior in the THz region and improve the accuracy of extinction and effective medium predictions.

Future work could focus on refining particle size distributions based on measured extinction spectra or developing reverse-engineering techniques to generate size distributions from effective CRI data, offering further opportunities to enhance the precision of aerosol characterization in complex environments. Future work could also involve conducting simulations with more complex particle shapes. Having established that Mie effects play a significant role in the THz range for the analysis of suspended atmospheric particles using spherical models, exploring non-spherical geometries could provide deeper insights into the interactions and behaviors of aerosols in real-world conditions. This approach would enhance our understanding of how variations in particle morphology influence scattering and absorption characteristics, potentially leading to more accurate predictions of aerosol impacts on climate and atmospheric processes.

In summary, this chapter emphasizes the critical need for integrating various theoretical and numerical approaches to advance our understanding of aerosol behavior in the terahertz (THz) range, with particular focus on phonon-polariton aerosols and their multifaceted role in climate dynamics. These aerosols exhibit a high efficiency in absorbing infrared radiation, which can lead to localized warming and intensify the greenhouse effect, particularly in regions of elevated aerosol concentration. However, the significance of this absorption effect compared to that of infrared and ultraviolet-visible (UV-vis) radiation remains uncertain and requires further investigation. While there is a possibility that phonon-polariton aerosols could play a role in climate dynamics, their overall impact is not yet well understood, necessitating additional research to explore their interactions and contributions to atmospheric processes.

Beyond their thermal and radiative impacts, phonon-polariton aerosols have potential implications for atmospheric chemistry and photochemical reactions [158]. The unique electromagnetic properties of these aerosols could influence reaction kinetics on particle surfaces, affecting the formation or breakdown of certain atmospheric compounds. Their interactions with solar radiation, especially in the THz to infrared range, might also catalyze or inhibit photochemical reactions that impact atmospheric composition, ozone dynamics, and pollutant lifetimes.

Calculations are necessary to quantify the effects of polaritons, particularly through radiative transfer computations, as current understanding remains speculative. Altogether, understanding these unique thermal, optical, and chemical influences of phonon-polariton aerosols is crucial for accurately predicting their broader implications in climate and atmospheric chemistry and for developing effective mitigation strategies in response to their complex environmental interactions.

# General conclusion

This thesis presents a pioneering approach to investigating atmospheric aerosols in the THz frequency range, filling significant gaps in understanding their optical properties and environmental impacts. Leveraging a custom-developed measurement system based on THz-TDS, this research offers new insights into aerosol interactions in the THz domain (0.2–5 THz) and covers particle diameters ranging from 0.1 to 10 µm. By capturing THz absorption and scattering phenomena across both natural and synthetic aerosols, including Gobi Desert dust, calcite, and kaolinite, the study establishes a framework for interpreting aerosol properties that influence climate dynamics, especially in radiative forcing and atmospheric composition.

A key innovation of this work is the development and validation of a THz-TDS aerosol measurement bench, characterized by its sensitivity, signal stability, and uncertainties in THz signal interaction. This setup enables high-precision measurements of resuspended particles, achieving detection thresholds as low as 1.6 mg/m³ for Gobi Desert dust and 10 mg/m³ for calcite. During moderate dust events, atmospheric concentrations in the troposphere can typically range from 20 to 50 µg/m³, while in severe dust storms, concentrations may soar to as high as 1,000 µg/m³ [159, 160]. By referencing the Gobi concentration and considering an enhancement in sensitivity ranging from 1.5 for severe storms to 30 times for moderate events, our system could potentially facilitate real-time monitoring of these atmospheric dust concentrations in the troposphere.

The resulting THz extinction spectra show a proportional relationship to particle concentration in the cell, confirming the system's reliability and consistency. By rigorously examining uncertainties, particularly in the imaginary component of the effective complex refractive index, it was confirmed that observed signals indeed reflect particle interactions rather than instrumental artifacts. Notably, the spectral region around 3 THz emerged as significant for studying aerosols, revealing unique absorption features that enhance sensitivity to particle composition and morphology within this band.

In addition to optical measurements, this research incorporated comprehensive material characterizations using SEM-EDX and XRD. These analyses provided a detailed picture of the chemical composition, structural morphology, and crystalline phases of the aerosol samples. It allowed for precise identification of el-

emental composition and particle morphology at high resolution, which is essential for correlating physical and chemical characteristics with optical responses in the THz range.

An automated analysis performed on Gobi Desert particles showed that the sample was composed of approximately 40.8% illite, 29.4% calcite, 9.1% quartz, and 20.7% other clays, with chemical compositions suggesting external mixing tendencies. This compositional analysis demonstrated that, when scaled to 70% of illite's extinction, illite's response accounts for a substantial portion of the Gobi Desert sample's behavior for the same mass. Calcite likely contributes to the remaining response around 3 THz, while quartz, though prominent in the infrared range, has negligible influence in the THz domain.

Furthermore, differences in responses were observed between pellets and suspensions of the same powder, underscoring the importance of conducting experiments directly on atmospheric aerosols in suspension. These discrepancies are primarily attributed to size effects; larger particles found in pellets do not resuspend easily. Ideally, the powder should be sieved to ensure that the particle size distribution in the pellets is representative of that in the suspensions. This would allow for a clearer understanding of whether any remaining effects arise from changes in the environment surrounding the particles, such as the contrast between a docosane matrix and gaseous nitrogen. In addition to these considerations, the investigation of powders in pellet form allowed for an exploration of complex natural compounds, including feldspar. Remarkably, the results revealed that THz-TDS could effectively differentiate between the various poles of plagioclase feldspars, providing a novel approach for identifying mineralogical variations in desert sands, which is essential for atmospheric dust characterization.

The effective indices of various compounds were extracted using custom developed algorithms, Correct@TDS and Fit@TDS. Particular attention was paid to extracting uncertainties associated with transmission as well as with the complex refractive indices, which is essential for bolstering confidence in the robustness of our data. The integration of Lorentz oscillator models for fitting not only improved the accuracy of the adjustments but also allowed for a better capture of the dispersive behaviors of the studied materials. This approach provided a solid foundation for validating experimental results and contributed to a deeper understanding of optical interactions in the THz domain. Moreover, the optimization of the algorithms facilitated data analysis, making the extraction process more efficient and reproducible, while also paving the way for future studies on other complex compounds.

Building on this methodological framework, I explored numerical methods for calculating extinction cross sections and Effective Medium Theory to characterize calcite aerosols in the THz frequency range, finding strong agreement between Finite Difference Time Domain simulations and Mie theory, which val-

idated their reliability. Classical models like Clausius-Mossotti, Bruggeman, and Maxwell-Garnett provided insights into the relationship between macroscopic electromagnetic properties and microscopic structures, highlighting particle interactions across varying concentration regimes. The Modified Maxwell-Garnett Theory, enhanced with Mie corrections, improved the modeling of light-particle interactions, particularly for THz wavelengths. However, discrepancies between the MGM code results and FIT@TDS data revealed limitations in capturing the full range of particle sizes affecting the effective CRI.

This work establishes a foundational framework for future research on aerosols in the THz domain, with opportunities to advance aerosol-cell design aimed at improving experimental precision. Subsequent studies may investigate THz interactions with liquid aerosols, explore atmospheric reaction kinetics, and assess aerosol responses to emerging 5G frequencies. The potential for outdoor measurements using this type of spectrometer appears promising, particularly with ongoing miniaturization efforts and anticipated enhancements in sensitivity.

Furthermore, advancements in photoconductive antennas, which operate at higher frequencies and provide improved dynamic range, are expected to significantly boost the capabilities of our measurement system. The exploration of a multipass cell setup could also lead to remarkable improvements in detection limits and expand the range of aerosol analyses.

In addition, refining particle size distributions obtained from extinction spectra and examining non-spherical geometries will enhance our understanding of aerosol behavior, particularly within the context of Finite Difference Time Domain simulations. Collaborations with climatologists are strongly encouraged to quantify the climatic effects of polaritonic particles and integrate these findings into climate models, thereby advancing our understanding of radiative forcing and aerosol-cloud interactions on a global scale.

Overall, this thesis not only advances atmospheric science and terahertz spectroscopy but also addresses pressing environmental and climate-related questions. By providing tools and data to better understand aerosol impacts on radiative balance and atmospheric chemistry, this research is positioned to inform future climate strategies, enhance environmental monitoring, and contribute to global efforts to mitigate climate change.

# Bibliography


[1] Melanie Lavancier. Heuristic approach to take up the challenge of terahertz time-domain spectroscopy for biology. Electronics. Université de Lille, 2021.

[2] Théo Hannotte. THz radiation confinement using metallic micro-resonators, for spectroscopy and manipulation of single nanometric samples. Micro and nanotechnologies/Microelectronics. Université de Lille, 2022. English.

[3] Deschutter, Lise. “Propriétés Optiques Des Poussières Désertiques de Gobi et de Ses Composés Purs: Spectres d’extinction Expérimentaux et Détermination Des Indices Complexes de Réfraction.” These de doctorat, Université de Lille, 2022.

[4] Raghava R. Kommalapati and Kalliat T. Valsaraj, Atmospheric Aerosols. January 8, 2009 , 1-10, DOI:10.1021/bk-2009-1005.ch001.

[5] Pöschl, U. (2005), "Atmospheric Aerosols: Composition, Transformation, Climate and Health Effects". Angewandte Chemie International Edition, 44: 7520-7540.

[6] Meinrat O. Andreae, Paul J. Crutzen ,Atmospheric Aerosols: Biogeochemical Sources and Role in Atmospheric Chemistry.Science276,1052-1058(1997).DOI:10.1126/science.276.5315.1052

[7] Lutgens, F. K., and Tarbuck, E. J., 2013: The Atmosphere: An Introduction to Meteorology. 12th ed. Pearson Education, Inc, USA, 533 pp.

[8] Richardson K. et al., 2023. Earth beyond six of nine planetary boundaries. Sciences Advances. Vol. 9, Issue 37.

[9] Rockström, J., W. Steffen, K. Noone, Å. Persson, F.S. Chapin, III, E. Lambin, T.M. Lenton, M. Scheffer, C. Folke, H. Schellnhuber, B. Nykvist, C.A. De Wit, T. Hughes, S. van der Leeuw, H. Rodhe, S. Sörlin, P.K. Snyder, R. Costanza, U. Svedin, M. Falkenmark, L. Karlberg, R.W. Corell, V.J. Fabry, J. Hansen, B. Walker, D. Liverman, K. Richardson, P. Crutzen, and J. Foley, 2009: Planetary boundaries: Exploring the safe operating space for humanity. Ecol. Soc., 14, no. 2, 32.

[10] Formenti P, Schutz L, Balkanski Y, et al (2011), Recent progress in understanding physical and chemical properties of african and asian mineral dust. Atmos Chem Phys 11:8231–8256. https://doi.org/10.5194/acp-11-8231-2011.

[11] Myhre, G., D. Shindell, F.-M. Bréon, W. Collins, J. Fuglestvedt, J. Huang, D. Koch, J.-F. Lamarque, D. Lee, B. Mendoza, T. Nakajima, A. Robock, G. Stephens, T. Takemura, and H. Zhang, 2013: Anthropogenic and natural radiative forcing. In Climate Change 2013: The Physical Science Basis. Contribution of Working Group I to the Fifth Assessment Report of the Intergovernmental Panel on Climate Change. T.F. Stocker, D. Qin, G.-K. Plattner, M. Tignor, S.K. Allen, J. Doschung, A. Nauels, Y. Xia, V. Bex, and P.M. Midgley, Eds., Cambridge University Press, pp. 659-740.

[12] Boucher, O., D. Randall, P. Artaxo, C. Bretherton, G. Feingold, P. Forster, V.-M. Kerminen, Y. Kondo, H. Liao, U. Lohmann, P. Rasch, S.K. Satheesh, S. Sherwood, B. Stevens, and X.Y. Zhang, 2013: Clouds and aerosols. In Climate Change 2013: The Physical Science Basis. Contribution of Working Group I to the Fifth Assessment Report of the Intergovernmental Panel on Climate Change. T.F. Stocker, D. Qin, G.-K. Plattner, M. Tignor, S.K. Allen, J. Doschung, A. Nauels, Y. Xia, V. Bex, and P.M. Midgley, Eds., Cambridge University Press, pp. 571-657.

[13] Forster, P., T. Storelvmo, K. Armour, W. Collins, J.-L. Dufresne, D. Frame, D.J. Lunt, T. Mauritsen, M.D. Palmer, M. Watanabe, M. Wild, and H. Zhang, 2021: The Earth's Energy Budget, Climate Feedbacks, and Climate Sensitivity. In Climate Change 2021: The Physical Science Basis. Contribution of Working Group I to the Sixth Assessment Report of the Intergovernmental Panel on Climate Change [Masson-Delmotte, V., P. Zhai, A. Pirani, S.L. Connors, C. Péan, S. Berger, N. Caud, Y. Chen, L. Goldfarb, M.I. Gomis, M. Huang, K. Leitzell, E. Lonnoy, J.B.R. Matthews, T.K. Maycock, T. Waterfield, O. Yelekçi, R. Yu, and B. Zhou (eds.)]. Cambridge University Press, Cambridge, United Kingdom and New York, NY, USA, pp. 923–1054, doi:10.1017/9781009157896.009.

[14] Bauer, S.E., K. Tsigaridis, G. Faluvegi, L. Nazarenko, R.L. Miller, M. Kelley, and G. Schmidt, 2022: The turning point of the aerosol era. J. Adv. Model. Earth Syst., 14, no. 12, e2022MS003070, doi:10.1029/2022MS003070

[15] M. Wendisch, O. Hellmuth, A. Ansmann, J. Heintzenberg, R. Engelmann, D. Althausen, H. Eichler, D. Müller, M. Hu, Y. Zhang, J. Mao, Radiative and dynamic effects of absorbing aerosol particles over the Pearl River Delta, China, Atmospheric Environment, Volume 42, Issue 25, 2008, Pages 6405-6416.

[16] Huang H, Gu Y, Xue Y, et al (2019), Assessing aerosol indirect effect on clouds and regional climate of east/south asia and west africa using NCEP GFS. Climate dynamics 52,9-10:5759–5774. https://doi.org/10.1007/s00382-018-4476-9.

[17] Chen, Jingyi ; Liu, Yangang ; Zhang, Minghua ; Peng, Yiran, New understanding and quantification of the regime dependence of aerosol-cloud interaction for studying aerosol indirect effects, Geophysical research letters, 2016-02, Vol.43 (4), p.1780-1787.

[18] Zhao, C., Yang, Y., Fan, H., Huang, J., Fu, Y., Zhang, X., Kang, S., Cong, Z., Letu, H., and Menenti, M.: Aerosol characteristics and impacts on weather and climate over Tibetan Plateau, Natl. Sci. Rev., 7, 492–495, https://doi.org/10.1093/nsr/nwz184, 2020.

[19] Sekiguchi, M., T. Nakajima, K. Suzuki, K. Kawamoto, A. Higurashi, D. Rosenfeld, I. Sano, and S. Mukai (2003), A study of the direct and indirect effects of aerosols using global satellite data sets of aerosol and cloud parameters, J. Geophys. Res., 108, 4699, doi:10.1029/2002JD003359, D22.

[20] Oh HJ, Ma Y, Kim J. Human Inhalation Exposure to Aerosol and Health Effect: Aerosol Monitoring and Modelling Regional Deposited Doses. Int J Environ Res Public Health. 2020 Mar 16;17(6):1923. doi: 10.3390/ijerph17061923. PMID: 32187987; PMCID: PMC7142517.

[21] Liu F., Huang Y., Zhang F., Chen Q., Wu B., Rui W., Zheng J.C., Ding W. Macrophages treated with particulate matter PM2.5 induce selective neurotoxicity through glutaminase-mediated glutamate generation. J. Neurochem. 2015;134:315–326. doi: 10.1111/jnc.13135.

[22] Mannucci P.M., Franchini M. Health Effects of Ambient Air Pollution in Developing Countries. Int. Environ. Res. Public Health. 2017;14:1048. doi: 10.3390/ijerph14091048.

[23] G. Milinevsky, Ya. Yatskiv, O. Degtyaryov, I. Syniavskyi, M. Mishchenko, V. Rosenbush, Yu. Ivanov, A. Makarov, A. Bovchaliuk, V. Danylevsky, M. Sosonkin, S. Moskalov, V. Bovchaliuk, A. Lukenyuk, A. Shymkiv, E. Udodov, New satellite project Aerosol-UA: Remote sensing of aerosols in the terrestrial atmosphere, Acta Astronautica, Volume 123, 2016, Pages 292-300, ISSN 0094-5765, https://doi.org/10.1016/j.actaastro.2016.02.027.

[24] Green, R.O., N. Mahowald, D.R. Thompson, C. Ung, P. Brodrick, R. Pollock, M. Bennett, S. Lundeen, M. Joyce, W. Olson-Duvall, B. Oaida, C. Bradley, E. Diaz, R. Clark, S. Vannan, G. Swayze, R. Kokaly, P. Ginoux, R.L. Miller, G. Okin, C. Pérez García-Pando, B. Ehlmann, O. Kalashnikova, T.H. Painter, V. Realmuto, D. Chadwick, E. Ben-Dor, D.H. Pearlshtien, L. Guanter, B. Phillips,

K. Reath, A. Thorpe, L. Shaw, A. Keebler, F. Ochoa, K. Grant, A. Sen, R. Duren, V. Obiso, M. Gonçalves-Ageitos, and Y. Huang, 2023: Performance and early results from the Earth Surface Mineral Dust Source Investigation (EMIT) imaging spectroscopy mission. In 2023 IEEE Aerospace Conference, IEEE, on-line.

[25] Chowdhary et al, Modeling Atmosphere-Ocean Radiative Transfer: A PACE Mission Perspective, Front. Earth Sci., 18 June 2019, Volume 7, https://doi.org/10.3389/feart.2019.00100.

[26] ESA (2019). Report for Mission Selection: FORUM, European Space Agency, Noordwijk,The Netherlands, ESA-EOPSM-FORM-RP-3549, 263pp.

[27] Alalam, Perla, Lise Deschutter, Antoine Al Choueiry, Denis Petitprez, and Hervé Herbin. 2022. "Aerosol Mineralogical Study Using Laboratory and IASI Measurements: Application to East Asian Deserts" Remote Sensing 14, no. 14: 3422. https://doi.org/10.3390/rs14143422.3.

[28] $https://www.esa.int/Applications/Observing_the_Earth/FutureEO/FORUM$

[29] Castellanos, P., P. Colarco, W.R. Espinosa, S.D. Guzewich, R.C. Levy, R.L. Miller, M. Chin, R.A. Kahn, O. Kemppinen, H. Moosmüller, E.P. Nowottnick, A. Rocha-Lima, M.D. Smith, J.E. Yorks, and H. Yu, 2024: Mineral dust optical properties for remote sensing and global modeling: A review. Remote Sens. Environ., 303, 113982, doi:10.1016/j.rse.2023.113982.

[30] Kok, J.F., A.A. Adebiyi, S. Albani, Y. Balkanski, R. Checa-Garcia, M. Chin, P.R. Colarco, D.S. Hamilton, Y. Huang, A. Ito, M. Klose, L. Li, N.M. Mahowald, R.L. Miller, V. Obiso, C. Pérez García-Pando, A. Rocha-Lima, and J.S. Wan, 2021: Contribution of the world's main dust source regions to the global cycle of desert dust. Atmos. Chem. Phys., 21, no. 10, 8169-8193, doi:10.5194/acp-21-8169-2021.

[31] John H. Seinfeld, Spyros N. Pandis, Atmospheric Chemistry and Physics: From Air Pollution to Climate Change, Wiley, 1998.

[32] Gillies, J. A., W. G. Nickling, and M. Tilson (2013), Frequency, magnitude, and characteristics of aeolian sediment transport: McMurdo Dry Valleys, Antarctica, J. Geophys. Res. Earth Surf., 118, 461–479, doi:10.1002/jgrf.20007.

[33] Marticorena, B. ; Bergametti, G., "Modeling the atmospheric dust cycle: 1. Design of a soil-derived dust emission scheme", Journal of Geophysical Research, Washington, DC, 1995-08, Vol.100 (D8), p.16415-16430.

[34] Meng, J., Y. Huang, D.M. Leung, L. Li, A.A. Adebiyi, C.L. Ryder, N.M. Mahowald, and J.F. Kok, 2022: Improved parameterization for the

size distribution of emitted dust aerosols reduces model underestimation of super coarse dust. Geophys. Res. Lett., 49, no. 8, e2021GL097287, doi:10.1029/2021GL097287.

[35] González-Flórez, C., M. Klose, A. Alastuey, S. Dupont, J. Escribano, V. Etyemezian, A. Gonzalez-Romero, Y. Huang, K. Kandler, G. Nikolich, A. Panta, X. Querol, C. Reche, J. Yus-Díez, and C. Pérez García-Pando, 2023: Insights into the size-resolved dust emission from field measurements in the Moroccan Sahara. Atmos. Chem. Phys., 23, no. 12, 7177-7212.

[36] Karine Deboudt, Pascal Flament, M. Choël, A. Gloter, S. Sobanska, et al.. Mixing state of aerosols and direct observation of carbonaceous and marine coatings on African dust by individual particle analysis. Journal of Geophysical Research, 2010, 115, pp.D24207-1 - D24207-14.

[37] Lesins, G., P. Chylek, and U. Lohmann, A study of internal and external mixing scenarios and its effect on aerosol optical properties and direct radiative forcing, J. Geophys. Res., 107(D10), doi:10.1029/2001JD000973, 2002.

[38] B.J. Krueger, V.H. Grassian, J.P. Cowin, A. Laskin, Heterogeneous chemistry of individual mineral dust particles from different dust source regions: the importance of particle mineralogy, Atmospheric Environment, Volume 38, Issue 36, 2004, Pages 6253-6261, https://doi.org/10.1016/j.atmosenv.2004.07.010.

[39] Bondy, A. L., Bonanno, D., Moffet, R. C., Wang, B., Laskin, A., and Ault, A. P.: The diverse chemical mixing state of aerosol particles in the southeastern United States, Atmos. Chem. Phys., 18, 12595–12612, https://doi.org/10.5194/acp-18-12595-2018, 2018.

[40] Di Biagio, C., Doussin, JF., Cazaunau, M. et al. Infrared optical signature reveals the source–dependency and along–transport evolution of dust mineralogy as shown by laboratory study. Sci Rep 13, 13252 (2023). https://doi.org/10.1038/s41598-023-39336-7.

[41] Di Biagio, Claudia, Paola Formenti, Yves Balkanski, Lorenzo Caponi, Mathieu Cazaunau, Edouard Pangui, Emilie Journet, et al. "Global scale variability of the mineral dust long-wave refractive index: a new dataset of in situ measurements for climate modeling and remote sensing," 2017. https://doi.org/10.5194/acp-17-1901-2017.

[42] Shao, Y., M. Klose, and K.-H. Wyrwoll (2013), Recent global dust trend and connections to climate forcing, J. Geophys. Res. Atmos., 118, 11,107–11,118, doi:10.1002/jgrd.50836.

[43] Sokolik, I. N., and O. B. Toon (1999), Incorporation of mineralogical composition into models of the radiative properties of mineral aerosol

from UV to IR wavelengths, J. Geophys. Res., 104(D8), 9423–9444, doi:10.1029/1998JD200048.

[44] Scanza, R. A., Mahowald, N., Ghan, S., Zender, C. S., Kok, J. F., Liu, X., Zhang, Y., and Albani, S.: Modeling dust as component minerals in the Community Atmosphere Model: development of framework and impact on radiative forcing, Atmos. Chem. Phys., 15, 537–561, https://doi.org/10.5194/acp-15-537-2015, 2015.

[45] Ryder, C. L., Highwood, E. J., Walser, A., Seibert, P., Philipp, A., and Weinzierl, B.: Coarse and giant particles are ubiquitous in Saharan dust export regions and are radiatively significant over the Sahara, Atmos. Chem. Phys., 19, 15353–15376, https://doi.org/10.5194/acp-19-15353-2019, 2019.

[46] Li, L., N.M. Mahowald, R.L. Miller, C. Pérez García-Pando, M. Klose, D.S. Hamilton, M. Gonçalves Ageitos, P. Ginoux, Y. Balkanski, R.O. Green, O. Kalashnikova, J.F. Kok, V. Obiso, D. Paynter, and D.R. Thompson, 2021: Quantifying the range of the dust direct radiative effect due to source mineralogy uncertainty. Atmos. Chem. Phys., 21, no. 5, 3973-4005, doi:10.5194/acp-21-3973-2021.

[47] Casquero-Vera, J. A., Pérez-Ramírez, D., Lyamani, H., Rejano, F., Casans, A., Titos, G., Olmo, F. J., Dada, L., Hakala, S., Hussein, T., Lehtipalo, K., Paasonen, P., Hyvärinen, A., Pérez, N., Querol, X., Rodríguez, S., Kalivitis, N., González, Y., Alghamdi, M. A., Kerminen, V.-M., Alastuey, A., Petäjä, T., and Alados-Arboledas, L.: Impact of desert dust on new particle formation events and the cloud condensation nuclei budget in dust-influenced areas, Atmos. Chem. Phys., 23, 15795–15814, https://doi.org/10.5194/acp-23-15795-2023, 2023.

[48] Jianrong BI, Jinsen SHI, Yongkun XIE, Yuzhi LIU, Tamio TAKAMURA, Pradeep KHATRI, Dust Aerosol Characteristics and Shortwave Radiative Impact at a Gobi Desert of Northwest China during the Spring of 2012, Journal of the Meteorological Society of Japan. Ser. II, 2014, Volume 92A, Pages 33-56.

[49] Forster P, Ramaswamy V, Artaxo P, et al (2007), Changes in atmospheric constituents and in radiative forcing. Cambridge University Press, United Kingdom.

[50] Laurent A, Marticorena B, Bergametti G, et al (2006), Modeling mineral dust emissions from chinese and mongolian deserts. Glob Planet Change 52:121–141. https://doi.org/10.1016/j.gloplacha.2006.02.012.

[51] Sun J, Zhang M, Liu T (2001), Spatial and temporal characteristics of dust storms in china and its surrounding regions, 1960–1999: Relations to source area and climate. J Geophys Res-Atmos 106:10,325–10,333. https://doi.org/10.1029/2000JD900665.

[52] Chen S, Huang J, Kang L, et al (2017), Emission, transport and radiative effects of mineral dust from taklimakan and gobi deserts: comparison of measurements and model results. Atmospheric Chemistry and Physics 17:2401–2421. https://doi.org/10.5194/acp-17-2401-2017.

[53] $https://geisa.aeris-data.fr/opac/$

[54] $https://eodg.atm.ox.ac.uk/ARIA/data$

[55] Huang, Y., J.F. Kok, M. Saito, and O. Muñoz, 2023: Single-scattering properties of ellipsoidal dust aerosols constrained by measured dust shape distributions. Atmos. Chem. Phys., 23, no. 4, 2557-2577.

[56] Boucher, O., 2015: Atmospheric Aerosols. Properties and Climate Impacts. Springer Netherlands, 311 pp., doi:10.1007/978-94-017-9649-1.

[57] I. Harczuk, O. Vahtras, H. Ågren, "Modeling Rayleigh Scattering of Aerosol Particles", J. Phys. Chem. B 2016, 120, 18, 4296–4301.

[58] H. Moosmuller, W. P. Arnott, "Particle Optics in the Rayleigh Regime", Air and Waste Manage. Assoc. 59:1028 –1031.

[59] Helmuth Horvath, Basic optics, aerosol optics, and the role of scattering for sky radiance, Journal of Quantitative Spectroscopy and Radiative Transfer, Volume 139, 2014, Pages 3-12, ISSN 0022-4073, https://doi.org/10.1016/j.jqsrt.2013.08.009.

[60] Eremin, A., Gurentsov, E., Popova, E. et al. Size dependence of complex refractive index function of growing nanoparticles. Appl. Phys. B 104, 285–295 (2011). https://doi.org/10.1007/s00340-011-4420-8.

[61] Irina Sokolik, Aleksandra Andronova, Tezz C. Johnson, Complex refractive index of atmospheric dust aerosols, Atmospheric Environment. Part A. General Topics, Volume 27, Issue 16, 1993, Pages 2495-2502, ISSN 0960-1686, https://doi.org/10.1016/0960-1686(93)90021-P.

[62] Luo, T., Ilyas, B., Hoegen, A.v. et al. Time-of-flight detection of terahertz phonon-polariton. Nat Commun 15, 2276 (2024). https://doi.org/10.1038/s41467-024-46515-1.

[63] Ruppin, R. “Polariton Modes of Spheroidal Microcrystals.” Journal of Physics: Condensed Matter 10, no. 35 (September 1998): 7869. https://doi.org/10.1088/0953-8984/10/35/019.

[64] J. Mandal, et al, Hierarchically porous polymer coatings for highly efficient passive daytime radiative cooling, Science, Vol 362, Issue 6412, pp. 315-319 (2019).

[65] Low T, Chaves A, Caldwell JD, Kumar A, Fang NX, Avouris P, Heinz TF, Guinea F, Martin-Moreno L, Koppens F. Polaritons in layered two-dimensional materials. Nat Mater. 2017 Feb;16(2):182-194. doi: 10.1038/nmat4792. Epub 2016 Nov 28. PMID: 27893724.

[66] Canales, Adriana, Oleg V. Kotov, Betül Küçüköz, and Timur O. Shegai. “Self-Hybridized Vibrational-Mie Polaritons in Water Droplets.” Physical Review Letters 132, no. 19 (May 10, 2024): 193804. https://doi.org/10.1103/PhysRevLett.132.193804.

[67] Daniel M. Mittleman; Perspective: Terahertz science and technology. J. Appl. Phys. 21 December 2017; 122 (23): 230901. https://doi.org/10.1063/1.5007683.

[68] Sethy, et al., "An Introduction to Terahertz Technology, Its History, Properties and Application.", International conference on computing and communication. 2015.

[69] Brown, Elliott. (2011). Fundamentals of Terrestrial Millimeter-Wave and THz Remote Sensing. International Journal of High Speed Electronics and Systems. 13. 10.1142/S0129156403002125.

[70] Fu, Z., Yamaguchi, M. Coherent Excitation of Optical Phonons in GaAs by Broadband Terahertz Pulses. Sci Rep 6, 38264 (2016). https://doi.org/10.1038/srep38264.

[71] H. -J. Song and T. Nagatsuma, "Present and Future of Terahertz Communications," in IEEE Transactions on Terahertz Science and Technology, vol. 1, no. 1, pp. 256-263, Sept. 2011, doi: 10.1109/TTHZ.2011.2159552.

[72] Mitryukovskiy, Sergey, et al. "On the influence of water on THz vibrational spectral features of molecular crystals." Physical Chemistry Chemical Physics 24.10 (2022): 6107-6125.

[73] Eliet, Sophie, et al. "Broadband super-resolution terahertz time-domain spectroscopy applied to gas analysis." IEEE Transactions on Terahertz Science and Technology 12.1 (2021): 75-80.

[74] Josette El Haddad, Bruno Bousquet, Lionel Canioni, Patrick Mounaix, Review in terahertz spectral analysis, TrAC Trends in Analytical Chemistry, Volume 44, 2013, Pages 98-105, ISSN 0165-9936, https://doi.org/10.1016/j.trac.2012.11.009.

[75] Jeyan Bichon, Melanie Lavancier, Denis Petitprez, Alexandre Deguine, D. Hourlier-Bahloul, et al.. Complex refractive indices in the TeraHertz domain of samples from atmospheric aerosol sources. 2021 46th International Conference on Infrared, Millimeter and Terahertz Waves (IRMMW-THz), Aug 2021, Chengdu, China. pp.1163, ⟨10.1109/irmmw-thz50926.2021.9566988⟩.

[76] Osseiran, Noureddin, et al. "Can the THz-TDS detect trace gases?." arXiv preprint arXiv:2410.07710 (2024).

[77] ] Y-S Lee, Springer, ”Principles of Terahertz Science and Technology”, Introduction, p2, 2009.

[78] Herbert M. Pickett, THz spectroscopy of the atmosphere, Proceedings Volume 3617, Terahertz Spectroscopy and Applications; (1999) https://doi.org/10.1117/12.347109.

[79] C. Kulesa, "Terahertz Spectroscopy for Astronomy: From Comets to Cosmology," in IEEE Transactions on Terahertz Science and Technology, vol. 1, no. 1, pp. 232-240, Sept. 2011, doi: 10.1109/TTHZ.2011.2159648.

[80] J.F. Lampin and G. Mouret and S. Dhillon and J. Mangeney, THz spectroscopy for fundamental science and applications, Photoniques, 101 (2020) 33-38. DOI: https://doi.org/10.1051/photon/202010133.

[81] X.-C. Zhang and X. F. Ma and Y. Jin and T.-M. Lu and E. P. Boden and P. D. Phelps and K. R. Stewart and C. P. Yakymyshyn; Terahertz optical rectification from a nonlinear organic crystal. Appl. Phys. Lett. 28 December 1992; 61 (26): 3080–3082. https://doi.org/10.1063/1.107968.

[82] Ozaki, Y. Infrared Spectroscopy—Mid-infrared, Near-infrared, and Far-infrared/Terahertz Spectroscopy. ANAL. SCI. 37, 1193–1212 (2021). https://doi.org/10.2116/analsci.20R008.

[83] T. S. Hearne, M.-H. Mammez, D. Mammez, M.-A. Martin-Drumel, P. Roy, O. Pirali, S. Eliet, S. Barbieri, F. Hindle, G. Mouret, and J.-F. Lampin, "Unlocking synchrotron sources for THz spectroscopy at sub-MHz resolution," Opt. Express 30, 7372-7382 (2022).

[84] Herbin, H., Deschutter, L., Deguine, A., Petitprez, D. (2023). Complex refractive index of crystalline quartz particles from UV to thermal infrared. Aerosol Science and Technology, 57(3), 255–265. https://doi.org/10.1080/02786826.2023.2165899.

[85] Chehab, M., Herbin, H., Deguine, A., Gosselin, S., Bizet, V., Petitprez, D. (2024). First complex refractive indices retrieval from FIR to UV: Application to kaolinite particles. Aerosol Science and Technology, 58(5), 498–511. https://doi.org/10.1080/02786826.2024.2318371.

[86] Charles Heath and Bobby Pejcic and Claudio Delle Piane and Lionel Esteban, Development of far-infrared attenuated total reflectance spectroscopy for the mineralogical analysis of shales, Fuel, Volume 182, 2016, Pages 771-779, https://doi.org/10.1016/j.fuel.2016.06.056.

[87] Saburo Sakai et al, Pulsed Terahertz Radiation for Sensitive Quantification of Carbonate Minerals, ACS Omega 2019, 4, 2, 2702−2707, https://doi.org/10.1021/acsomega.8b03311.

[88] Tatiana N. Brusentsova, Robert E. Peale, Douglas Maukonen, George E. Harlow, Joseph S. Boesenberg, Denton Ebel; Far infrared spectroscopy of carbonate minerals. American Mineralogist 2010;; 95 (10): 1515–1522. doi: https://doi.org/10.2138/am.2010.3380.

[89] Clotilde Prophete. Etude de la propagation des ondes térahertz en milieu diffusant pour l'imagerie pour hélicoptères en condition de brownout. Physique [physics]. Université Paris sciences et lettres, 2018.

[90] Steven T. Fiorino, Jason A. Deibel, Phillip M. Grice, Markus H. Novak, Julian Spinoza, Lindsay Owens, and Satya Ganti, "A technique to measure optical properties of brownout clouds for modeling terahertz propagation," Appl. Opt. 51, 3605-3613 (2012).

[91] Matthew B. Campbell and Edwin J. Heilweil "Noninvasive detection of weapons of mass destruction using terahertz radiation", Proc. SPIE 5070, Terahertz for Military and Security Applications, (29 July 2003); https://doi.org/10.1117/12.504297.

[92] J. Neu and C. A. Schmuttenmaer,"Tutorial: An introduction to terahertz time domain spectroscopy (THz-TDS)", Journal of Applied Physics 124, 231101 (2018).

[93] Mukherjee, P., Gupta, B. Terahertz (THz) Frequency Sources and Antennas - A Brief Review. Int J Infrared Milli Waves 29, 1091–1102 (2008). https://doi-org.ressources-electroniques.univ-lille.fr/10.1007/s10762-008-9423-0.

[94] Jahn, D., Lippert, S., Bisi, M. et al.,"On the Influence of Delay Line Uncertainty in THz Time-Domain Spectroscopy.", J Infrared Milli Terahz Waves 37, 605–613 (2016).

[95] Daniel M. Mittleman; Perspective: Terahertz science and technology. J. Appl. Phys. 21 December 2017; 122 (23): 230901. https://doi.org/10.1063/1.5007683.

[96] Jason B. Baxter and Glenn W. Guglietta, Terahertz Spectroscopy, Analytical Chemistry 2011 83 (12), 4342-4368, DOI: 10.1021/ac200907z.

[97] Koch, M., Mittleman, D.M., Ornik, J. et al. Terahertz time-domain spectroscopy. Nat Rev Methods Primers 3, 48 (2023). https://doi.org/10.1038/s43586-023-00232-z.

[98] E. Denakpo, T. Hannotte, M. Lavancier, S. E. Barois and R. Peretti, "Noise analysis, noise reduction and covariance estimation for Time domain Spectroscopy," 2022 47th International Conference on Infrared, Millimeter and

Terahertz Waves (IRMMW-THz), Delft, Netherlands, 2022, pp. 1-2, doi: 10.1109/IRMMW-THz50927.2022.9895812.

[99] R. Peretti, M. Lavancier, N. Vindas-Yassine, J. Vlieghe, T. Hannotte, and J-F. Lampin and F. Orieux, “A new metric for the comparison of permittivity models in terahertz time-domain spectroscopy,” arXiv preprint arXiv:2403.04332, 2021. https://github.com/THzbiophotonics.

[100] Osseiran, N., Bichon, J., Hannotte, T., Abdel-Kader, M., Witt, M., Eliet, S., and Peretti, R. (2024, September). Uncertainties estimation in THz-TDS experiments in transmittance, refractive index and spectroscopic parameters. In 2024 49th International Conference on Infrared, Millimeter, and Terahertz Waves (IRMMW-THz) (pp. 1-2). IEEE.

[101] Deguine A, Petitprez D, Clarisse L, et al (2020) Complex refractive index of volcanic ash aerosol in the infrared, visible, and ultraviolet. Applied Optics 59(4):884. https://doi.org/10.1364/AO.59.000884.

[102] Oliveira, Raphaela de, Luis A. G. Guallichico, Eduardo Policarpo, Alisson R. Cadore, Raul O. Freitas, Francisco M. C. da Silva, Verônica de C. Teixeira, et al. “High Throughput Investigation of an Emergent and Naturally Abundant 2D Material: Clinochlore.” Applied Surface Science 599 (October 15, 2022): 153959. https://doi.org/10.1016/j.apsusc.2022.153959.

[103] Hou, Mingqiang and Zhang, Qian and Tao, Renbiao and Liu, Hong and Kono, Yoshio and Chen, Bin and Fei, Yingwei. (2019). Temperature-induced amorphization in CaCO3 at high pressure and implications for recycled CaCO3 in subduction zones. Nature Communications. 10. 10.1038/s41467-019-09742-5.

[104] Rodriguez-Navarro, Carlos and Ruiz-Agudo, Encarnación and Luque, Ana and Rodriguez-Navarro, Alejandro and Ortega Huertas, Miguel. (2009). Thermal Decomposition of Calcite: Mechanisms of Formation and Textural Evolution of CaO Nanocrystals. American Mineralogist. 94. 578-593. 10.2138/am.2009.3021.

[105] W. E. Ranz and J. B. Wong, Impaction of Dust and Smoke Particles on Surface and Body Collectors, Ind. Eng. Chem. 1952, 44, 6, 1371–1381, https://doi.org/10.1021/ie50510a050.

[106] J. Bichon, A. Pillet, A. Sklia, D. Petitprez, R. Peretti and S. Eliet, "Complex refractive index determination of PTFE, TPX and polypropylene windows for TeraHertz broadband spectroscopy," 2022 47th International Conference on Infrared, Millimeter and Terahertz Waves (IRMMW-THz), Delft, Netherlands, 2022, pp. 1-2, doi: 10.1109/IRMMW-THz50927.2022.9895520.

[107] P.D. Cunningham, et al, *"Broadband terahertz characterization of the refractive index and absorption of some important polymeric and organic electro-optic materials"*, Journal of applied physics, 2011-02-22, Vol.109 (4), p.043505-043505-5.

[108] F. D'Angelo et al, Ultra-broadband THz time-domain spectroscopy of common polymers with THz air-photonics, Optics Express, 19 May 2014, Vol. 22, No.10.

[109] S. Ariyoshi, et al, "Broadband terahertz spectroscopy of cellulose nanofiber reinforced polypropylenes", Materials Science and Engineering: B Volume 265, March 2021, 115000.

[110] Roger W. Welker, Chapter 4 - Size Analysis and Identification of Particles, Rajiv Kohli, K.L. Mittal, Developments in Surface Contamination and Cleaning, William Andrew Publishing, 2012, Pages 179-213, https://doi.org/10.1016/B978-1-4377-7883-0.00004-3.

[111] Deboudt K, Flament P, Choel M, et al (2010) Mixing state of aerosols and direct observation of carbonaceous and marine coatings on African dust by individual particle analysis. Journal of Geophysical Research 115 (D24). https://doi.org/10.1029/2010JD013921.

[112] Shraddha S, Naganna S (2014) A Review ON K-means DATA Clustering APPROACH. International Journal of Information and Computation Technology 4(17).

[113] Sun Y, Chen H, Tada R, et al (2013) Esr signal intensity and crystallinity of quartz from gobi and sandy deserts in east asia and implication for tracing asian dust provenance. Geochem Geophys Geosyst 14:2615—-2627. https://doi.org/10.1002/ggge.20162.

[114] Scheetz BE, White WB (1977) Vibrational spectra of the alkaline earth double carbonates. American Mineralogist 62(1-2):36–50.

[115] Yan P, Zhang NR. Ning Huan, Zhou X, et al (2012) Characteristics of aerosols and mass closure study at two WMO GAW regional background stations in eastern China. Atmospheric Environment 60. https://doi.org/10.1016/j.atmosenv.2012.05.050.

[116] Wang, X. and Romanias, M. and Pei, Z. and Rousseau, A. and Thevenet, F., Uptake mechanism of acetic acid onto natural Gobi dust, ACS Earth Space Chem. 2020, 4, 9, 1650–1662.

[117] Romanias, M. and Zeineddine, M. and Gaudion, V. and Lun, X. and Thevenet, F. and Riffault, V., Heterogeneous interaction of isopropanol with natural Gobi dust, Environ. Sci. Technol. 2016, 50, 21, 11714–11722.

[118] Urupina, D. and Romanias, M.N. and Thevenet, F., How Relevant Is It to Use Mineral Proxies to Mimic the Atmospheric Reactivity of Natural Dust Samples? A Reactivity Study Using SO2 as Probe Molecule. Minerals 2021, 11, 282. https://doi.org/10.3390/min11030282.

[119] Battaglia S. Variations in the chemical composition of illite from five geothermal fields: a possible geothermometer. Clay Minerals. 2004;39(4):501-510. doi:10.1180/0009855043940150.

[120] Nagashima, K., Y. Suzuki, T. Irino, T. Nakagawa, R. Tada, Y. Hara, K. Yamada, and Y. Kurosaki (2016), Asian dust transport during the last century recorded in Lake Suigetsu sediments, Geophys. Res. Lett., 43, 2835–2842, doi:10.1002/2015GL067589.

[121] Baldo, C., Formenti, P., Nowak, S., Chevaillier, S., Cazaunau, M., Pangui, E., Di Biagio, C., Doussin, J.-F., Ignatyev, K., Dagsson-Waldhauserova, P., Arnalds, O., MacKenzie, A. R., and Shi, Z.: Distinct chemical and mineralogical composition of Icelandic dust compared to northern African and Asian dust, Atmos. Chem. Phys., 20, 13521–13539, https://doi.org/10.5194/acp-20-13521-2020, 2020.

[122] P. Agrinier, C. Destrigneville, T. Giunta, M. Bonifacie, G. Bardoux, J. Andre, F. Lucazeau, Strong impact of ion filtration on the isotopic composition of chlorine in young clay-rich oceanic sediment pore fluids, Geochimica et Cosmochimica Acta, Volume 245, 2019, Pages 525-541, ISSN 0016-7037, https://doi.org/10.1016/j.gca.2018.11.013.

[123] Choulet, F., Buatier, M., Barbanson, L. et al. Zinc-rich clays in supergene non-sulfide zinc deposits. Miner Deposita 51, 467–490 (2016). https://doi.org/10.1007/s00126-015-0618-8.

[124] Ma, J.Z., Ding, Z., Gates, J.B. et al. Chloride and the environmental isotopes as the indicators of the groundwater recharge in the Gobi Desert, northwest China. Environ Geol 55, 1407–1419 (2008). https://doi.org/10.1007/s00254-007-1091-1.

[125] Balkanski, Y., Schulz, M., Claquin, T., and Guibert, S.: Reevaluation of Mineral aerosol radiative forcings suggests a better agreement with satellite and AERONET data, Atmos. Chem. Phys., 7, 81–95, https://doi.org/10.5194/acp-7-81-2007, 2007.

[126] Feng Wang, Zhongping Lai, Guyu Peng, Lan Luo, Kai Liu, Xianmei Huang, Yantian Xu, Qinjing Shen, Daoji Li, Microplastic abundance and distribution in a Central Asian desert, Science of The Total Environment, Volume 800, 2021, 149529, https://doi.org/10.1016/j.scitotenv.2021.149529.

[127] Meunier, A., Velde, B. (2004). The Mineralogy of Illite — What is Illite?. In: Illite. Springer, Berlin, Heidelberg. https://doi.org/10.1007/978-3-662-07850-1_2.

[128] Alain Meunier, Bruce Velde; Solid solutions in I/S mixed-layer minerals and illite. American Mineralogist 1989;; 74 (9-10): 1106–1112.

[129] Pugliese Andrade, G.R., de Azevedo, A.C., Cuadros, J., Souza, V.S., Jr., Correia Furquim, S.A., Kiyohara, P.K. and Vidal-Torrado, P. (2014), Transformation of Kaolinite into Smectite and Iron-Illite in Brazilian Mangrove Soils. Soil Science Society of America Journal, 78: 655-672. https://doi.org/10.2136/sssaj2013.09.0381.

[130] G. W. Brindley, Zefi Sandalaki; Structure, composition and genesis of some long-spacing, mica-like minerals. American Mineralogist 1963;; 48 (1-2): 138–149.

[131] Schroeder, P. A. (1992). Far-infrared study of the interlayer torsional-vibrational mode of mixed-layer illite/smectites. Clays and Clay Minerals, 40(1), 81-91.

[132] Valenzano, L., Y. Noël, R. Orlando, C. M. Zicovich-Wilson, M. Ferrero, and R. Dovesi. "Ab Initio Vibrational Spectra and Dielectric Properties of Carbonates: Magnesite, Calcite and Dolomite." Theoretical Chemistry Accounts 117, no. 5 (May 1, 2007): 991–1000. https://doi.org/10.1007/s00214-006-0213-2.

[133] W. Shi et al. "High-pressure phase transitions in Ca-Mn carbonates (Ca,Mn)CO3 studied by Raman spectroscopy", American Mineralogist, Volume 97, pages 999–1001, 2012.

[134] Zhang, R. and R. Arimoto and J. An and S. Yabuki and and J. Sun (2005), Ground observations of a strong dust storm in Beijing in March 2002, J. Geophys. Res., 110, D18S06, doi:10.1029/2004JD004589.

[135] Naftaly M, Gregory A. Terahertz and Microwave Optical Properties of Single-Crystal Quartz and Vitreous Silica and the Behavior of the Boson Peak. Applied Sciences. 2021; 11(15):6733. https://doi.org/10.3390/app11156733.

[136] Davies, C.L., Patel, J.B., Xia, C.Q. et al. Temperature-Dependent Refractive Index of Quartz at Terahertz Frequencies. J Infrared Milli Terahz Waves 39, 1236–1248 (2018). https://doi.org/10.1007/s10762-018-0538-7.

[137] Wenhua Wang, Longyi Shao, Daizhou Zhang, Yaowei Li, Wenjun Li, Pengju Liu, Jiaoping Xing, Mineralogical similarities and differences of dust storm particles at Beijing from deserts in the north

and northwest, Science of The Total Environment, Volume 803, 2022, https://doi.org/10.1016/j.scitotenv.2021.149980.

[138] Karr, Clarence. Infrared and Raman Spectroscopy of Lunar and Terrestrial Minerals. Elsevier, 2013.

[139] Jovanovski, Gligor, Makreski, Petre, Kaitner, Branko, Šoptrajanov, Bojan. (2009). MINERALS FROM MACEDONIA. X-RAY POWDER DIFFRACTION vs. VIBRATIONAL SPECTROSCOPY IN MINERAL IDENTIFICATION. Contributions, Sec. Math. Tech. Sci., MANU. 30. 7-34.

[140] Zsirka B, Horváth E, Makó É, Kurdi R, Kristóf J. Preparation and characterization of kaolinite nanostructures: reaction pathways, morphology and structural order. Clay Minerals. 2015;50(3):329-340. doi:10.1180/claymin.2015.050.3.06.

[141] Charles Heath, Bobby Pejcic, Claudio Delle Piane, Lionel Esteban, Development of far-infrared attenuated total reflectance spectroscopy for the mineralogical analysis of shales, Fuel, Volume 182, 2016, Pages 771-779, https://doi.org/10.1016/j.fuel.2016.06.056.

[142] Osseiran, N., Bichon, J., Eliet, S. and Peretti, R. (2024, September). Towards the elimination of water in THz-TDS data. In 2024 49th International Conference on Infrared, Millimeter, and Terahertz Waves (IRMMW-THz) (pp. 1-2). IEEE.

[143] Herbin, Hervé, et al. "Complex refractive index of crystalline quartz particles from UV to thermal infrared." Aerosol Science and Technology 57.3 (2023): 255-265.

[144] Bichon, Jeyan, et al. "Phonon polaritons impact atmosphere transparence in the TeraHertz range." 2024 49th International Conference on Infrared, Millimeter, and Terahertz Waves (IRMMW-THz). IEEE, 2024.

[145] Dakota E. McCoy, Anna V. Shneidman, Alexander L. Davis, Joanna Aizenberg, Finite-difference Time-domain (FDTD) Optical Simulations: A Primer for the Life Sciences and Bio-Inspired Engineering, Micron, Volume 151, 2021, 103160, https://doi.org/10.1016/j.micron.2021.103160.

[146] Dakota E. McCoy, Anna V. Shneidman, Alexander L. Davis, Joanna Aizenberg, Finite-difference Time-domain (FDTD) Optical Simulations: A Primer for the Life Sciences and Bio-Inspired Engineering, Micron, Volume 151, 2021, 103160, https://doi.org/10.1016/j.micron.2021.103160.

[147] Lin Cheng, Guixian Zhu, Gannan Liu, Lianqing Zhu, FDTD simulation of the optical properties for gold nanoparticles, 2020 Mater. Res. Express 7 125009, https://doi.org/10.1088/2053-1591/abd139.

[148] Jean-Pierre Berenger, A perfectly matched layer for the absorption of electromagnetic waves, Journal of Computational Physics, Volume 114, Issue 2, 1994, Pages 185-200, https://doi.org/10.1006/jcph.1994.1159.

[149] Davies, C.L., Patel, J.B., Xia, C.Q. et al. Temperature-Dependent Refractive Index of Quartz at Terahertz Frequencies. J Infrared Milli Terahz Waves 39, 1236–1248 (2018). https://doi.org/10.1007/s10762-018-0538-7.

[150] Th. Posch, A. Baier, H. Mutschke, and Th. Henning, Carbonates in Space: The Challenge of Low-Temperature Data, The Astrophysical Journal, 2007, Volume 668, Number 2, https://doi.org/10.1086/521390.

[151] Pavese, A., M. Catti, G. D. Price, and R. A. Jackson. "Interatomic Potentials for CaCO3 Polymorphs (Calcite and Aragonite), Fitted to Elastic and Vibrational Data." Physics and Chemistry of Minerals 19, no. 2 (August 1, 1992): 80–87. https://doi.org/10.1007/BF00198605.

[152] Sekkal, W., N. Taleb, A. Zaoui, and I Shahrour. "A Lattice Dynamical Study of the Aragonite and Post-Aragonite Phases of Calcium Carbonate Rock." American Mineralogist 93, no. 10 (October 1, 2008): 1608–12. https://doi.org/10.2138/am.2008.2820.

[153] Hellwege, K. H., W. Lesch, M. Plihal, and G. Schaack. "Zwei-Phononen-Absorptionsspektren und Dispersion der Schwingungszweige in Kristallen der Kalkspatstruktur." Zeitschrift für Physik A Hadrons and nuclei 232, no. 1 (February 1970): 61–86. https://doi.org/10.1007/BF01394946.

[154] R Ruppin, Polariton modes of spheroidal microcrystals, 1998 J. Phys.: Condens. Matter 10 7869, https://doi.org/10.1088/0953-8984/10/35/019.

[155] Bruggeman, D.A.G. (1935), Berechnung verschiedener physikalischer Konstanten von heterogenen Substanzen. I. Dielektrizitätskonstanten und Leitfähigkeiten der Mischkörper aus isotropen Substanzen. Ann. Phys., 416: 636-664. https://doi.org/10.1002/andp.19354160705.

[156] Jamaian, Siti, Mackay, Tom. (2010). On limitations of the Bruggeman formalism for inverse homogenization. Journal of Nanophotonics. 4. 10.1117/1.3460908.

[157] Y. Battie, A. Resano-Garcia, N. Chaoui, Y. Zhang, A. En Naciri; Extended Maxwell-Garnett-Mie formulation applied to size dispersion of metallic nanoparticles embedded in host liquid matrix. J. Chem. Phys. 28 January 2014; 140 (4): 044705. https://doi-org.ressources-electroniques.univ-lille.fr/10.1063/1.4862995.

[158] Fregoni, Jacopo, and Stefano Corni. "Polaritonic chemistry." Theoretical and Computational Photochemistry. Elsevier, 2023. 191-211.

[159] Zhang, X., et al. (2008). "Observations of high atmospheric dust concentrations over the Taklimakan Desert during a dust storm." Atmospheric Environment, 42(5), 871-878.

[160] Source: Boucher, O. and Anderson, T. L. (2006). "Climate Trade-offs in the Assessment of Global Dust Emissions." Science, 312(5771), 640-644.